

FAKULTÄT FÜR PHYSIK
TECHNISCHE UNIVERSITÄT MÜNCHEN

Experimental and Numerical Investigation of Neon-Seeded High Radiation Discharges at the JET Tokamak

Stephan Glögger

Vollständiger Abdruck der von der Fakultät für Physik der Technischen Universität München zur Erlangung eines Doktors der Naturwissenschaften genehmigten Dissertation.

Vorsitz:

Prof. Dr. David Egger

Prüfer*innen der Dissertation:

1. Prof. Dr. Ulrich Stroth

2. Prof. Dr. Mathias Groth

Die Dissertation wurde am 01.02.2022 bei der Technischen Universität München eingereicht und durch die Fakultät für Physik am 04.04.2022 angenommen.



FAKULTÄT FÜR PHYSIK
TECHNISCHE UNIVERSITÄT MÜNCHEN

**Experimental and Numerical
Investigation of Neon-Seeded
High Radiation Discharges
at the JET Tokamak**

Author: Stephan Glögler
Supervisor: Prof. Dr. Ulrich Stroth
Advisor: Dr. Marco Wischmeier



MAX-PLANCK-GESELLSCHAFT



EUROfusion

Abstract

Generating energy from nuclear fusion is an attractive alternative to energy sources that produce considerable amounts of carbon dioxide or radioactive waste. The currently most advanced concepts for a fusion reactor are based on magnetic confinement. In future fusion devices the power deposited onto the divertor target plates can damage them, if not mitigated. The necessary limitation of the plasma temperature in front of the targets to below about 4 eV can only be achieved by dissipating the fusion power before it reaches the target. In order to increase the power losses by electromagnetic radiation, impurity species are deliberately injected (or “seeded”) into the plasma. The seeding of impurities that increase the radiation power from the region of open field lines, the scrape-off layer (SOL), and the divertor is an established technique. However, to mitigate the power of devices like the future demonstration power plant DEMO, the radiation losses from these regions are not sufficient and additional power losses from the region of closed field lines are required. To avoid a degradation of the fusion performance and the plasma stability by impurities in the plasma core, the impurity radiation in the confined region should primarily be located in the edge, close to the separatrix. Currently, efforts are made to investigate ways to increase the radiation power in the edge and the ways it affects the core stability. This thesis contributes to these efforts by the analysis of data from neon-seeded discharges in the currently largest tokamak JET and from numerical simulations of these discharges with the SOLPS-ITER transport code package.

In many of the neon-seeded JET discharges, phases of a high energy confinement mode without characteristic periodic edge instabilities (M-mode) were observed. During these M-mode phases the radiation was concentrated in the edge close to the magnetic null (called X-point). The density at the steep edge pressure gradient (pedestal) was degraded and the power flux onto the divertor target plates was reduced (a state called detachment). These three phenomena seemed to occur simultaneously during the M-mode phases and a correlation among them was assumed. Furthermore, the neon seeding led to an increase of the core temperature as well as a reduction of the influx of wall impurities into the core. The comparably low energy confinement time was caused by the experiments’ setup, but was not further reduced by the neon seeding. The core and edge radiation powers increased with increased neon seeding, whereas the divertor radiation power saturated, similar to the total radiative power fraction. Due to the high confinement mode in conjunction with high radiation powers and detached targets, this regime appears to be promising with regard to future fusion devices.

To investigate the possibility of a correlation between the phenomena observed during the M-mode phases numerical simulations were set up in SOLPS-ITER similar to the experiments. In the simulations the neon seeding rate was ramped up until they became numerically unstable. Like in the experiment higher neon seeding rates led to an increase in core radiation. Although the radiation in the edge was increased as well, a pronounced X-point radiator was only found in

cases that were not converged. At highest neon seeding rates the inner target was in detachment, but the outer target was not and remained in the low recycling regime. The pressure losses at the inner target necessary for detachment originated mostly from a region in the divertor close to the target, whereas the pressure losses in the pedestal were much lower. A lack of divertor neutral deuterium density due to the core fuelling assumed in the simulations as well as the neglect of drift effects are discussed to be the main cause for the attached outer target as well as for the low radiation powers in the simulations. Despite these limitations the simulations could, at least partly, reproduce key experimental features. Their results imply that under the given simulation conditions, the correlation between X-point radiator, the drop in pedestal pressure and detachment of the targets is not as strong as the experiments suggest.

Zusammenfassung

Kernfusion ist eine attraktive Alternative zu herkömmlichen Energiequellen, die erhebliche Mengen an Kohlendioxid oder radioaktivem Abfall erzeugen. Die bisher am weitesten erforschten Konzepte für einen Fusionsreaktor beruhen auf magnetischem Einschluss. Die in solchen künftigen Fusionsreaktoren erzeugte Leistung ist in der Lage, die Targetplatten des Divertors zu beschädigen. Daher ist es nötig, die Plasmatemperatur am Target unter circa 4 eV zu halten, indem die Fusionsleistung auf anderem Wege abgeführt wird. Dies kann durch das gezielte Einbringen (engl. seeding) von Verunreinigungen ins Plasma erreicht werden, die zusätzliche Leistungsverluste durch elektromagnetische Strahlung hervorrufen. Das Seeding von Verunreinigungen, die die Strahlungsleistung im Bereich offener Feldlinien, der sog. Abschältschicht (engl. scrape-off layer), und im Divertor erhöhen, ist bereits ein gängiges Verfahren. Um jedoch die Leistung zukünftiger Reaktoren, wie die des zukünftigen Demonstrationskraftwerks DEMO, abzuführen, reichen die Strahlungsverluste aus diesen Regionen nicht aus, und es werden zusätzliche Leistungsverluste aus dem Bereich geschlossener Feldlinien benötigt. Die Verunreinigungen sollte hierbei hauptsächlich im Randbereich nahe der Separatrix strahlen, um negative Beeinträchtigungen der Fusionsleistung und der Plasmastabilität durch die Verunreinigungen zu vermeiden. Wie die Strahlungsleistung im Randbereich erhöht werden kann und wie sie den Plasmakern beeinflusst, ist Gegenstand der aktuellen Forschung. Durch die Analyse von Daten Neon-geseedeter Entladungen am derzeit größten Tokamak der Welt, JET, und aus numerischen Simulationen dieser Entladungen mit dem Transportcode SOLPS-ITER, trägt diese Arbeit zu dieser Forschung bei.

In vielen der Neon-geseedeten Entladungen bei JET wurden Phasen einer Mode mit hohem Energieeinschluss ohne typische periodische Randinstabilitäten (M-Mode) beobachtet. In den M-Mode-Phasen war die Strahlung im Randbereich nahe des magnetischen Nullpunktes, des sog. X-Punktes, konzentriert. Die Dichte im Bereich des steilen Druckgradienten am Rand (engl. pedestal) war verringert und der Leistungsfluss auf die Divertortargetplatten reduziert (das Target befindet sich im sog. Detachment). Diese drei Phänomene schienen während der M-Mode-Phasen gleichzeitig aufzutreten, weshalb ein Zusammenhang vermutet wurde. Das Neon-Seeding führte desweiteren zu einem Anstieg der Temperatur, sowie zu einem geringeren Fluss von Wandverunreinigungen in das Plasma. Die vergleichsweise niedrige Energieeinschlusszeit war durch die Konfiguration des Experiments bedingt, sie sank aber durch das Neon-Seeding nicht weiter. Mit zunehmendem Neon-Seeding stiegen die Strahlungsleistungen aus Kern- und Randbereich an, wohingegen die Divertorstrahlungsleistung in Sättigung ging, ähnlich dem Anteil der Gesamtstrahlungsleistung. Aufgrund des hohen Einschlusses in Verbindung mit hohen Strahlungsleistungen und der Targets im Detachment erscheint dieses Regime im Hinblick auf zukünftige Fusionsreaktoren vielversprechend.

Um zu erforschen, ob die während der M-Mode-Phasen beobachteten Phänomene zusammenhängen könnten, wurden, in Anlehnung an die Experimente, numerische Simulationen mit dem

Transportcode SOLPS-ITER durchgeführt. In den Simulationen wurde die Menge geseedeten Neons erhöht, bis sie numerisch instabil wurden. Wie auch im Experiment führte höheres Neon-Seeding zu einem Anstieg der Strahlung im inneren Plasma. Obwohl die Strahlung im Randbereich ebenfalls anstieg, konnte ein ausgeprägter X-Punkt-Strahler nur in Simulationen beobachtet werden, die nicht konvergiert waren. Bei höchsten Mengen an Neon-Seeding war das innere Target im Detachment, nicht jedoch das äußere, welches im Niedrig-Recycling-Regime verblieb. Die für das Detachment nötigen Druckverluste am inneren Target stammten überwiegend aus einem Bereich des Divertors nahe des Targets; die Druckverluste im Pedestal hingegen waren deutlich niedriger. Ein Mangel an Deuterium-Neutralteilchen im Divertor, bedingt durch die in den Simulationen angenommene Versorgung über den Kern, sowie die Nichtberücksichtigung von Drifteffekten, werden als Gründe für das nicht auftretende Detachment am äußeren Target sowie die niedrigen Strahlungsleistungen diskutiert. Trotz dieser Einschränkungen konnten die Simulationen zumindest teilweise wichtige Eigenschaften des Experiments nachbilden. Ihre Ergebnisse legen nahe, dass unter den gegebenen Simulationsbedingungen der Zusammenhang zwischen X-Punkt-Strahler, Einbruch des Pedestaldrucks und Detachment nicht so stark ist, wie das Experiment vermuten lässt.

Contents

Abstract	iii
Zusammenfassung	v
1 Introduction and Basics	1
1.1 Nuclear Fusion	1
1.2 Power Exhaust by Impurity Radiation	3
1.3 Scope and Outline of the Thesis	6
2 Scrape-Off Layer and Divertor Physics	8
2.1 Divertor Tokamaks	8
2.1.1 The Tokamak Principle	8
2.1.2 The Divertor Configuration	11
2.1.3 H-mode	13
2.2 Plasma-Wall Interaction	15
2.2.1 The Sheath	15
2.2.2 Recycling and Sputtering	15
2.2.3 Power Deposition Limit	16
2.3 Volumetric Processes	17
2.3.1 Ion-Neutral Interactions	17
2.3.2 Plasma Radiation	18
2.4 Divertor Regimes	20
2.4.1 Heat Transport	21
2.4.2 Recycling Regimes	22
2.4.3 Detachment	22
2.4.4 Detachment by Impurity Radiation	24
2.5 Impurity Radiation	25
2.5.1 Impurity Radiation Species and Poloidal Distribution	25
2.5.2 X-Point Radiation	26
2.5.3 SOL and Divertor Radiation	26
2.5.4 Core Radiation	27
2.5.5 Edge Radiation	28
2.6 Numerical Simulations of Detached High Radiation Experiments	28
2.7 Brief Summary and Outline of This Thesis	29
3 The SOLPS-ITER Code Package	31
3.1 The Plasma Fluid Code B2.5	31
3.1.1 Braginskii Equations	31
3.1.2 Perpendicular Transport	33

3.2	The Monte Carlo Neutral Code EIRENE	34
3.3	SOLPS-ITER Workflow	36
3.4	Simulation Setup in This Thesis	38
3.4.1	Running the Simulations	38
3.4.2	Physical Grid (B2.5)	38
3.4.3	Pumping and Puffing in EIRENE	40
3.4.4	Atomic and Molecular Physics	40
3.4.5	Boundary Conditions	40
4	The Joint European Torus (JET)	44
4.1	JET Heating Systems	44
4.1.1	Ohmic Heating	44
4.1.2	Ion Cyclotron Resonance Heating (ICRH)	45
4.1.3	Neutral Beam Injection Heating (NBI)	45
4.2	Fuelling and Pumping	45
4.2.1	Gas Introduction Modules (GIMs)	45
4.2.2	Pumping	46
4.3	JET Diagnostics	46
4.3.1	Foil Bolometers and Tomographic Reconstruction	46
4.3.2	Visible Light Spectroscopy (VLS)	48
4.3.3	Charge Exchange Recombination Spectroscopy (CXRS)	48
4.3.4	High Resolution Thomson Scattering (HRTS)	49
4.3.5	Electron Cyclotron Emission (ECE)	49
4.3.6	Far-Infrared Interferometer (FIR)	49
4.3.7	Divertor Langmuir Probes	50
4.3.8	Divertor Thermocouples	51
4.4	Divertor Physics in JET	51
4.4.1	In-Out Asymmetry	51
4.4.2	Divertor Wall Material	52
4.4.3	Divertor Geometry and Magnetic Field Geometry	52
4.4.4	Impact of Radiation	54
4.5	Relevance for This Thesis	55
5	Experimental Analysis	56
5.1	Experimental Setup	56
5.2	Characterisation of Neon-Seeded JET Discharges	57
5.2.1	Low Heating Power (15 MW)	57
5.2.2	Medium Heating Power (19 MW)	60
5.2.3	High Heating Power (29 MW)	63
5.2.4	Influence of the Neon Puff on the L-H Transition	68
5.3	Improved Core Energy Confinement	71
5.3.1	ASTRA-TGLF Transport Prediction of Core Temperature Profiles	71
5.3.2	Density Peaking	73
5.3.3	Energy Confinement	74
5.3.4	Neutron Rate	75
5.4	Impurity Content	76

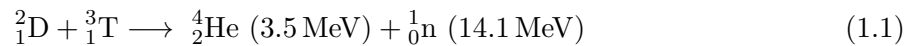
5.5	Poloidal Radiation Distribution	78
5.6	Summary and Discussion	80
6	SOLPS-ITER Modelling	82
6.1	Setup	82
6.2	Poloidal Radiation Distribution	83
6.3	Detachment and Pressure Loss	86
6.4	Deuterium and Impurity Distribution	91
6.5	Summary and Discussion	94
7	Conclusion	96
	Bibliography	98
A	JET Pulse Numbers with Neon Seeding	118
B	Acknowledgments	120

1 Introduction and Basics

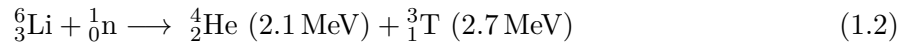
In the past 50 years the world's energy consumption has more than doubled [1] and is projected to further grow in the upcoming decades [2]. To avoid severe consequences arising from global warming it is imperative to curtail the emission of CO₂ [3] and hence transition away from fossil energy sources. It is currently discussed if and how it is technically and economically feasible to generate the world's entire energy supply from carbon-free energy sources (e.g. in [4, 5] and [6]), in particular from renewable sources like solar, wind, hydro, or geothermal energy. In this light the construction of nuclear fusion power plants might be suitable, especially to provide a base load which so far is being generated by power plants based on carbon or nuclear fission. In contrast to the latter, a nuclear fusion power plant does not emit CO₂, is inherently safe to operate, and produces significantly less long-lived radioactive waste than a fission reactor (cf. [7, ch. 1.5] and references therein).

1.1 Nuclear Fusion

Nuclear fusion naturally occurs in the Sun and other stars [8]. In a fusion process two light nuclei form a heavier nucleus. The mass difference between the educts and the products is released as energy. This energy as well as the heavier nuclei up to ⁵⁶₂₆Fe that were bred in long gone stars are the basis for life on Earth. In order for the strong interaction to act, the nuclei have to tunnel through the Coulomb barrier. This requires high kinetic energies of the nuclei, and thus high temperatures that by far exceed the ionisation energies of atoms. The atoms are hence present in the plasma state. The nucleus ⁴₂He, also called alpha particle, has a particularly high binding energy, which makes fusion reactions producing this nucleus favourable in terms of energy gain. The predominant reaction in the Sun, the proton-proton reaction chain [9], is not eligible for a reactor on Earth due to its very low cross-section as a result of the necessity for the weak interaction to take effect [10, ch. 7][9]. Out of the suitable fusion reactions the reaction



has by far the highest reaction rate for temperatures up to some 100 keV. Deuterium can easily be found in water (natural abundance of deuterium: 0.000 115 [11]) of which is plenty available on Earth. In contrast to deuterium, tritium is radioactive and decays with a half-life time of 12.32 years [12], rendering its extraction from natural sources unfeasible and its handling and storage more challenging. One way to bypass these difficulties is to breed the tritium in the fusion reactor's blanket from lithium, exploiting the high-energetic neutron created in the fusion process (Eq. 1.1). The most favourable reaction for this is [13]:



Current experiments are mostly run with only deuterium in order to avoid the enrichment of radioactive material in the components by tritium itself or neutron bombardment of the plasma-facing components.

The quotient of the thermal power gained by nuclear fusion P_{fus} (not to confuse with the electrical power gain) to the external heating power P_{ext}

$$Q = \frac{P_{\text{fus}}}{P_{\text{ext}}} \quad (1.3)$$

must be larger than 1 for a reactor to produce net energy. Considering that in reaction Eq. 1.1 80% of the fusion power is transported away by the neutrons, Q must at least be 5 in order to produce energy. The reactor reaches ignition when it is able to sustain its temperature only by the internal heating power of the alpha particles (P_{α}) created in the fusion reaction, i.e. when $P_{\text{ext}} = 0$ and $Q \rightarrow \infty$. Up to this date the maximum value in a fusion experiment is $Q = 0.64$, which was achieved during the 1997 JET deuterium-tritium campaign [14].

The conditions necessary for ignition can be estimated using the Lawson criterion (originally introduced in [15]; derivations of modified forms can be found for example in [7, 16–18]). The ability of a plasma device to confine the energy is represented by the energy confinement time

$$\tau_{\text{E}} = \frac{W_{\text{th}}}{P_{\text{loss}} - dW_{\text{th}}/dt} \quad (1.4)$$

in which all the plasma's thermal energy $W_{\text{th}} = \int_V \frac{3}{2} (n_e T_e + n_i T_i) dV$ ¹ is completely dissipated. In a fusion plasma the simple power balance $P_{\text{heat}} = P_{\text{ext}} + P_{\alpha} = P_{\text{loss}}$ must be fulfilled. In the case of an ignited plasma $P_{\text{ext}} = 0$ and the relation $P_{\alpha} > P_{\text{loss}}$ results in the triple product

$$\bar{n} \cdot \bar{T} \cdot \tau_{\text{E}} > \frac{12\bar{T}^2}{\langle \sigma v \rangle \epsilon_{\alpha}} \quad (1.5)$$

with \bar{n} and \bar{T} being the average density and temperature, $\langle \sigma v \rangle$ the reaction rate coefficient and ϵ_{α} the energy carried by an alpha particle after the reaction. The resulting curve (see Fig. 1.1) has a minimum at around $\bar{T} = 15 \text{ keV}$, i.e. ignition is easiest to achieve at this temperature under the condition

$$\bar{n} \cdot \bar{T} \cdot \tau_{\text{E}} > 3 \cdot 10^{24} \frac{\text{eV s}}{\text{m}^3} \quad (1.6)$$

While in inertial confinement fusion [19] it is tried to satisfy the Lawson criterion by compressing the plasma with lasers to densities in the orders of magnitude around $1 \times 10^{32} \text{ m}^{-3}$ at very low

¹Note that in plasma physics temperatures are usually given in eV, hence the Boltzmann constant k_{B} is omitted.

confinement times of around 1×10^{-12} s [20], magnetic confinement fusion operates at lower densities of around $1 \times 10^{20} \text{ m}^{-3}$ and confinement times around 1 s. In this thesis only magnetically confined plasmas are treated.

Fusion is taking place in a temperature range where the involved gases are in the plasma state and can thus be manipulated using electromagnetic fields. In order to reduce the losses of particles and energy occurring at the ends of linear devices [21, 22], the principal component of today's most advanced configurations for magnetic confinement is a toroidally closed magnetic field. To avoid particle losses by drift effects, an additional poloidal field component is necessary (see Fig. 2.1 and Fig. 2.2). While in stellarators this poloidal magnetic field is generated by the shape of the three-dimensional field coils [23], in tokamaks it is created by the induction of a toroidal current through a central solenoid [18] (see subsection 2.1.1). Since charged plasma particles follow magnetic field lines, two major areas can be distinguished in a magnetic confinement device: the confined region in which magnetic field lines are closed in itself, confining the charged plasma particles and enabling the fusion reaction, and the scrape-off layer (SOL) in which the open field lines transport particles and heat to the device's wall with which they intersect. For the purpose of this thesis the confined region is subdivided in the inner core region and the outer edge or pedestal region. Most of the current tokamaks are equipped with a divertor (see subsection 2.1.2), a configuration which allows to divert these fluxes into a region far from the confined region and onto target plates. The flux surface separating the SOL and the confined region is then called separatrix.

With a major radius of $R = 2.96$ m the largest tokamak in operation is JET (Joint European Torus) [24], located in Culham (United Kingdom). The international experimental device ITER ($R = 6.2$ m) is currently under construction in Cadarache (France) and foreseen to produce its first plasma in 2025 and to reach $Q = 10$ in a later stage. Based on the results of ITER, a demonstration power plant DEMO might be designed and constructed as subsequent step on the road to a nuclear fusion power plant. In ITER and DEMO considerable amounts of fusion power will be produced, which raises the issue of its exhaustion.

1.2 Power Exhaust by Impurity Radiation

In future fusion devices like ITER or DEMO the power load onto the divertor target plates has to be limited due to tight constraints set by the material properties. The power originating from the confined region must be exhausted before it reaches the divertor targets. This can be achieved by electromagnetic radiation, which in a plasma mainly occurs in the form of line radiation from atomic transitions and recombination, and synchrotron radiation/bremsstrahlung (see section 2.3). The intrinsic radiation power losses of a plasma consisting of deuterium, tritium, and the produced helium are not sufficient to dissipate enough power by radiation. Additional radiative power losses can be achieved by the deliberate injection of impurity gases, so-called seeding, into the plasma. The location in which atoms of a certain species radiate depends on the temperature distribution. In the core, bremsstrahlung and line radiation of heavy impurities prevail, in the SOL and in the divertor line radiation and recombination radiation of light species like deuterium are dominant.

The fraction of the total heating power ($P_{\text{heat}} = P_{\alpha} + P_{\text{ext}} = \frac{1}{5}P_{\text{fus}} + P_{\text{ext}}$) that has to be dissipated is defined as

$$f_{\text{diss}} = \frac{P_{\text{diss}}}{P_{\text{heat}}} = \frac{P_{\text{heat}} - P_{\text{div,max}}}{P_{\text{heat}}} \quad (1.7)$$

with $P_{\text{div,max}}$ being the maximum power to be deposited onto the divertor target tiles, which can be expressed as product of the maximum perpendicular power flux density onto the divertor target tiles with the plasma wetted area:

$$P_{\text{div,max}} = q_{\perp,\text{div,max}} \cdot A_{\text{wet}} = q_{\perp,\text{div,max}} \cdot \lambda_{\text{int}} \cdot 2\pi R \quad (1.8)$$

with λ_{int} being the width of the target power load and R the major radius. The energy that is deposited on the target can be reduced through low temperatures and low particle fluxes. A regime in which the heat flux onto the target and the pressure between mid-plane and the targets is reduced [25] is called detachment (see subsection 2.4.3). For future fusion machines detached targets are indispensable.

Table 1.1: Rough key figures of ITER and DEMO for simple power exhaust estimates.

	ITER		DEMO	
P_{fus}	500 MW	[26]	2 GW	[27]
P_{α}	100 MW		400 MW	
P_{ext}	50 MW	[28]	100 MW	
P_{heat}	150 MW		500 MW	[27, 29, 30]
$q_{\text{div,max}}$	<10 MWm ⁻²	[28]	5–10 MWm ⁻²	[31]
A_{wet}	3.5 m ²	[26]	1–2 m ²	[27]
$P_{\text{div,max}}$	35 MW		5–20 MW	
$P_{\text{rad,sep}}$	30–50 MW	[26, 32]	> 350 MW	(see text)
$P_{\text{rad,div/sol}}$	60–70 MW	[26]	≈100 MW	[32]

In Tab. 1.1 the foreseen values that are most relevant for estimating the feasibility of power exhaust in ITER and DEMO are listed. With these values it can be estimated from Eq. 1.7 that for ITER f_{diss} must be in the range of 0.60–0.75 [32]. According to Eq. 1.7 the dissipative power fraction of DEMO must be larger than 0.95 [31, 32]. Such fractions can only be achieved by additional loss mechanisms of which the most important one is electromagnetic radiation.

While for ITER it is predicted that major parts of P_{heat} are either radiated by intrinsic core radiation (mostly bremsstrahlung) and induced SOL impurity radiation or deposited on the divertor [26], things will look different in DEMO. Assuming that DEMO has a similar capability for SOL and divertor dissipation as ITER [32], the radiative power fraction inside the separatrix alone must be

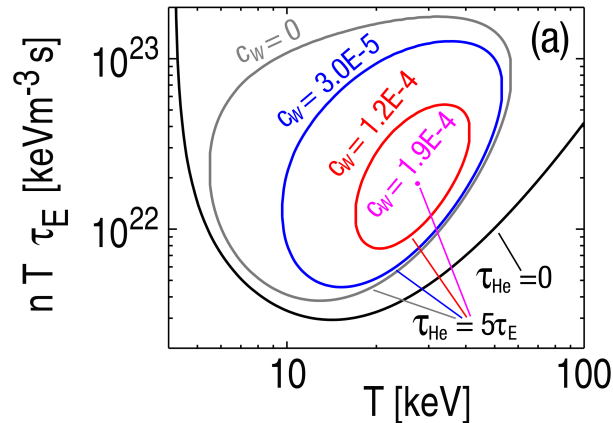


Figure 1.1: Burn curve from the triple product for a pure deuterium plasma (black) and for different tungsten impurity concentrations (at a helium particle confinement time of $\tau_{\text{He}} = 5 \cdot \tau_{\text{E}}$). Small amounts of tungsten can already hinder ignition, which is possible inside the burn curves. Taken from [33, Fig. 7(a)].

$$f_{\text{rad,sep}} = \frac{P_{\text{heat}} - P_{\text{div,max}} - P_{\text{rad,div/sol}}}{P_{\text{heat}}} > 0.7 \quad (1.9)$$

The seeding of impurities for the purpose of increasing the SOL and divertor radiation is a well-researched technique. Seed impurities and their radiation might pose problems in the core region, though: Additional power losses from the core, especially from high- Z impurities, including e.g. tungsten from the wall, as well as the replacement of hydrogenic ions needed for the fusion reaction by low- Z species can lead to conditions that reduce the operational space of a burning plasma or even render the ignition of the plasma impossible. Additional power loss terms are to be appended to the divisor on the RHS of Eq. 1.5, a dilution of the core plasma leads to a decrease of n on the LHS. Both effects result in a deformation of the burn curve [33, 34], as shown in Fig. 1.1, where the burn curves for various tungsten concentrations and a fix helium confinement time are depicted. These considerations set strict limits to the allowed amount of impurity atoms in the core and additionally induced radiation must origin in the edge, close to the separatrix.

Impurity radiation from the confined region poses not only a limitation to the feasibility of a nuclear fusion reactor but also causes operational problems. Power losses by radiation can lead to a transition from a high confinement to a low confinement regime (see subsection 2.1.3). For a power plant like DEMO the high confinement regime is foreseen [35] and impurity particles transported towards the core will reduce the fusion performance [34]. Globally or locally high radiation powers might be stable in some cases, for example the X-point radiator discussed later, but they can also lead to the growth of instabilities and hence to the disruption of the discharge. A disruption is characterised by a quasi-sudden loss of the stored energy and the plasma current. Disruptions are to be avoided at all costs in future devices as they can cause massive damage to the first wall, the coils, and other mechanical components. Nonetheless, high radiative power fractions from inside and outside the confined region will be crucial to safely operate such a future device.

1.3 Scope and Outline of the Thesis

In recent years, scenarios with high divertor and SOL radiation have been examined extensively, providing new knowledge regarding their suitability for ITER. The development of scenarios with high edge radiation for DEMO is yet in an early stage and only few thorough analyses of corresponding experiments are available. However, many studies performed so far focussed on single aspects or were conducted on a specific range of discharge parameters. At JET the new tungsten divertor allows to study new impurity seeding scenarios with relevance for ITER and DEMO, for example high divertor radiation by nitrogen seeding [36]. The safe operation of future machines like DEMO, though, requires much higher radiative power fractions and radiation also from inside the separatrix. At JET the experimental campaigns M13-17 and M15-20 were dedicated to investigate ways to increase the total radiative power fraction as well as the impact of the poloidal radiation distribution on the confinement and the plasma stability. The discharges were performed at high densities and a wide range of heating powers and puff rates of various impurities (nitrogen, argon, krypton, neon) in order to reach f_{rad} and P_{heat}/R values as high as possible [37, 38].

In this thesis the neon-seeded discharges of these JET campaigns were examined with respect to the characteristics of discharges with strong edge radiation. The analysis of neon-seeded high radiation experiments was restricted so far to the analysis of only few (or single) discharges at a time, mostly in similar ranges of heating powers, seeding, or fuelling. In this thesis a more general approach is taken, evaluating the whole range of heating powers, fuelling, and neon seeding applied in these neon-seeded high radiation discharges (see Appendix A for an overview over these pulses). The availability of discharges with different heating powers ranging from 15 to 30 MW allows on the one hand the evaluation of single discharges, e.g. by a comparison of different time points with few determined parameters varying between them or by a comparison with other discharges, and on the other hand an evaluation of the complete set of discharges by the implementation of a small database to reveal correlations not to be seen in single discharges or a limited set of them. This broad range of discharges allowed to thoroughly examine, among others, the radiation distribution and its development, the changes in the energy confinement regime, the power fluxes to the divertor, the impurity content of the plasma, and the plasma performance.

The experimental evaluations are supplemented by results of SOLPS-ITER [39, 40] simulations, a numerical tool which couples a plasma fluid code to a Monte Carlo neutral particle code. Using a set of SOLPS-ITER simulations permits to reproduce trends found in experiments and explore new correlations that are inaccessible to experimental measurements, including two-dimensional quantities and neutral particle physics. The simulations created for this thesis show a radiation distribution similar to the experimentally observed, but with a less pronounced X-point radiator. The inner target was in a detached state with the majority of the required pressure loss originating close to the target rather than in the edge. The outer target was not in the detached state, which was attributed to strong asymmetries and a lack of neutral particle density in the divertor.

The following chapters are structured as follows: Chapter 2 deepens the introduction of scrape-off layer and divertor physics to allow a better insight into the power exhaust problem. The

physics underlying the SOLPS-ITER code package are introduced in chapter 3. In chapter 4 the tokamak JET (Joint European Torus) and the most relevant diagnostics for the following experimental analysis are introduced in brief, accompanied by a short summary of divertor physics results in JET relevant for this thesis. The results of the neon-seeded JET experiments are presented in chapter 5, first phenomenologically for discharges of different heating powers and neon seeding strengths, followed by analyses of transport physics and impurity content. The chapter is completed with a database analysis including all the examined discharges which allows to depict findings related to density peaking, increasing energy confinement time, neutron rate, impurity content, and radiation distribution. A correlation between some key observations made in high heated, high seeded discharges is reported in this chapter. In chapter 6 the results from a series of neon-seeded SOLPS-ITER simulations are shown, examining the radiation distribution, the pressure drop towards the targets as well as the main and impurity ion distribution. Finally, the results of experimental and numerical analyses are summarised in chapter 7 and a conclusion for radiating regimes in future fusion machines is drawn.

2 Scrape-Off Layer and Divertor Physics

The divertor is a key element for power and particle exhaust in future fusion devices. Interactions of plasma particles with the wall material as well as with other ionised or neutral particles take to a particular degree part in the divertor. This chapter will first introduce the basics of divertor tokamaks, followed by a discussion of the plasma-wall interactions and volumetric processes. The basic divertor regimes are introduced, one of which is the so-called detachment which is characterised by reduced particle and heat fluxes to the divertor and which is hence the preferred regime for future reactors. Recent findings of experiments and simulations with detached divertor, impurity seeding, and high radiation are presented. Finally, the aspects most relevant for this thesis are briefly summarised.

2.1 Divertor Tokamaks

This section introduces the basics of the tokamak principle, along with its most relevant quantities and phenomena (subsection 2.1.1), the widely-used divertor configuration and its magnetic topology (subsection 2.1.2) as well as the high confinement mode (subsection 2.1.3).

2.1.1 The Tokamak Principle

In a magnetic field a charged particle is forced onto a gyrating motion perpendicular to the field. Its parallel velocity component, however, is not affected by the field, which allows to confine a plasma by a closed magnetic field. Due to the closure of the magnetic field, a magnetic confinement device typically is shaped like a torus. One major magnetic confinement configuration, and currently the most researched, is the tokamak.

Figure 2.1 shows the magnetic field components in a tokamak: The toroidal magnetic field B_ϕ (toroidal green arrows) is created by the toroidal magnetic field coils. Since inboard the coils are closer to each other, the magnetic field strength is higher. From Ampère's law the dependency $B_\phi \propto 1/R$ can easily be derived [18, ch. 3.1]. The inner side is therefore referred to as high-field side (HFS), while the outer side is called low-field side (LFS). R denotes the major torus radius, while in the following r shall denote the minor radius of the torus and a the minor radius of the last closed flux surface (LCFS, see below). The aspect ratio is given by R/a .

The differences in the magnetic field strength between LFS and HFS give rise to drift motions of the particles in vertical directions, resulting in a poloidal charge separation. To compensate such a charge separation, an additional poloidal magnetic field has to be introduced, which leads to a twisting of the magnetic field and along the field lines to Pfirsch-Schlüter currents

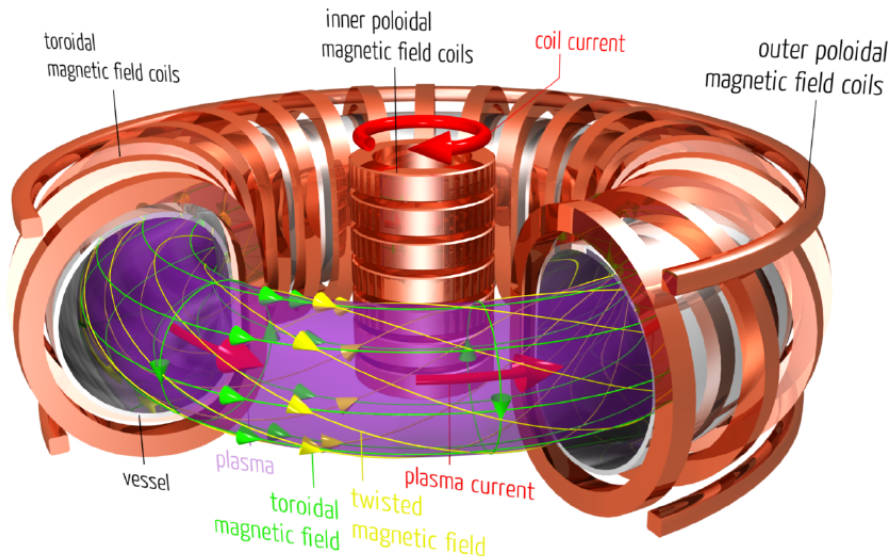


Figure 2.1: Basic principle of a tokamak: The toroidal magnetic field B_ϕ is created by the toroidal field coils, the poloidal magnetic field B_θ is generated by a current driven I_p by the central solenoid. Further poloidal field coils are used to shape and stabilise the plasma. Figure taken from [41].

that compensate the charge separation. The poloidal field component is generated by running a toroidal current through the plasma. This plasma current I_p (red arrow) is induced by a coil current in the central solenoid, leading to the formation of an additional poloidal magnetic field $B_\theta \approx \frac{\mu_0 I_p}{2\pi a}$ [42, ch. 1.3] (poloidal green arrow). The resulting twisted magnetic field $B = B_\phi + B_\theta$ (yellow arrows) provides a higher stability. Additional poloidal magnetic field coils are used to shape and further stabilise the plasma. The induction of the toroidal current requires a steadily increasing current through the central solenoid. This current is limited by technical restrictions and tokamaks can therefore not be run continuously, but in pulses (also called discharges or shots) of some seconds.

Global Tokamak Parameters

An important parameter for plasma stability is

$$\beta = \frac{nT}{B^2/2\mu_0}, \quad (2.1)$$

the ratio of kinetic to magnetic pressure. In tokamaks it is in the range of some percent [43]. To satisfy the Lawson criterion (Eq. 1.6) the density is ought to be high, while the magnetic field is supposed to be low for economical reasons. Therefore a high β is beneficial [44, ch. 3.1.1]. High values for β can also be achieved by favourable shaping of the plasma. Due to magneto-hydrodynamic (MHD) instabilities there is an upper stability limit to β [45] of

$$\beta \leq \beta_n \frac{I_p}{aB_\phi} \quad (2.2)$$

with $\beta_n = 2.8\%$. β_n can be compared to normalised values of β in the experiment [17]:

$$\beta_N = \frac{\beta}{I_p / (aB_\phi)} \quad (2.3)$$

This thesis will follow the common convention that β_N is displayed in %.

Since the energy confinement time τ_E depends on numerous transport processes [18, ch. 4.1] an estimate from a first principle model for future fusion devices is unattainable. However, a scaling over various engineering and physics parameters of current devices can give confident projections. The most widely used scaling in these days is the IPB98(y,2) scaling [46]. The ratio of experimentally measured τ_E to the value $\tau_{98(y,2)}$ predicted by the IPB98(y,2) scaling

$$H_{98(y,2)} = \frac{\tau_E}{\tau_{98(y,2)}} \quad (2.4)$$

gives an indication how an experiment is performing in terms of the energy confinement. To reach $Q = 10$ in ITER it is required that $H_{98(y,2)} = 1.0$ is reached at $\beta_N = 1.8$ [47]. In high radiation discharges the meaningfulness of the IPB98(y,2) scaling might be reduced, though, as only discharges with $f_{\text{rad}} \leq 0.6$ were included in the scaling [48].

Another limit to the operational space of a tokamak is posed by the density. From scalings it was found [49, 50] that an upper limit for the line-averaged density is given by

$$n_{\text{GW}} \approx \frac{I_p}{\pi a^2} \quad (2.5)$$

with n_{GW} being the Greenwald density in $1 \times 10^{20} \text{ m}^{-3}$, I_p the plasma current in MA, and a the minor radius in m. The Greenwald fraction is defined as ratio of the line-averaged density in the experiment to the Greenwald density: $f_{\text{GW}} = \bar{n}_e / n_{\text{GW}}$.

Disruptions

Reaching an operational limit such as the Greenwald limit can lead to a sudden end of a plasma discharge in a disruption [51, 52][18, ch. 7.7–7.9]. During a disruption the plasma confinement is lost, leading to high heat and particle loads on the walls as well as to a loss of the plasma current, which in turn induces magnetic and mechanical forces into the tokamak and its structure. Both, enormous heat and particle loads onto the wall, and high mechanical forces are very undesirable in fusion devices.

Close to the density limit a further increase of density leads to increased power losses by impurity radiation, analogously an increase of the impurity concentration will have the same result. Due to temperature, density, and impurity distributions the radiation will first increase toroidally symmetrical at the plasma edge, localised in a poloidal region of low temperature and high density, as a so-called MARFE (Multifaceted Asymmetric Radiation from the Edge) [53][7, ch. 3.5]. A MARFE can be unstable as the low temperatures in a MARFE cause a further increase of radiation as well as a local increase in plasma resistivity. As a consequence, the plasma current moves away from the edge and towards the core. This permits the development of MHD mode instabilities and finally the disruption. Around the X-point, however, stable MARFE-like regions with high radiation powers have been observed.

Also a drop of the heating power P_{heat} below the total radiation power $P_{\text{rad,tot}}$ can lead to a disruption. This can be caused in experiment by the temporal, mostly partial breakdown of the external heating systems. If the duration of this breakdown is, however, lower than τ_E , a disruption can be avoided.

Field Lines and Flux Surfaces

The magnetic field consists of a toroidal component B_ϕ and a poloidal component B_θ which leads to the field lines being twisted. Their poloidal position will hence not be constant on their course around the torus. A magnetic field line can be represented by the entire surface of constant magnetic flux on which the field line lies. A poloidal cross-section of a tokamak (like in Fig. 2.2 for JET) shows the nested surfaces of constant poloidal magnetic flux Ψ . Charged particles move on these flux surfaces, parallel to the magnetic field lines, and are only transported in perpendicular direction by collisions with other particles (classical/neoclassical transport) or by turbulence (anomalous transport). The magnetic field lines that intersect with a plasma facing component (PFC) are called open field lines, while the field lines that don't are called closed field lines. In between these two areas is the last closed flux surface (LCFS).

In experiment the normalised flux coordinate

$$\rho_{\text{pol}} = \sqrt{\frac{\Psi - \Psi_{\text{axis}}}{\Psi_{\text{sep}} - \Psi_{\text{axis}}}} \quad (2.6)$$

with Ψ_{axis} being the flux at the magnetic axis and Ψ_{sep} the flux at the separatrix is often used as a coordinate to assign the flux surfaces coordinate values between $\rho_{\text{pol}} = 0.0$ at the magnetic axis and $\rho_{\text{pol}} = 1.0$ at the LCFS. Sometimes also as ρ_ϕ , using the toroidal flux. The horizontal plane through the magnetic axis is called the mid-plane.

2.1.2 The Divertor Configuration

Magnetic fusion devices are currently primarily operated in two magnetic configurations: the limiter and the divertor configuration [42]. In the limiter configuration the LCFS is determined by the intersection of the magnetic field lines with the material surface of the wall or limiters,

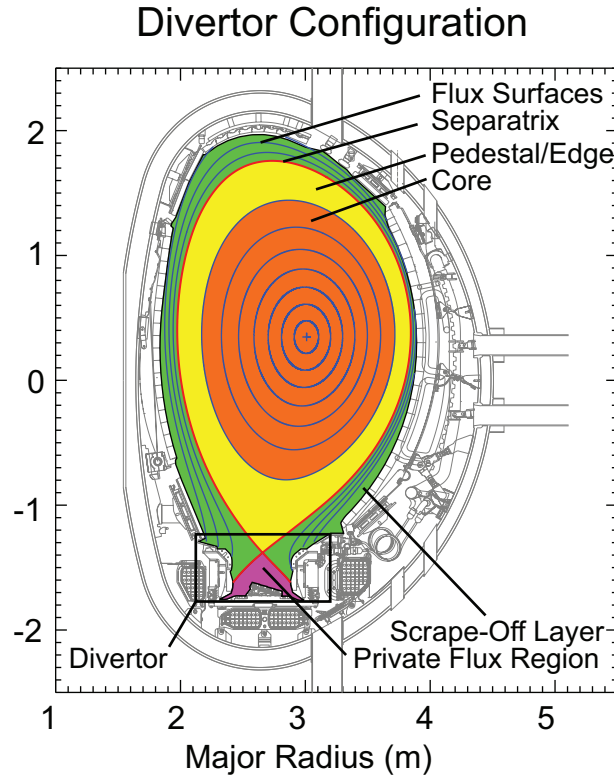


Figure 2.2: Poloidal cross-section through JET divertor configuration with the magnetic flux-surfaces (blue). The last closed flux surface, the separatrix (red), subdivides it into the confined region with closed field lines and the scrape-off layer with open field lines (SOL, green area). To distinguish the central area of the confined region with low tolerance for impurity concentration and radiation losses from the outer area which is preferred for radiation, in the framework of this thesis they are called "core" (orange area) and "pedestal area" or "edge" (yellow area). Note that these definitions might vary from such found in other sources and that the sharp separation between core and edge is only for illustrative purposes. The area with open flux surfaces below the X-point (purple area) is called private flux region (PFR). The divertor region is indicated by the black box, but is usually not precisely defined. The divertor configuration shown here and used in all experiments analysed in this thesis has the strike points on the vertical divertor target tiles (VV configuration).

which were toroidally installed specifically for this purpose. Due to the high particle and energy flux onto these surfaces, the surface material might be damaged, but more importantly material particles extracted from the limiter by sputtering [54] as well as helium from fusion processes and other impurities that recombined at this limiter surface can efficiently enter the confined region and pollute the plasma, with negative consequences for the fusion performance and plasma stability (see section 1.2).

In the divertor configuration the location of plasma-wall interaction is moved to a divertor region far away from the LCFS in order to reduce the plasma-wall interaction and impurity influx into the confined region. This is done by applying additional poloidal fields in a way that the LCFS, which in a divertor configuration is called separatrix, is no longer defined by its contact with the wall but rather by the shape of the field itself (see Fig. 2.2). The lower temperatures in the divertor are beneficial for the reduction of sputtering impurities (see section 2.2). Since the plasma-wall interaction does not take place in close proximity to the confined region, impurities

cannot directly enter the confined region anymore, no matter if they originate from sputtering, recycling at the wall, or deliberate seeding. Instead the higher neutral pressures in the cold divertor are assumed to facilitate a more efficient pumping of impurities and helium ash [55]. The spatial distance between the origin and the deposition location of power allows further to remove power by volumetric loss processes (see section 2.3) more easily.

The magnetic null point that forms in a divertor configuration, i.e. where the poloidal magnetic field is zero, is called X-point. Usually, modern tokamaks can be operated with one X-point being located in the lower half of the poloidal cross-section (lower single null, LSN), in the upper half (upper single null, USN) or with both X-points being located within the first wall (double null, DN). The intersection points with the wall (the so-called strike points) are located on target tiles which are specifically designed to withstand high heat loads. The magnetic field lines leading from the X-point to the strike points are called divertor legs. On their way to the targets the flux surfaces' radial distance and hence the area of a flux tube changes (flux expansion). Below the X-point an area with open field lines is formed, named private flux region (PFR). A measure for the shape of the poloidal cross-section is given by the so-called triangularity δ , which denotes the horizontal distance between the magnetic axis and the X-point (see e.g. [56] or [18, ch. 14.14] for a more detailed definition).

In modern plasma experiments the divertor configuration is predominant. The limiter configuration is often used nonetheless, especially during the ramp-up phase of a plasma discharge. While current devices are mostly operated with a single-null divertor, alternative geometry concepts like the snowflake divertor [57] with additional divertor legs or the super-X divertor [58], with one leg being extended to allow increased flux expansion and stronger spatial separation of the strike point from the plasma in the confined region, are currently being discussed and implemented in experiments for further investigation [59–61].

2.1.3 H-mode

In the ASDEX tokamak, the predecessor of ASDEX Upgrade, it was found that exceeding a threshold heating power leads to a transition to a regime with high confinement [62], the so-called high confinement mode or H-mode, in contrast to the regime before this transition which is called low confinement mode, or L-mode. The H-mode was since observed and examined in many other major magnetic fusion devices.

The transition from L-mode to H-mode can typically be detected by the formation of an edge transport barrier [63, 64], resulting in an increase of density and temperature gradients in the edge. As a consequence, a pedestal forms on which the stiff core profiles [65] seem to lie, thus elevating the core values (see e.g. Fig. 5.9 for L-mode and H-mode profiles of a neon-seeded discharge treated in this thesis). The formation of the edge transport barrier is assumed to be related to the suppression of turbulent transport by shear flows [66, 67]. It is envisaged that ITER [68] and DEMO [69] are operated in H-mode.

There is no consistent theory to derive the L-H transition threshold power P_{LH} which the power over the separatrix

$$P_{\text{SOL}} = P_{\text{sep}} = P_{\text{heat}} - P_{\text{rad,sep}} \quad (2.7)$$

has to exceed in order to reach H-mode. Therefore, it is usually derived from scaling laws that set the H-mode transition power in relation to physical and mechanical parameters of a multitude of discharges. The currently most widely used multi-machine scaling is the Martin or ITPA scaling [70], but also other scalings are used, depending on the specific machine or the parameter range to examine, e.g. [71–73]. It should be considered that the data used to derive such scaling laws can be restricted to certain parameter ranges or regimes. The ITPA scaling for example includes only data points with $f_{\text{rad}} \leq 0.5$ and should therefore be treated with caution when applying it on high radiation discharges.

The transition to H-mode can also be triggered by sawteeth. A sawtooth oscillation is an instability arising close to the magnetic axis, characterised by a slow increase of the core temperature, followed by a rapid decrease (hence the name) [18, ch. 7.6][22, ch. 5.3.3]. In the outer core regions the contrary is observed: a drop in core temperature leads to a heat pulse, which can also trigger the transition into the H-mode.

In the H-mode characteristic magnetohydrodynamic instabilities in the edge lead to a periodic collapse of the pedestal [74, 75]. Due to the release of energy and particles into the SOL concomitant with these edge localised modes (ELMs), they pose a threat for the wall and the divertor target material. In future fusion devices ELMs will have to be mitigated (like in ITER [68]) or completely avoided (like in DEMO [29]). ELMs are commonly categorised as type I, type II, and type III according to their frequency, their impact on the energy confinement, and other experimental characteristics [7, 75]. Type III ELMs for example are typically observed close to the L-H power threshold. High-frequent type III ELMs have smaller amplitudes than type I ELMs, which typically have large amplitudes but lower frequencies [18, ch. 7.17]. The energy confinement times of a type III ELMy H-mode is decreased with respect to type I ELMs, though. Type I and type III ELMs can be distinguished by an increase (type I) or a decrease (type III) of their frequency at an increase of heating power [75]. For type III ELMs, which typically occur close to the L-H transition, this can lead to an ELM-free H-mode phase. However, such a variation of heating power is not always feasible and in the case of strong radiation from the confined region also difficult to judge.

A regime found intermediate between L-mode and H-mode is the M-mode. An M-mode is a weak ELM-less H-mode regime found at JET [76, 77]. It can typically be observed right after an L-H transition. In an M-mode a typical $n = 0$, $m = 1$, with n, m being the toroidal and poloidal mode numbers, magnetic oscillation can be observed in pedestal, scrape-off layer, and divertor measurements [78]. It has to be distinguished from type III ELMs which are less periodical than the oscillation associated to the M-mode [78, 79]. The M-mode is similar or equal to plasma states close to the L-H transition described in other experiments, e.g. at ASDEX Upgrade it is called I-phase [80, 81], at EAST [82], and HL-2A [83] it is described as a Limit Cycle Oscillation. The I-phase appears prior to all L-H transitions and exhibits oscillations which are considered to be related to type III ELMs [84]. M-mode and I-phase are widely considered identical [78, 79, 85]. For the present study the M-mode is considered to be indicative for a situation where the power flux through the separatrix is close to the L-H threshold power.

It was observed in experiment that a maximum density exists for which the H-mode is still able to exist [86–88]. This maximum is typically found at Greenwald fractions of 0.8–1.1. Approaching this H-mode density limit leads first to a transition from type I ELMs to type III ELMs or

to a phase of dithering between H-mode and L-mode. In contrast to the Greenwald limit, the H-mode density limit does not lead finally to a disruption, but to a back-transition into L-mode. Even though phenomena like detachment or strong radiation close to the X-point were observed as well in vicinity of the H-mode density limit, they do not seem to be the cause for the back-transition from H-mode to L-mode [86–88].

2.2 Plasma-Wall Interaction

The interactions between plasma particles and wall material are fundamental for the operation of fusion experiments as they heavily impact the power and particle balance: the walls constitute a major power sink and a source for fuel and impurity particles. This section therefore introduces several aspects of plasma-wall interaction, namely the sheath in subsection 2.2.1, the recycling and sputtering of particles from the wall into the plasma in subsection 2.2.2, and the limit to power deposited onto the wall material in subsection 2.2.3.

2.2.1 The Sheath

Due to the higher electron thermal velocity, an electric potential forms close to the wall. Within a region of the size of some Debye lengths, called the sheath, this potential accelerates ions towards the wall while electrons are repelled. According to the Bohm criterion [89–91] the ions enter the sheath at velocities equal to or larger than the ion sound speed $v_{se} \geq c_{s,i} = \sqrt{\frac{T_e + T_i}{m_i}}$. However, the total power density deposited onto the target not only originates from the power transmitted through the sheath with a sheath heat transmission coefficient $\gamma \approx 7-8$, but also from ions recombining at the targets, thus depositing their binding energy on them [17, ch. 16.2.3]:

$$q_{\text{tot}} = (\gamma T_t + W_{\text{rec}}) \Gamma_t \quad (2.8)$$

From Eq. 2.8 it becomes clear that reducing only the target temperature is not sufficient in order to reduce the heat flux density but also a reduction of the total particle flux Γ_t is necessary.

2.2.2 Recycling and Sputtering

Depending on the initial energy E_0 of an atom or ion striking the wall, it undergoes either a reflection with energy $E < E_0$, an adsorption at the surface or an absorption in the upper layers of the wall and subsequent re-release into the plasma with a thermal velocity according to the wall temperature, or an absorption at deeper layers of the wall where it will be trapped (retention) [42, ch. 3]. In the first two cases an incoming ion is most likely to be re-emitted as a neutral since the wall is charged negatively due to the higher electron thermal velocities. This process is called recycling. In most cases the recycling flux from the walls constitutes the major particle source of the plasma.

In all of the above cases the particle transmits parts of its initial energy to the wall atoms. The energy transferred in a collision between plasma and wall particle can exceed the binding energy of the material's atomic lattice and hence single wall atoms be extracted from the wall [92, ch. 6]. This process is called physical sputtering. A measure for the sputtering is the sputtering yield Y which denotes the number of sputtered particles per incoming particle. In the case of physical sputtering $Y(E_0, M_1, M_2)$ depends on the impact energy as well as the masses $M_{1,2}$ of the involved particles. Physical sputtering has only a low dependency on the wall temperature. Generally, the physical sputtering yield for deuterium is lower the heavier the wall material atoms are. Even though the physical sputtering yield is higher for incoming impurity ions with a higher mass, the seeding of impurities can be necessary in order to reduce the impact energy and the number of deuterium ions impacting onto the wall and hence reduce the sputtering of tungsten particles which can migrate into the core and put the plasma stability at risk. This is the case in the discharges examined in this thesis.

Chemical sputtering instead denotes the overcoming of the wall atom's binding energy by a chemical potential and the formation of molecules including wall and plasma atoms [54]. Especially in machines with carbon walls, the formation of hydrocarbons can strongly contribute to the introduction of wall impurity atoms into the plasma. Chemical sputtering can take place at low impact energies, depends strongly on the wall temperature, and the chemical sputtering yield can reach the same orders of magnitude as physical sputtering. The chemical sputtering yield decreases with increasing ion flux onto the wall [93].

Especially sputtered wall particles which got ionised and transported again towards the wall can sputter more efficiently, the so-called self-sputtering. The re-deposition of sputtered material, also at other than their original position, and also co-deposition of hydrogenic plasma particles, which in a fusion experiment includes tritium, are possible. Due to its low sputtering yield at typical edge temperatures, tungsten is foreseen as divertor material in ITER [94] and was tried in many current machines like JET or ASDEX Upgrade in the past decade. It often replaced the previously widely-used carbon, which also has the disadvantage of binding radioactive tritium in hydrocarbon molecules, despite the harm it might create in terms of radiation (see subsection 2.3.2).

2.2.3 Power Deposition Limit

In the development of the divertor in future machines, the peak heat flux density onto the divertor target is one of the most relevant quantities. In order to avoid damages to the target, e.g. by sputtering, melting or evaporation, the peak power flux has to be limited. It is distinguished between the steady state heat load and the transient heat load which includes temporarily higher fluxes due to ELMs or disruptions, which are to be mitigated or avoided in future machines for this reason. Current tungsten targets in development for ITER are capable of tolerating peak power fluxes up to 10 MW/m^2 (steady state) and 20 MW/m^2 (slow transient heat load). For DEMO similar values are assumed with an active cooling by water or later maybe helium [95] of the divertor target material. An overview over the material science behind the target development is provided in [96]. However, in the case of DEMO the material additionally has to withstand the bombardment of neutrons and radiation. This irradiation can cause further

damages to the targets and enhance existing erosion mechanisms. The radiation power flux density in the divertor is estimated to be below 2 MW/m^2 [31] (or even below 1 MW/m^2 [97]), the power flux by neutrons around 1 MW/m^2 [31]. Including some security margin, this reduces further the tolerable steady state heat load to about 5 MW/m^2 which requires high radiative power fractions.

2.3 Volumetric Processes

Ionised and neutral particles not only undergo reactions with wall atoms but also amongst each other. They constitute source and sink terms for the particle densities (including the various charge states), momentum, and energy, and therefore determine the (local) state of a plasma as well as the radiation characteristics. This section briefly introduces the different types of ion-neutral interaction in subsection 2.3.1 and the ways in which a fusion plasma emits electromagnetic radiation in subsection 2.3.2.

2.3.1 Ion-Neutral Interactions

In a fusion plasma the following reactions have to be considered:

- **Ionisation/Excitation:** The impact of a free electron can either remove another bound electron from a neutral or partially ionised atom or excite it from a lower-energetic level to a higher-energetic level [98].
- **Recombination:** The recombination of an ion and an electron to a neutral or partially ionised atom takes effect in three different ways [99, ch. 54–55]: radiative recombination, dielectronic recombination, and three-body recombination. Due to the continuous kinetic energy distribution of the electrons also the emitted radiation is continuous [100].
- **Charge Exchange:** At the collision of an ion and a neutral atom the ion can strip one of the valence electrons from the atom, incorporating it in one of its energy states.
- **Molecular Physics:** Molecular reactions include dissociation of a molecule, dissociative ionisation, molecular ionisation, dissociative recombination, and dissociative excitation [18, ch. 9.6].

The reaction rates of these collisional reactions can generally be represented as

$$S_i = n_1 n_2 \langle \sigma_i v \rangle \quad (2.9)$$

where S_i denotes the rate density of process i (in $\text{m}^{-3}\text{s}^{-1}$), $\langle \sigma_i v \rangle$ its temperature-dependent reaction rate coefficient (in m^3s^{-1} , see Fig. 2.5), and n_1 and n_2 the densities of the respectively involved species. The rate densities can also be interpreted as source or sink terms, which plays an important role in coupling codes which separately calculate the fluid equations and the

neutral particles. In coupled numerical simulations, elastic collisions between plasma particles are treated in the fluid equations, e.g. as friction forces. However, elastic collisions between neutral and ionised atoms also create friction and viscous forces [18, ch. 5.4]. Neutral-neutral collisions can be ignored in current divertor plasmas [101].

2.3.2 Plasma Radiation

The sources of electromagnetic radiation, with discrete or continuous spectrum, depend directly on the population densities that are governed by the interactions introduced above. In particular, the dominating radiation sources in a plasma are:

- Line radiation: The de-excitation of an electron (spontaneous or by electron impact (dielectronic recombination) [18, 99, 102]) causes the emission of a photon. The discrete spectral lines and their profile shapes can be utilised for diagnostic purposes [103].
- Recombination radiation: see above.
- Bremsstrahlung: An electron that is deflected by the electric field of an ion or partially ionised atom emits bremsstrahlung. The total power radiated by bremsstrahlung can be calculated to be [18, ch. 4.25][22]

$$P_{\text{br}} = 5.35 \cdot 10^{-37} n_e^2 Z_{\text{eff}}^2 T_e^{1/2} \text{ Wm}^{-3} \quad (2.10)$$

The bremsstrahlung depends strongly on electron density and the effective charge

$$Z_{\text{eff}} = \frac{\sum n_Z Z^2}{\sum n_Z Z} = \frac{\sum n_Z Z^2}{n_e}, \quad (2.11)$$

with n_Z being the ion density of the species with charge state Z and assuming quasi-neutrality for the second equality. The bremsstrahlung spectrum is continuous. In DEMO bremsstrahlung is foreseen to contribute about 90 MW to the radiation power [35] from the confined region.

- Synchrotron (cyclotron) radiation: The gyro-motion of charged particles in the magnetic field leads to the emission of synchrotron radiation. The characteristics of the synchrotron radiation depends on local quantities, like temperature, density, and magnetic field. For this reason, synchrotron radiation originates mostly from the region with the highest temperatures, namely the core. Synchrotron radiation power is usually negligible in current devices and only low in ITER, since the plasma is optically thick to the fundamental frequency of the synchrotron radiation [18, ch. 4.25] and most of the radiation is re-absorbed by the plasma. It can be used for diagnostic purposes, nonetheless. In future machines, however, the synchrotron radiation power will be larger due to higher core temperatures and therefore higher powers will be able to leave the plasma (26 MW in DEMO [35]; it is even considered as a mean to increase the radiation power with less impurity seeding [104]).

The knowledge of population densities of the various charge states of an atomic species can be used to determine the related radiative emissions. The population densities for each state and the radiation power can be received from a collisional-radiative model which couples the rate equations of the various states. The model can assume a wide range of complexity, depending on the underlying assumptions and considered reactions. One of the simplest models is the coronal equilibrium, which assumes a balance between electron impact ionisation and excitation, and spontaneous de-excitation and recombination in a system with uniform densities and temperatures [42, ch. 3.5]. It is assumed that the spontaneous decay occurs on a shorter time-scale than excitation and that the excitation is only from the ground state [34, ch. 2.1.3]. The coronal equilibrium is independent of the density. However, the coronal equilibrium is not sufficient to describe a fusion plasma as with higher density de-excitation by electrons and three-body-recombination play a larger role and would have to be included in a collisional-radiative model. In general, it can be assumed that the plasma is optically thin and that radiation can propagate outward onto the walls, but for some frequencies the re-absorption and the effect of photo-ionisation have to be considered as well, e.g. for the Lyman lines [105],[106, ch. 3.4]. The synchrotron radiation contribution can often only be included in such models as estimates as it depends strongly on the temperature, density, and magnetic field profiles [34, ch. 2.4]. In a collisional-radiative model in local equilibrium, transport effects are not considered but they might lead to higher radiation powers [42, ch. 3.5],[107]. This can be modelled by the coupling of a transport code and a code containing the atomic reaction rate coefficients. The code package SOLPS-ITER used in this thesis (see chapter 3) couples the fluid code B2.5 and the Monte Carlo neutral code EIRENE, which makes it a useful tool to analyse the radiation in a fusion plasma.

The entirety of the power losses caused by the different radiation mechanisms can be summarised in the definition of a cooling factor $L_Z(T_e)$:

$$P_{\text{rad}} = \sum_Z n_Z n_e L_Z(T_e) \quad (2.12)$$

Figure 2.3 depicts the cooling factor for various elements [34, 108] from a collisional-radiative model. From known temperature and density distributions a prediction can be made in which region the power losses will be increased by impurities.

In the core, where T_e is in the order of some keV, the light species are fully ionised and in a pure deuterium plasma bremsstrahlung would dominate. Even at the high core temperatures heavy atoms like tungsten impurities from the wall are not fully ionised [109]. Thus, they do not only increase the bremsstrahlung from the core by increasing Z_{eff} in Eq. 2.10 but can also emit additional line radiation. Increasing the radiation power in the core and diluting the fusion fuel with impurities, especially the heavy ones which tend to accumulate in the core more easily [110–112], can cause instability and even the disruption of the plasma. They can therefore only be tolerated in lowest concentrations $c_Z = n_Z/n_e$ (e.g. maximum of around $c_Z = 1 \times 10^{-5}$ – 1×10^{-4} for tungsten or xenon [33, 34, 113]) in order to still fulfil the conditions for a burning plasma.

In the rather cold ($T_e < 100$ eV) and less dense SOL and divertor regions bremsstrahlung does not play a role anymore and instead line radiation of light species, especially deuterium, can be observed. The low temperatures also permit the recombination of ions and electrons and

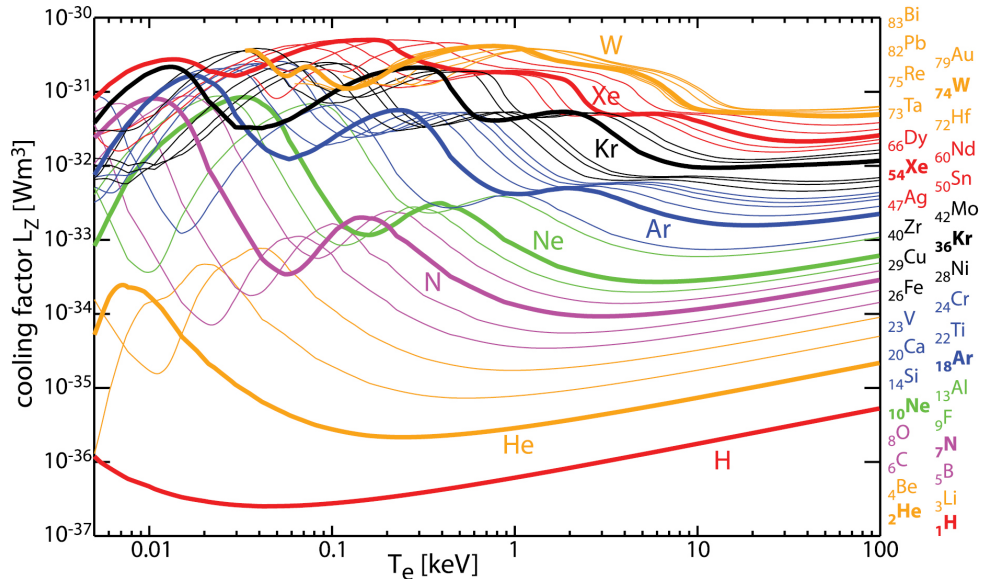


Figure 2.3: The cooling factor L_Z as function of T_e for several elements, calculated from a collisional-radiative model at $n_e = 5 \times 10^{19} \text{ m}^{-3}$. It can be used to estimate the regions of radiation losses by impurities. While at lower temperatures the profiles of L_Z reflect the atomic structure of the atoms, at higher temperatures the $T^{1/2}$ dependency in the bremsstrahlung power loss equation Eq. 2.10 leads to an increase of all profiles. Taken from [34].

the associated recombination radiation. In the pedestal region intermediate between the core and the SOL the effects just described overlap. While the hydrogenic fuel species are already fully ionised, lighter impurities like nitrogen or neon might not be and contribute line and recombination radiation. Since the emission of radiation means a loss of power, this might also affect the pedestal shape and the stability of the plasma.

2.4 Divertor Regimes

It is essential for the integrity of the divertor target material to reduce the temperature in its vicinity and the particle flux onto it. Due to the position of the only heat source in the main plasma and the SOL transport processes acting along the field lines towards the divertor, the conditions of the divertor depend on the conditions at the separatrix. In SOL and divertor physics one-dimensional models are often used for simplification of the complex processes taking place in this area [114, 115]. Figure 2.4 shows the geometry of such a simple model to illustrate the energy and particle fluxes in the high recycling regime. For more sophisticated analyses two-dimensional codes like SOLPS or EDGE2D-EIRENE have to be used. In the following, the different divertor regimes are introduced, using a simplifying one-dimensional picture. In particular, in this section the parallel heat transport (subsection 2.4.1), the recycling regimes in the divertor (subsection 2.4.2), the detachment (subsection 2.4.3), and how the latter can be induced by impurity radiation (subsection 2.4.4) are introduced.

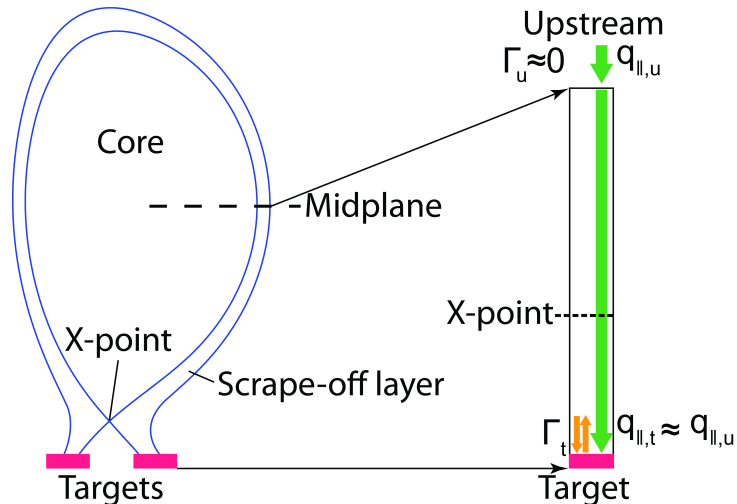


Figure 2.4: Simplifying one-dimensional geometry in the case of the high recycling regime: The heat flux $q_{||}$ is assumed to enter at the midplane/upstream position and to be conducted to the target. The particle flux Γ_t on the target is only fed from ionisation processes close to the target. Perpendicular fluxes are neglected.

2.4.1 Heat Transport

Apart from the power losses from the atomic reactions introduced above, collisions between particles also constitute a mean of energy transport. At a sufficiently high collisionality the plasma can be treated as a fluid and two major energy transport channels can be distinguished in the fluid equations: convection and conduction. For simplicity, the energy transport from an upstream position to the target is considered only in one dimension on a coordinate $s_{||}$ parallel to the magnetic field lines. From the energy conservation equation Eq. 3.7 of the Braginskii equations [116] a relation for the one-dimensional energy flux along a magnetic field line coordinate $s_{||}$ can be deduced:

$$q_{||} = q_{||,\text{conv}} + q_{||,\text{cond}} = \left(\frac{1}{2}mv^2 + \frac{5}{2}T \right) nv - \kappa_0 T^{5/2} \frac{dT}{ds_{||}} \quad (2.13)$$

where v is the fluid velocity. This equation can be applied to electrons as well as to ions. The first term can be associated with convective energy transport while the second represents conductive heat transport as derived by Spitzer and Härm [117]. $\kappa_{0,e} \approx 2000 \text{ W}/(\text{m eV}^{7/2})$ and $\kappa_{0,i} \approx 60 \text{ W}/(\text{m eV}^{7/2})$ denote the respective heat conductivities of ions and electrons [42, ch. 9.6]. Due to their higher mass, the ions contribute significantly more to the convective transport at high Mach numbers, while the conductive transport is dominated by the electrons since $\kappa_{0,e} \gg \kappa_{0,i}$.

For the existence of a temperature gradient between the upstream position and the targets it plays a major role if energy is transported towards the divertor by convection or by conduction and hence which term is predominant. In the extreme case in which the heat is only transported by convection the SOL properties are determined by the sheath (sheath-limited regime). In the

other case, the conduction-limited regime, the heat is transported through the SOL purely by conduction. In the latter case convective transport can still take place in the sheath and through ionisation processes, especially within the divertor, but is not dominating. The term “limited” here only means a limitation of SOL properties like temperature and density, not of power flux to the target which is given by the confined region nonetheless [42, ch. 1.9].

The temperature gradient is reduced when convective heat transport is dominant, hence the target and the upstream temperature are similar. Conductive heat transport instead is more effective the larger the temperature gradient. Usually, in the divertor low temperatures are desired while upstream higher temperatures are preferred for higher core temperatures. The resulting temperature gradient towards the target favours conductive heat transport. However, in DIII-D it was shown that even under detached (see below) conditions significant convective transport can be observed in large parts of the SOL, driven by parallel flows as well as by perpendicular $E \times B$ drift flows [118]. Diffusive radial particle transport can also contribute to convective energy transport.

2.4.2 Recycling Regimes

For the particle transport in the SOL the continuity equation Eq. 3.5 holds, neglecting the impact of drifts and resulting currents such as the Pfirsch-Schlüter currents. In equilibrium condition the SOL particle flux is then determined only by ionisation sources. It can be distinguished between two major divertor regimes, basically depending on the main plasma density [119, Fig. 8],[42, ch. 16.3], hence the collisionality, hence the location in which ionisation takes place. At low main plasma densities charged particles enter the SOL only upstream by radial transport across the separatrix and are then transported towards the target sheath. Due the low collisionality they do rarely undergo interactions and ionisation sources in the SOL can be neglected. For this reason this regime is called low recycling regime. The particles are recycled at the target and enter the confined region as neutrals where they are ionised again.

At high densities and thus high collisionalities recycled neutrals cannot penetrate in the confined region anymore as they are ionised primarily in the vicinity of the targets, i.e. in the SOL or in the divertor. As convection is low, this high recycling regime is also a conduction-limited regime, but not necessarily vice versa, and due to its high densities and lower target temperatures it is more favourable for a fusion device.

2.4.3 Detachment

It was first discovered in L-mode experiments [119] that the further increase of fuelling and thus the upstream density above a so-called ‘roll-over’ point did not lead to a further increase of the density in front of the target but to a decrease. This decrease in target density is correlated to a decrease of the target particle flux. The target temperature continues to decrease, though, and has reached values of $T_e \lesssim 5 \text{ eV}$. The terms target temperature and target density here means the plasma temperature and density in front of the target rather than the temperature and density of the target itself. Such a state with both, low target temperature and low target

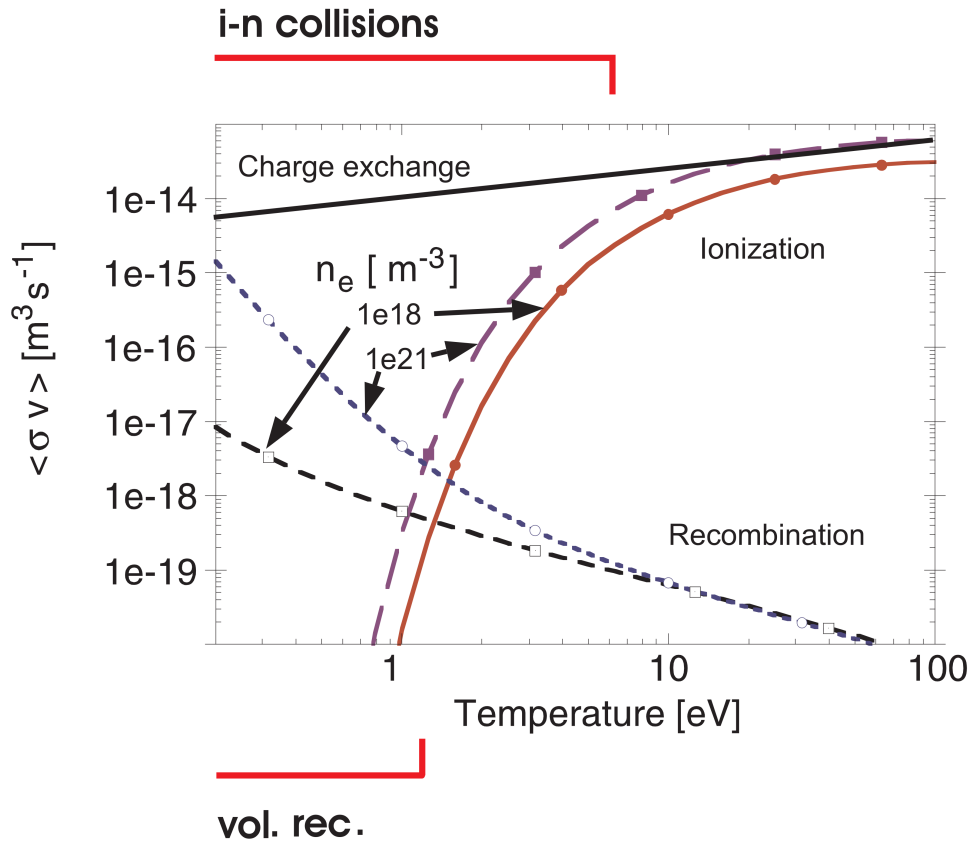


Figure 2.5: Reaction rate coefficients of the SOL processes charge exchange, ionisation, and recombination for hydrogenic atoms. At temperatures below 10 eV the ionisation rate decreases, allowing the charge exchange to become relatively stronger. For temperatures below 2 eV the recombination is stronger than the competing ionisation. The bifurcation of the recombination at low temperatures for different densities shows the impact of three-body recombinations compared to radiative recombination. Taken from [121, Fig. 32].

particle flux is called detachment. It is highly favourable for the operation of a future fusion experiment [120], where it will be reached by increasing the SOL radiation losses rather than by ramping up the density. This is also the case for most of the current experiments.

The processes leading to detachment can be characterised by the temperature distribution along a SOL flux tube, giving rise to the according volumetric processes (see Fig. 2.5):

- The increase of density leads to an increase in radiative power losses (see Eq. 2.12) in the upstream SOL above the X-point which are responsible for the low divertor temperature. Injecting impurity gases into the plasma in order to increase radiative power losses is an equivalent way to decrease the divertor temperature.
- For regions of the flux tube in which $T_e > 10$ eV ionisation is significantly stronger than recombination, hence the flux tube above the recycling region can be treated as in the case of the high recycling regime. With the onset of detachment the volumetric ionisation source moves upstream, i.e. away from the target [120].

- For temperatures $T_e \lesssim 5$ eV the ionisation rate is low compared to that of ion-neutral interactions, such as friction and charge exchange processes. Such processes remove momentum from the plasma, allowing a drop of the pressure in the divertor.
- In the case that close to the target temperatures of $T_e \lesssim 1$ eV are reached the recombination becomes very efficient, dominating over the ionisation. The plasma particle sink has changed from being a target recombination sink to being a volumetric recombination sink. Thus, the particle flux onto the target is very low to non-existent and recombination radiation leads to further dissipation of energy. The neutral density increases at the target, facilitating the work of the divertor pumps.

The loss of pressure between the midplane position and a target can be used to determine if the target is detached while a drop of target temperature alone is not sufficient to determine detachment. While the necessity of SOL radiation losses is undisputed, the relative importance of ion-neutral interactions and recombination for the detachment process in theoretical models is still being discussed ([42, 55, 114] and [115, 122, 123]). The onset of recombination can be seen as a criterion for detachment, nonetheless. In fact, if the upstream radiation losses lead to a reduction of the ionisation source, recombination is the only way to further reduce the particle flux onto the wall [115]. Instead of the roll-over of the target density the exceeding of a threshold value $\{p_{\text{up}}/q_{\text{r}}\}_{\text{crit}}$ (≈ 15 N/MW for deuterium plasmas) can also be used to define the onset of detachment [115]. Physically this can be explained by the necessity for a minimum heat flux q_{r} into the recycling region to drive the ionisation necessary to sustain the upstream pressure p_{up} .

During a ramp-up of density or equivalently of SOL radiation it can be observed that first the ion flux of flux tubes close to the separatrix decreases while in the outer SOL the ion target flux is still increasing [124]. This situation of detachment restricted to only parts of the target close to the separatrix is called partial detachment. With increasing density or radiation a radial growth of the detached region takes place, until the strong radiation moves away from the targets. A very strong reduction of the ion flux to the target is called complete or full detachment.

2.4.4 Detachment by Impurity Radiation

To reach detachment more easily than by ramping up the density and provide a channel for power exhaust the deliberate puffing of impurity gases into the plasma is indispensable. A model derived by Lengyel [125] estimates the radiation power in the SOL for reaching detachment. Assuming that radiation in the SOL is the only mechanism for dispersing power, the following relation is found [55, ch. 6.4]:

$$q_{\text{u}}^2 - q_{\text{r}}^2 = \frac{1}{3} \kappa_0 c_Z L_Z p_{\text{u}}^2 (T_{\text{u}}^{3/2} - T_{\text{r}}^{3/2}) \quad (2.14)$$

q_{u} and q_{r} denote the power flux densities at the upstream position and at the begin of the recycling region, T_{u} and T_{r} the respective temperatures, p_{u} the upstream pressure, and $c_Z = n_Z/n_e$ and L_Z the concentration and the radiative cooling factor of element Z . According to this equation, the radiation losses in the divertor cause a temperature gradient along the SOL. Since T_{u} is quite invariable the radiation is proportional to the upstream density, which is a desirable

feature in view of high fusion gains. From this model the criterion $c_Z \propto n_u^{-2}$ for the impurity concentration necessary to reach detachment by impurity radiation can easily be derived. In recently published results from spectroscopic analyses with nitrogen at ASDEX Upgrade ([126], based on [127]) and from numerical simulations with neon for ITER [128, 129]) similar relations have been found. In the latter study a dependency $c_Z \propto n_u^\alpha$ was observed, with α ranging from -2 for high divertor radiation powers to -4 in the case of low divertor radiation power. In case of high radiation the radial transport losses were increased, allowing a lower c_Z at low densities to radiatively dissipate the power flux. Another recent empirical scaling by Reinke [130] can be used to estimate the impurity fractions necessary to mitigate heat fluxes in future devices.

Equipping many major tokamaks with a tungsten divertor, as foreseen for ITER, allowed dedicated experiments to examine the reduction of the target power fluxes by means of divertor and SOL radiation in an environment more similar to ITER or DEMO. The power decay length Eq. 1.8 can be used to derive an important qualifier [131, 132]: since λ_q can be considered independent of the major radius R [133] the ratio P_{sep}/R gives a measure of the heat flux to be dissipated by radiation in the divertor and the SOL. The more general formulation for the overall power dissipation is P_{heat}/R . For ITER a value of $P_{\text{sep}}/R = 15 \text{ MW m}^{-1}$ is foreseen [25], for DEMO values of $17\text{--}20 \text{ MW m}^{-1}$ are estimated [134]. However, note that small variations in this parameter can have a tremendous impact on the machine design [35].

2.5 Impurity Radiation

High-radiating operational scenarios for next-step fusion devices like ITER and DEMO require strong extrinsic impurity seeding [26, 29, 68, 135] and, thus, many dedicated experiments have been performed for many years to analyse thoroughly the impact of impurities and their radiation on various operational aspects. In the following a brief overview over experimental and numerical findings regarding the impact of radiation from SOL, edge, and core on the plasma is given.

2.5.1 Impurity Radiation Species and Poloidal Distribution

Since for ITER only SOL and divertor radiation will be mandatory, the focus in the more recent experiments was on maximising the radiation from these regions. The poloidal temperature distribution in today's medium-sized and larger machines are mostly such that nitrogen is ideal for increasing the divertor radiation, argon and krypton for core radiation [25] and neon in the SOL and the pedestal region. For reaching ITER-relevant exhaust scenarios therefore nitrogen was often used as seed impurity. In the future neon might be a more adequate seed impurity for divertor radiation in ITER since nitrogen might form ammonia molecules with the radioactive tritium [136, 137], leading to various operational issues. In current fusion devices tritium is almost never used (only in rare, dedicated experimental campaigns like the ones at JET [138]) and nitrogen is therefore (for now) most suited for increasing the divertor radiation. Also other seeding impurities, preferably noble gases, like neon, argon, and krypton, as well as combinations of different impurities were examined in current devices.

2.5.2 X-Point Radiation

During the detachment process it was often observed that the zones of strong radiation moved away from the targets towards the X-point where it finally concentrated inside the separatrix [124]. This phenomenon was suspected to be similar to a MARFE (Multifaceted Asymmetric Radiation from the Edge) which might cause disruptions (see subsection 2.1.1). A MARFE is a self-amplifying radiation condensation instability [53],[18, ch. 7.16]. The X-point region might be prone to develop such an instability due to the high flux expansion in that region, i.e. a larger volume between flux surfaces and more efficient cooling, and due to the vicinity to the main fuel/recycling and impurity source, the divertor [55, ch. 6.6]. Drift effects might amplify this effect [55, ch. 6.8 & 9.3]. The energy lost by radiation in this region leads to lower temperatures. In some temperature ranges (see Fig. 2.3) a decrease of temperature can lead to an increase of L_Z , to an increase of radiation and therefore to a further decrease of temperature. Furthermore, the constant pressure along the flux surfaces leads to a particle flow into this region. The concomitant higher density also leads to higher radiation power. The X-point MARFE is often observed to be stable, though [139, 140]. There might be several reasons for this [115]: the high density might cause an increased diffusion of deuterium and impurities away from the MARFE; the thermal force $F_T = \alpha_T \nabla_{\parallel} T$ tends to push impurities towards regions of higher temperatures. Both effects might eventually lead to an equilibrium state.

2.5.3 SOL and Divertor Radiation

A P_{sep}/R value of 10 MW m^{-1} was reached in nitrogen-seeded ASDEX Upgrade discharges while the target power flux density remained below 2 MW/m^2 [25]. With increasing detachment a strongly radiating zone inside the separatrix developed near the X-point. The outer target was defined to be in pronounced detachment, i.e. a large drop in pressure and heat flux was observed over several power decay lengths without being in complete detachment. The pronounced detachment lead to reduced confinement ($H_{98(y,2)} = 0.7\text{--}1.1$), attributed to the detachment and partly counter-acted by the nitrogen seeding. Furthermore, higher pedestal and core densities (while the temperature decreased) and a lower ELM size are reported [25].

In ASDEX Upgrade discharges with lower heating powers ($P_{\text{heat}} = 6\text{--}12 \text{ MW}$) complete detachment was achieved with nitrogen seeding [139] at a radiative power fraction of $f_{\text{rad}} = 0.8\text{--}0.9$. It was observed that the advancing detachment of the outer divertor target was correlated to the radiation zone moving from the outer divertor into the confined region at the X-point, to ELMs transiting from type I to type III and finally at complete detachment to their mitigation, and to a pressure loss at the pedestal, first only by a decreased temperature profile and at complete detachment affecting the density profile as well as the temperature profile. An increasing nitrogen concentration lead to a movement of the X-point radiator further inside the confined region, suggesting a possible control mechanism for its position. When only the inner divertor was detached and the outer attached, at sufficient heating powers on the high field side a region of high density was observed in the outer SOL [141] which also impacts the fuelling of the pedestal [142]. The high field side high density is suppressed by the seeding of nitrogen and was also observed at JET.

At JET nitrogen seeding experiments displayed similar characteristics [37, 143]: full divertor detachment was reached and the strongest radiation was observed at the X-point. Compared to a similar, but unseeded discharge, the electron density was increased in the core and decreased at the pedestal region, i.e. a higher density peaking, while the electron temperature was increased only in the core. This leads to an improvement of the confinement factor from $H_{98(y,2)} = 0.65$ (unseeded) to up to $H_{98(y,2)} = 0.75$ (nitrogen-seeded, at $f_{\text{rad}} = 0.50$). However, these values are clearly lower than the $H_{98(y,2)} = 1.0$ aimed for at ITER. The ELMs were either completely mitigated ($P_{\text{heat}} = 18$ MW) or type I ELMs ($P_{\text{heat}} = 27$ MW). In the 18 MW discharges increased nitrogen seeding lead to the transition into an ELM-free regime (the M-mode, see section 5.2). It was found that at $f_{\text{rad}} = 0.60$ the divertor radiation reached a peak. The maximum achieved radiative power fraction in these experiments was $f_{\text{rad}} = 0.75$, which in view of the completely detached targets raises questions with regards to the accuracy of the single components of the power balance. A thorough analysis of the uncertainties of the power balance [144, 145] has not yet come to a final conclusion.

2.5.4 Core Radiation

Argon and krypton are mostly used as core radiators in today's machines, in the future xenon might become a possible candidate as well. To ensure low divertor temperatures from the beginning of the discharge (to avoid tungsten sputtering), these gases are often injected after an initial nitrogen puff. At ASDEX Upgrade krypton seeding caused a radiating poloidal ring in the pedestal [140], causing an f_{rad} of up to 0.90 and a detached divertor. The increased pedestal density and the low ELM frequency (reduced by the strong core radiation, as one would expect from type I ELMs [75]), however, can render the discharge unstable when the ELM flushing of krypton outwards can no longer counterbalance the inter-ELM inward transport (see e.g. [146] for more details on neoclassical impurity transport in the edge). At JET krypton also increased the radiation in a poloidal ring at the pedestal which caused a dithering between L-mode and H-mode [140]: while in H-mode the density pedestal caused an inward transport of krypton, it was flushed out in L-mode. The transition seems to be triggered by the closeness of P_{sep} , which is reduced by krypton radiation in the pedestal, to the L-H transition threshold power P_{LH} .

Argon was seeded at ASDEX Upgrade in conjunction with nitrogen seeding, resulting in high radiation powers (15 MW in the core, 5 MW in the divertor, of total $P_{\text{heat}} = 23$ MW) while simultaneously maintaining an H-mode with good energy confinement (probably due to the nitrogen), without pedestal degradation, and detached targets [132]. Only the ELM frequency was observed to be decreased due to the strong core seeding, leading eventually to a tungsten accumulation in the core. More generally, it was observed in ASDEX Upgrade discharges with high core radiation from argon or krypton that the ELM behaviour is affected by the divertor neutral pressure [25]: at low/medium pressure the type I ELM frequency is decreased by the impurity seeding, rendering the discharge unstable; at high pressure the ELMs become smaller and more frequent, which is attributed to the higher pedestal collisionality. The energy confinement is reduced as a downside effect of the high pressure. The reduction of the type I ELM frequency with increasing radiation in the outer core by argon, and, thus, reducing P_{sep} , was also reported from JT-60U [147], where the argon seeding additionally lead to an increased confinement due to a more peaked density profile with a degraded pedestal due to dilution effects

and a concomitant temperature increase. Recently, a scenario with argon as pedestal radiator in an ELM-less regime was tested at ASDEX Upgrade [148]. In purely argon seeded discharges at JET instead only a minor improvement of confinement was seen for low radiative power fractions, while it declined at higher ones (around half of the radiation power coming from the core region) [37]. The discharges eventually underwent back-transitions to L-mode. In fact, the proximity of the discharges to the L-H power threshold seems to play a major role. This was underlined also by a study conducted at Alcator C-Mod [149] in which high energy confinement factors of $H_{98(y,2)} \geq 1.0$ were found for cases when P_{sep} of impurity (nitrogen, neon, argon) seeded discharges was just slightly above P_{LH} . Furthermore, the seeding of nitrogen was also the basis of mixed-impurity discharges in JET in which smaller amounts of neon or argon were added into an already nitrogen-seeded discharge [143]. While with neon the X-point radiation increased, with only minor growth of the core radiation, argon led to stronger core radiation at similar divertor radiation levels. Both impurities had in common that they further increased the energy confinement factor of the nitrogen-seeded discharge to values of $H_{98(y,2)} = 0.78$.

2.5.5 Edge Radiation

While nitrogen radiates primarily in the divertor and argon/krypton strongly in the core (even though, they show strong radiation peaks also at low temperature ranges), neon is most suitable to examine radiation in the SOL and the pedestal region. So far, it seems difficult to handle, though: At ASDEX Upgrade [140] neon seeding led to an improvement in energy confinement by an increase in pedestal density. However, this high pedestal density led to an increased inward transport of neon and tungsten, eventually causing a reduction of the ELM frequency due to their radiation, a further impurity accumulation in the core due to less impurity flushing by ELMs, and finally a disruption. Also the reports from JET had indicated that a stable H-mode could not be achieved and phases of back-transitions into L-mode during which the targets re-attached took place [140]. The H-mode phases turned out to be ELM-less for $f_{\text{rad}} > 0.50$. The typical X-point radiator was more extended into the inner and outer divertor during L-mode phases and more localised at the X-point in H-mode [37]. A maximum in the divertor radiation was found for $f_{\text{rad}} \approx 0.50$ and the confinement factor increased up to values of around $H_{98(y,2)} = 0.80$ for the maximum $f_{\text{rad}} \approx 0.65$. From discharges with higher heating powers a decrease of the type I ELM frequency with increased neon puffing was reported [150].

2.6 Numerical Simulations of Detached High Radiation Experiments

Experiments have been accompanied by numerical simulations for a long time in order to reproduce experimental results, explore physics questions that are inaccessible by experimental means, and extrapolate findings to a broader parameter range. At JET for example numerical simulations were used to reproduce first experimental results found in nitrogen-seeded detached discharges [151], among them the strong radiation at the X-point. Also at other machines numerical simulations have been used in order to examine the relevant processes in seeded, detached plasmas: At ASDEX Upgrade SOLPS5.0 simulations successfully managed to reproduce the experimentally observed correlation between the X-point MARFE, a loss of pedestal top pressure,

and complete detachment of the outer target in nitrogen-seeded discharges [152]. It turned out that the activation of drift terms in the simulations were deciding for the reproduction of the high field side high density region [153]. In a SOLPS5.0 study the radiation properties and divertor compression of argon seeded into ASDEX Upgrade was discussed [154]. The transport of nitrogen and argon in the divertor of ASDEX Upgrade was examined with SOLPS5.0 [155] and SOLPS-ITER [156]. SOLPS-ITER simulations with comparison to experimental observations in neon-seeded plasmas were also performed at EAST [157]. A comparison between nitrogen-seeded and neon-seeded simulations of ASDEX Upgrade and ITER was performed in order to determine machine size dependencies and the suitability of these two impurities as divertor radiators in ITER [158]. Neon and nitrogen show to radiate equally well in the divertor region, both being able to lead to a partial detachment of the targets, as is required for ITER. Drift effects play a much minor role in the ITER divertor than in that of ASDEX Upgrade. This is not only connected to the larger machine size of ITER but also to the high neutral pressures in ITER [159]. Drifts were also shown to stabilize the X-point radiator in ASDEX-Upgrade [160].

The capabilities of modelling were also used after the new tungsten divertor was built in, in order to compare the detachment processes in JET with carbon wall (JET-C) and JET with an ITER-like tungsten divertor (JET-ILW). In EDGE2D-EIRENE simulations with both divertors and in reasonable agreement with the experiment, volume recombination was found to be the main contributor for a deep divertor detachment [161]. Another study using EDGE2D-EIRENE featured the seeding of nitrogen up to radiative power fractions of 0.5, in which not only the experimentally observed increase of divertor radiation and the decrease of heat flux could be reproduced but also a correlation between the formation of a radiating zone in the SOL on both sides of the X-point with the transition to detachment was found [162]. In similar numerical simulations with nitrogen seeding the impact of different divertor geometries on detachment was analysed. The outer vertical target detaches at lower densities and reaches lowest heat fluxes at lower radiation powers than in the horizontal target configuration [163]. Neon-seeded experiments have been used as a benchmark for simulations with COREDIV in order to analyse global trends of power dissipation [150, 164].

2.7 Brief Summary and Outline of This Thesis

Tokamaks are currently the most researched magnetic fusion devices and therefore the basis for plans of future fusion reactors like DEMO. Such a reactor will have to run in the high confinement mode (H-mode). A divertor will be indispensable for the removal of impurities and power. However, the particle and energy fluxes have to be limited in order to protect the divertor targets, preferably by detachment of the targets. In order to remove the power before it reaches the target as well as to assist the transition to detached targets, the radiation power is increased by the seeding of impurities. While high radiation in the divertor area has been well researched in recent years, the effects of impurity radiation from inside the separatrix are not yet fully understood. Impurities could dilute the core or their radiation might deteriorate the stability of the H-mode or even the entire discharge. In this thesis dedicated neon-seeded experiments performed at JET were examined in order to find ways to increase the total radiative power fraction as well as the impact of the poloidal radiation distribution on the confinement and the plasma stability. In these experiments an ELM-less H-mode regime (M-mode) was found, in

which strong radiation around the X-point, a reduced density pedestal, and a detachment of the targets could be observed. The code package SOLPS-ITER was used to numerically reproduce trends found in the experimental analysis regarding the poloidal radiation distribution and the correlation of the X-point radiator, the drop of pedestal pressure and the detachment of the targets. In the simulations neon led to an increase of core and pedestal radiation as well as to a pre-form of the X-point radiator. The inner divertor was in detachment, though not due to the decrease of the pedestal pressure. The attached outer divertor target as well as the low radiation powers are attributed to the low density in the divertor.

3 The SOLPS-ITER Code Package

In an experimental setup the measurement of physical quantities is restricted by the space that is available for diagnostics and even the number of experiments itself is limited. A numerical simulation of a scenario similar to the experiment can overcome these limitations and provide a deeper insight into the physics of the SOL and of detachment. Not only can simulations be used to validate experimental data but also to discover trends by parameter variations and to make predictions for experiments (including future ones [165]) [122, ch. 3]. The numerical tool used in this thesis is the SOLPS-ITER code package. SOLPS stands for Scrape-Off Layer Plasma Simulation. SOLPS-ITER is the latest version of this code package, maintained by the ITER Organisation [39, 40]. SOLPS consists of two major parts: The plasma fluid code B2.5 [166] and the Monte Carlo neutral code EIRENE [167, 168]. They are briefly described in the first two sections of this chapter. They are coupled by particle, momentum, and energy source/sink terms [169]. Additionally, the code package provides tools for the generation of the B2.5 and the EIRENE meshes and for the generation of input files. Section 3.3 will introduce the physical basis of the fluid code B2.5 and of the Monte Carlo neutral code EIRENE before the general workflow of SOLPS-ITER simulations is presented. The most relevant parameters set in the simulations performed in the framework of this thesis are introduced in section 3.4.

3.1 The Plasma Fluid Code B2.5

3.1.1 Braginskii Equations

In kinetic theory the behaviour of a system characterised by a 6-dimensional single-particle distribution function $f(\vec{r}, \vec{v}, t)$ is described by the Boltzmann equation:

$$\frac{\partial f(\vec{r}, \vec{v}, t)}{\partial t} + \vec{v} \cdot \frac{\partial f(\vec{r}, \vec{v}, t)}{\partial \vec{r}} + \frac{q}{m} (\vec{E} + \vec{v} \times \vec{B}) \cdot \frac{\partial f(\vec{r}, \vec{v}, t)}{\partial \vec{v}} = \left. \frac{\partial f(\vec{r}, \vec{v}, t)}{\partial t} \right|_{coll} \quad (3.1)$$

The term on the RHS of the equation represents collisions between unlike particles. While kinetic theory comes in handy for the characterisation of plasma phenomena on a microscopic level, it is not suited for large systems with many particles. To compare numerical simulation results with experimentally observed data or phenomena a description of the plasma by macroscopic quantities is preferable.

Assuming short, compared to the size of the system, mean free paths between collisions of like particles and hence assuming the velocity distribution to be a Maxwellian, the macroscopic quantities and their conservation equations can be received from the velocity moments of the

single-particle distribution function (derivation by Braginskii [116], also presented in detail in [170, ch. 3] or in [17, ch. 7.4]).

The following equations for the macroscopic quantities density, mean velocity, and temperature can be derived from the unknown single-particle distribution function $f(\vec{r}, \vec{v}, t)$ by multiplication with a power of the velocity and an integration over the velocity space:

$$n(\vec{x}, t) = \int f(\vec{r}, \vec{v}, t) d^3\vec{v} \quad (3.2)$$

$$\vec{u}(\vec{x}, t) = \frac{1}{n} \int \vec{v} f(\vec{r}, \vec{v}, t) d^3\vec{v} \quad (3.3)$$

$$T(\vec{x}, t) = \frac{1}{n} \int \frac{m}{3} (\vec{v} - \vec{u})^2 f(\vec{r}, \vec{v}, t) d^3\vec{v} \quad (3.4)$$

In a similar way the conservation equations for these quantities, namely the continuity equation and the conservation equations for momentum and energy, can be derived from Eq. 3.1:

$$\frac{\partial n}{\partial t} + \nabla \cdot (n\vec{u}) = S_n \quad (3.5)$$

$$\frac{\partial}{\partial t} (mn\vec{u}) + \nabla \cdot (mn\vec{u}\vec{u}) + \nabla p + \nabla \bar{\Pi} - qn(\vec{E} + \vec{u} \times \vec{B}) = \vec{R} + \vec{S}_u \quad (3.6)$$

$$\frac{\partial}{\partial t} \left(\frac{3}{2} nT + \frac{mn}{2} \vec{u}\vec{u} \right) + \nabla \cdot \left[\left(\frac{5}{2} nT + \frac{mn}{2} \vec{u}\vec{u} \right) \vec{u} + \bar{\Pi} \cdot \vec{u} + \vec{q} \right] - qn\vec{E} \cdot \vec{u} = \vec{R} \cdot \vec{u} + Q_{ei} + S_E \quad (3.7)$$

S_n , \vec{S}_u , and S_E denote source terms for particles, momentum, and energy. \vec{R} is a friction term arising from collisions between ions and electrons and Q_{ei} the heat transferred in such collisions. $p = nT$ is the scalar pressure, $\bar{\Pi}$ the stress tensor and \vec{q} the heat flux density (not to confuse with the scalar particle charge q). Even though these fluid equations were derived under the assumption of small mean free paths, it turns out that they keep their validity also when this condition is not strictly fulfilled [42, ch. 1.6], which makes them a reasonable tool to examine the SOL.

Each of the above conservation equations contains a quantity of a higher order of \vec{v} , e.g. the density n determined by Eq. 3.5 contains the mean velocity \vec{u} that is determined by Eq. 3.6, which in turn depends on the temperature T (through $p = nT$) that is only determined in Eq. 3.7, which contains the heat flux density \vec{q} , and so on. The set of equations can be closed by relating a high-order term to a lower-order term, which can be achieved in various ways, e.g. by setting $p = 0$ or by using an isothermal or adiabatic equation. Besides \vec{q} the quantities \vec{R} , $\bar{\Pi}$, and Q_{ei} are yet to determine. A closure of the above equations was presented by Braginskii [116], assuming a high collisionality and conductive parallel transport as described by Spitzer

and Härm [117]. The Braginskii equations finally contain only terms depending on n_e , n_i , \vec{u}_e , \vec{u}_i , T_e , and T_i .

In B2.5 the Braginskii equations are discretised as described in [101, 121] by applying them on a two-dimensional finite volume grid that is aligned with the magnetic flux surfaces [122, ch. 3] (see Fig. 3.2 for an example). This allows a separation of parallel and perpendicular transport processes. In contrast to the more illustrative physical grid for the actual computations this grid is converted to a regular-sized computational grid (see Fig. 3.4) by “cutting” through the X-point and unfolding the grid. The fluid equations are converted from the physical poloidal coordinate system to the computational cartesian coordinate system accordingly. Additional guard cells on the boundaries of the computational grid allow the boundary conditions to be set individually for the north boundary (corresponding to the SOL boundary of the physical grid), the east and west boundaries (outer and inner target, respectively), and the south boundary (core/PFR).

3.1.2 Perpendicular Transport

The transport perpendicular to the magnetic field plays a crucial role for the energy and particle confinement and hence the conditions in SOL and divertor. To include perpendicular (or radial) transport in numerical codes as SOLPS-ITER is therefore indispensable. The radial particle and heat transport can be described by three theories: the classical transport theory assumes collisions between particles in the absence of or presence of only homogeneous, non-curved, and time-invariable electromagnetic fields [171], the neoclassical theory which describes the transport by collisions of plasma particles on trajectories along inhomogeneous, curved magnetic field lines (and hence including also e.g. trapped particle orbits or drift effects) [172], and the transport induced by turbulence, called turbulent or anomalous transport (see [44, 46] and references therein). While the theory of the former two is rather complete, the usually dominating latter one is still being investigated. In the absence of a full physics model the perpendicular transport processes can only be approximated. The perpendicular particle transport is usually represented by a diffusive ansatz:

$$\Gamma_{\perp} = -D_{\perp} \frac{dn}{dr} + vn \quad (3.8)$$

$D_{\perp}(r)$ is the diffusive transport parameter and $v(r)$ the pinch velocity which accounts for convective transport. Due to quasi-neutrality the equation rules for both, electrons and ions. A similar ansatz can be pursued for the radial heat transport:

$$q_{\perp} = -n_e \chi_e \frac{dT_e}{dr} - n_i \chi_i \frac{dT_i}{dr} + \frac{5}{2} \Gamma_{\perp} (T_e + T_i) \quad (3.9)$$

The first two terms on the RHS represent diffusive conductive heat transport with the effective diffusive heat transport parameters $\chi_{e,i}$, the second term corresponds to convective heat transport according to Eq. 3.7. While in the classical transport theory the transport parameters are in the range of $D_{\perp} \approx \chi_{e,i} \approx 1 \times 10^{-4} - 1 \times 10^{-5} \text{ m}^2/\text{s}$ and in neoclassical theory in the order of

magnitude of $D_{\perp} \approx 1 \times 10^{-3} \text{ m}^2/\text{s}$ and $\chi_{e,i} \approx 1 \times 10^{-2} \text{ m}^2/\text{s}$, in the experiment much higher values in the order of $D_{\perp} \approx \chi_{e,i} \approx 1 \text{ m}^2/\text{s}$ are found [43, ch. 14].

In SOLPS-ITER the 1D transport parameters $D_{\perp}(r)$, $v(r)$, $\chi_e(r)$ and $\chi_i(r)$ can be set, either as a radially constant value or as a radial profile. The pinch velocity is usually, as in this thesis, neglected, i.e. $v(r) = 0$, and D_{\perp} is then adapted to include also non-diffusive transport effects. The radial variation of the transport parameters allows the more accurate benchmark with experimental profiles and to replicate transport barriers, such as the one leading to the formation of a pedestal in H-mode. Radial source terms might be included as well, e.g. the power and particle deposition profiles of heating systems. Additionally, viscosity and drift terms can be activated separately [121, ch. 6]. Drift terms account for distortions of the single particle gyro-motion by external forces and inhomogeneities of magnetic field or particle distribution that are not included in the fluid theory and cause additional cross-field transport. These are in particular the $E \times B$ drift with drift velocity

$$v_{E \times B} = \frac{\vec{E} \times \vec{B}}{B^2} \quad (3.10)$$

and the diamagnetic drift

$$v_{\text{dia}} = \frac{\vec{B} \times \nabla p}{qnB^2}. \quad (3.11)$$

The additional terms can strongly impact the simulation results. Their activation can be cumbersome and makes the simulation runs more time-consuming. They are therefore often neglected, even though in some cases they can significantly improve the results, e.g. in [153]. Also in this work the drift terms were neglected.

3.2 The Monte Carlo Neutral Code EIRENE

The fluid approach could theoretically also handle neutral particle transport. Their low density, however, makes neutral-neutral collisions quite seldom and their collision mean free path (mfp) exceeds the SOL width by far [122, ch. 3.2]. The ion-neutral collision mfp is shorter and the poloidal variation of the mfp limits this approach to very few regions. Neutrals must therefore not be treated by the fluid but by the full kinetic equations. This is done in EIRENE by a Monte Carlo approach in which test particles are launched on a background plasma, which in the case of SOLPS-ITER is taken from B2.5. Probability then determines their reactions with plasma ions, and atomic and molecular reactions. The underlying methods of linear transport stem from the 1950s when they were developed for the calculation of neutron transport [173, 174].

A detailed mathematical description of neutral transport can be derived from the Boltzmann equation Eq. 3.1 (see [101, ch. 1.2] or [168, ch. 1]), but for understanding the basic method used in EIRENE to simulate neutral particle transport (called analogue sampling) it is sufficient to describe and emulate the processes represented by this mathematical description:

- A neutral particle is started from a source which can be a point, a surface, or a volume.

- It follows a straight trajectory until it collides with a background particle or with a wall surface.
- A collision can change the particle's velocity and type.
- The particle is tracked until it is absorbed or ionised.

The flight length L which a test particle that is emitted from a source or from a collision traverses before undergoing another collision is determined from the inverse cumulative distribution function

$$F(L) = 1 - \exp\left(-\int_0^L \frac{\nu(\vec{r}, \vec{v})}{|\vec{v}|} dl\right) \quad (3.12)$$

with $\lambda(\vec{r}, \vec{v}) = \frac{|\vec{v}|}{\nu(\vec{r}, \vec{v})}$ being the mean free path and $\nu(\vec{r}, \vec{v})$ the collision frequency [101, 175]. The flight length is then sampled from the integral

$$\int_0^L \frac{\nu(\vec{r}, \vec{v})}{|\vec{v}|} dl = -\ln(u) \quad (3.13)$$

where u is a computer-generated pseudo-random number in $[0, 1]$. The collision frequency $\nu(\vec{r}, \vec{v})$ is calculated from a plasma background that in the case of SOLPS-ITER is provided by the fluid code B2.5. At the location of the collision, the type of the collision is also determined by random numbers, on the basis of probabilities from the plasma background and atomic databases, like AMJUEL [176] and HYDHEL [177] for atomic and molecular data, TRIM [178] for surface interaction data, and ADAS [179] for photon emission coefficients. Average values for the plasma source terms of particles, momentum, and energy can then be calculated from a multitude of particle histories. EIRENE runs on a three-dimensional tetrahedral grid, which for the coupling with B2.5 is reduced to a two-dimensional triangular grid, which basically coincides with the B2.5 grid and is then extended to the vessel walls (see Fig. 3.3 for an example). For more detailed information about neutral transport in EIRENE the reader is referred to [101, 168, 175, 180].

The application of a Monte Carlo code provides the advantage that many atomic and molecular physics effects and divertor geometry can be included in the model [122, ch. 3.2]. This includes wall sources at the locations of real-experiment gas valves, particle-absorbing surfaces as a proxy for a pump, and many plasma-wall interactions like recycling and absorption. Also the possibility to consider neutral-neutral collisions and line radiation transport in EIRENE was included, which might become important in the dense divertor of ITER [181]. However, in nowadays devices like JET it is negligible and can therefore be left out to save calculation time. In general, the Monte Carlo approach is very time-consuming compared to a fluid code. Lately, this disadvantage could be compensated partly by enabling the code to be executed in parallel on several CPU cores. Furthermore, the numerical noise from EIRENE is introduced also into the fluid code via the source terms. This issue is currently further examined and possible solutions to minimise the noise's impact and increase the simulation's accuracy are provided [182–184].

3.3 SOLPS-ITER Workflow

The full workflow of the SOLPS-ITER package is shown in Fig. 3.1 [39]. The details of this workflow [39, 185, 186] shall be briefly introduced in this section, starting from the initial creation of a SOLPS-ITER case and going to the actual simulation run and its input/output. In this section programme names will be written in **bold**, file names in *italic*.

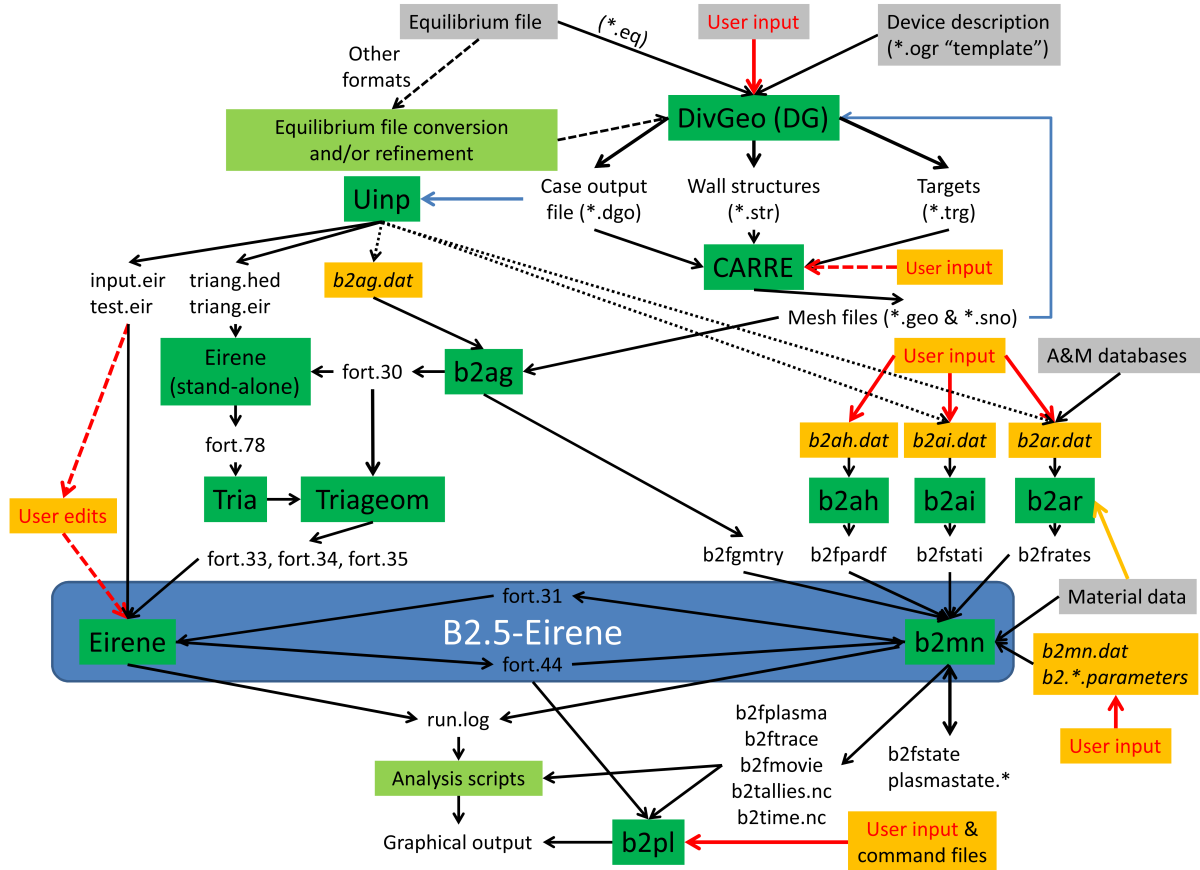


Figure 3.1: The workflow of SOLPS-ITER. Taken from [39].

DivGeo (DG): The creation of a SOLPS-ITER run requires information about the vessel geometry of the device to be simulated as well as a magnetic equilibrium of this device. **DivGeo** is the basic tool whose graphical user interface allows to put this information and others, like spatial extension of the plasma fluid grid, wall properties, puff and pump locations, and involved atomic species, together and to modify them.

Carre: From the output files of **DG**, **Carre** generates the computational mesh for **B2.5**.

Uinp: The output of **DG** and **Carre** are used by **Uinp** to create on the one hand **b2a*** input files and other **B2.5** input files, and on the other hand the input files for **EIRENE** (*input.eir/input.dat*) and the calculation for the triangular **EIRENE** mesh.

Tria/Triageom: To create the **EIRENE** triangular mesh, **Tria** first triangulates the space that is not covered by the physical **B2.5** mesh. In the following, **Triageom** creates the triangles

inside the **B2.5** mesh. The information about all the triangle nodes and their connections to each other and to the **B2.5** mesh are stored in the *fort.3[3-5]* files for **EIRENE** to read them.

b2a*: The first run of **B2.5** is preceded by the creation of relevant input files from the corresponding *b2a*.dat* files. The code **b2ag** prepares the mesh geometry file *b2fgmtry*, **b2ah** the default physics parameter file *b2fpardf*, **b2ai** the initial plasma state *b2fstati* (which for simplicity is assumed with constant densities in all mesh cells), and **b2ar** the atomic physics rates file *b2frates*.

b2yt: Not shown in Fig. 3.1 is **b2yt**, a tool that can be used to convert existing cases. The user can chose to change the **B2.5** mesh size and to remove atomic species from the case. A re-run of some of the programmes described above is necessary afterwards to provide the correct input files.

EIRENE: the Monte Carlo neutral transport code **EIRENE**, requires *input.dat/input.eir* input file and *fort.3[3-5]* files with mesh data.

B2.5: the plasma fluid code **B2.5**, requires the input files from **b2a*** (v.s.) and the main input file *b2mn.dat*. In this last file the settings made in the other files can be overwritten and the usage of additional input files can be activated. These are in particular: *b2.neutrals.parameters* with parameters for the neutrals treated by **EIRENE**, *b2.boundary.parameters* to set the boundary conditions, *b2.transport.parameters* and *b2.transport.inputfile* for transport settings (the latter one especially to prescribe radially varying transport parameters), *b2.numerics.parameters* to allocate computation time to single regions e.g. to speed up convergence of this region, and *b2.sources.profile* to define additional, radial source profiles e.g. to simulate the deposition profiles of particles and power by the NBI.

B2.5-EIRENE Coupling: The core modules of the code package can be found in the blue box. The plasma solution of **B2.5** is passed via the *fort.31* file to **EIRENE** which starts its test particles on this background and with the source terms contained in it. The averaged source terms are passed back to use in the fluid equations during the next iteration of **B2.5** through the *fort.44* file.

Output files: The run of SOLPS-ITER is stopped by reaching a maximum number of iterations, computation time, or another convergence criterion (all set in *b2mn.dat*). During the run many data are stored in *run.log*. Which information are given out is also set in *b2mn.dat*. The final plasma state is stored in *b2fstate* which can easily be re-used as *b2fstati* for the next run of the SOLPS-ITER case. The various output files can then be read in by evaluation scripts, be it one like **b2plot** which is part of the SOLPS-ITER package or others set up by the user. In this thesis both, batch scripts and the python tool **SOLPSpy** which was kindly provided by I. Paradela Perez and F. Hitzler from IPP Garching, are used.

3.4 Simulation Setup in This Thesis

The SOLPS-ITER code package offers a multitude of possible boundary conditions, with which numerical simulations can be conducted. This section introduces the setup of the simulations presented in this thesis, in particular how the simulations are run in practice, the B2.5 and EIRENE numerical grids, puffing and pumping for controlling the particle content, the atomic and molecular physics reactions taken into account as well as the conditions set at the grid boundaries.

3.4.1 Running the Simulations

The workflow in section 3.3 describes mostly processes that are run automatically or manually only at the setup of a simulation case. This section shall therefore give a short overview over settings and routines applied to run the SOLPS-ITER simulations for this thesis in everyday practice. Before the actual run, it is important to prepare the multitude of input files. This is described in subsection 3.4.2 for the grid, in subsection 3.4.3 for the neutral particles, in subsection 3.4.4 for the atomic and molecular physics, and in subsection 3.4.5 for the boundary conditions. The simulations are then submitted to the TOK server of IPP Garching. This allows to run the simulations in parallelised mode which especially benefits the run time of EIRENE. Before each submission the maximum number of iterations or the maximum calculation time can be set, whereas the latter has proven to be more practical on a server with a fixed maximum calculation time per calculation job. After completion the convergence of the case should be checked. Unfortunately, the convergence of a SOLPS-ITER case is not mathematically defined. In [40] some criteria are proposed to define convergence and were partially adapted in this work: A case is defined converged if plasma temperature and density at the midplane separatrix position do not change by more than 1% of their value over the course of one run with a rough simulation time of 0.2s. Numeric noise introduced in the simulations by the Monte-Carlo neutrals is included in this statement. This approach was chosen since the particle as well as the power sources in the simulation of this work are placed at the core boundary and transport is far lower in the core compared to the SOL. It was planned to use particle and power balances as further convergence criteria, but finally not applied due to difficulties in the practical implementation. Additional analyses of the simulation results might be necessary since converged simulations are not necessarily physically meaningful. The final state of the simulation can then be used as initial state for a new run.

3.4.2 Physical Grid (B2.5)

The template of the JET-ILW vessel geometry is similar as in [187] and was kindly provided by S. Wiesen from Forschungszentrum Jülich. The magnetic equilibrium that serves as basis of the grid was taken from the unseeded reference discharge JPN 84884, $t = 51.255$ s, but can be used for seeded simulations as well since in the experiment the magnetic field and the plasma current were kept constant for all discharges presented in this work.

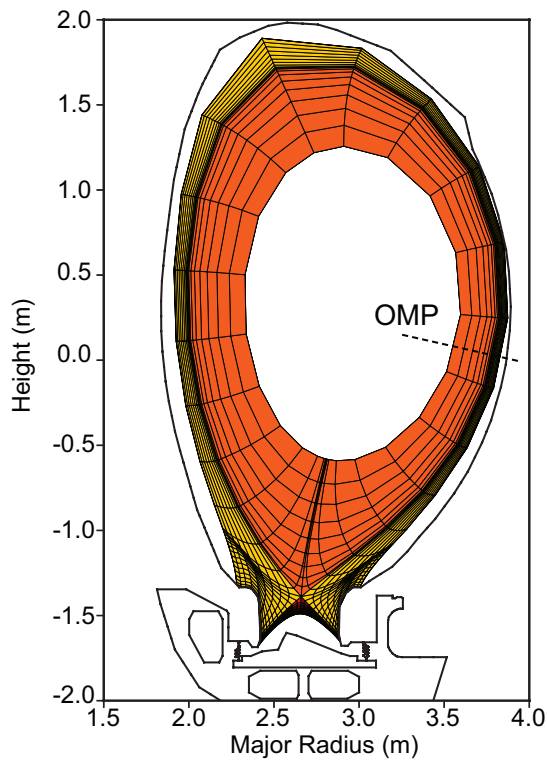


Figure 3.2: B2.5 physical grid (48×18) used in this thesis. In the grid 4 areas can be distinguished (corresponding to same-coloured areas in Fig. 3.4): the core (orange), the SOL (yellow), the inner and the outer PFR (light and dark red, barely visible here). The outer mid-plane (OMP) position is marked.

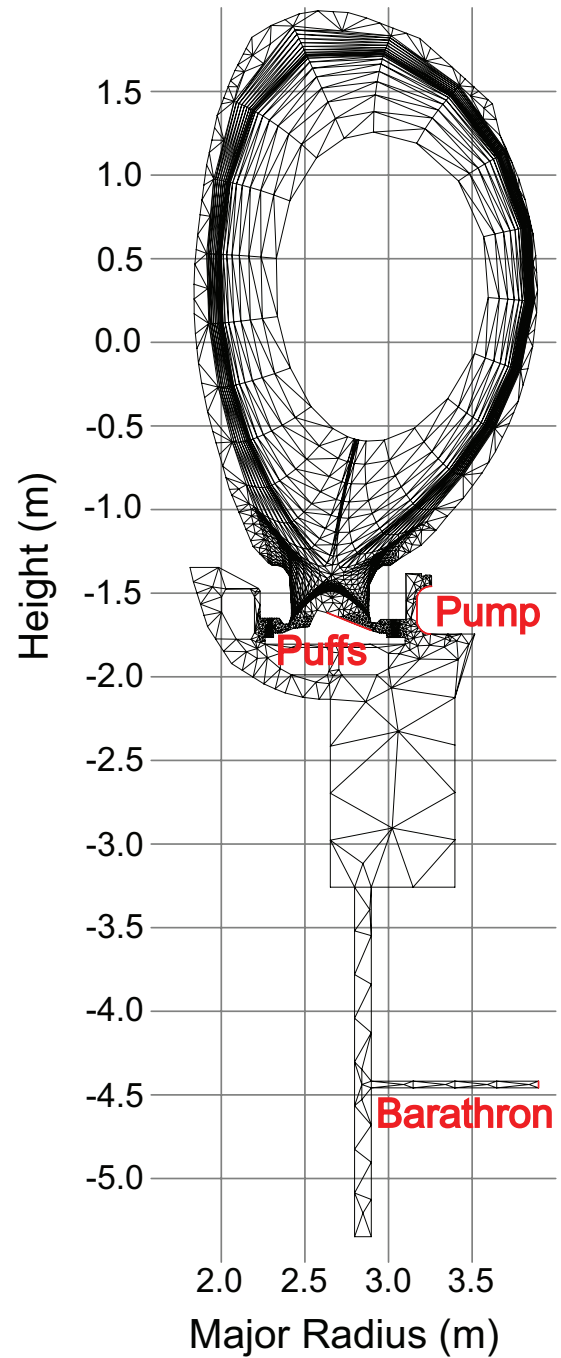


Figure 3.3: EIRENE triangular grid used in this thesis. The locations of the pump (simulated by surfaces with a reflection coefficient < 1), the puffs (deuterium and neon; not used in the simulations presented in this thesis), and of the pressure gauge in the experiment which can be used for comparisons of the sub-divertor pressure.

The width of the B2.5 physical grid (see Fig. 3.2) is limited on the SOL side by the first contact with the wall above the outer midplane. The width of the private flux region (PFR) is limited by the low strike point positions on the target. The grid was chosen to reach up to $\rho_{\text{pol}} \approx 0.69$ on the core side in order to take into consideration that neon might impact the outer core region as well. Originally, in DivGeo a grid with resolution 192×72 was created, but was scaled down to 48×18 in order to allow a faster convergence of the cases.

3.4.3 Pumping and Puffing in EIRENE

The JET-ILW template used here also includes the sub-divertor area which is therefore also covered by the EIRENE triangular grid (see Fig. 3.3). This area is included to enable a future comparison of these SOLPS-ITER simulations with a pressure gauge located at the end of a horizontal tube in the sub-divertor, as done e.g. in [187–189]. The pump behind the outer target is simulated by surfaces with a reflection coefficient < 1 . Contrary to the commonly applied approximation of placing these surfaces into the corners of the then completely closed divertor, the inclusion of the sub-divertor area allows also to simulate the pump in its actual poloidal location. The reflection coefficient was set to 0.49 for these pumping surfaces. A deuterium puff into the SOL from the vertical targets, as in the experiment, lead to numerical issues with the code and was hence not possible. Instead the possibility to puff deuterium and neon from the horizontal target (tile 5) into the private flux region was implemented in EIRENE, but not used in favour of core sources in B2.5 (see subsection 3.4.5).

3.4.4 Atomic and Molecular Physics

All charge states of deuterium and neon were included in the simulations (in contrast to the possibility of bundling charge states of atoms with a higher charge number). Tungsten was not included due to its low abundance and the time-expensive calculations that would be connected to it. The atomic and molecular EIRENE reactions included in the simulations in the input.dat file are listed in Tab. 3.1.

3.4.5 Boundary Conditions

The time steps per iteration can be widely spread over several orders of magnitude, depending on how stable and how converged the cases were. A variation of the time step could also be used to test stability and convergence of a case. However, since running the cases at time steps larger than the energy confinement time is not physical and can lead to numerical issues, the cases presented here were set to $\delta t = 1 \times 10^{-4}$ s. The minimum electron temperature was set to $T_{e,\text{min}} = 2$ eV in order to avoid numerical problems in cold cells close to the targets. The puffing of deuterium and neon from the PFR was foregone in favour of fuelling and seeding from the core boundary in order to increase the convergence velocity, since the outward transport acts faster than the penetration of the core by neutrals. The allocated calculation time of the core region is increased by a factor 1000 to assist a faster convergence of simulations fuelled this way

Table 3.1: Atomic and molecular reactions included in EIRENE in the SOLPS-ITER simulations treated in this thesis. All reaction rates are contained in AMJUEL [176] and HYDHEL [177]. Apart from the electron impact ionisation, neon is treated in ADAS [179], ACD96 (ionisation and recombination processes) and PRB96 (charge exchange reactions and line/bremsstrahlung radiation).

Reaction	Description
$D^0 + e^- \rightarrow D^+ + e^- + e^-$	Electron impact ionisation
$D_2^0 + e^- \rightarrow D_2^+ + e^- + e^-$	Electron impact ionisation
$D_2^0 + e^- \rightarrow D^0 + D^+ + e^- + e^-$	Ionising dissociation
$D_2^+ + e^- \rightarrow D^+ + D^+ + e^- + e^-$	Ionising dissociation
$D_2^0 + e^- \rightarrow D^0 + D^0 + e^-$	Electron impact dissociation
$D_2^+ + e^- \rightarrow D^0 + D^+ + e^-$	Electron impact dissociation
$D^+ + D_2^0 \rightarrow D^+ + D_2^0$	Elastic collision
$D^0 + D^+ \rightarrow D^+ + D^0$	Charge exchange
$D^+ + D_2^0 \rightarrow D^0 + D_2^+$	Charge exchange
$D_2^+ + e^- \rightarrow D^0 + D^0$	Recombining dissociation
$D^+ + e^- \rightarrow D^0$	Recombination (radiative and three-body)
$Ne^0 + e^- \rightarrow Ne^+ + e^- + e^-$	Electron impact ionisation (Neon)

The computational grid in Fig. 3.4 corresponds to the physical grid shown in Fig. 3.2. It allows to define boundaries, called by the points of compass direction, of the grid. In the simulations presented here the boundary conditions were set as following for deuterium and neon particles, and energy:

South (Core): For numerical stability and velocity the particle sources have been set to the core boundary, i.e. in the simulation the core functions as particle source even though this is barely the case in the experiment. The deuterium density at the boundary was fixed at values in the range $n_{D^+} = 7 \times 10^{19} - 10 \times 10^{19} \text{ m}^{-3}$. Also for neon the density was fixed at the core boundary, varying in the range $n_{Ne^{10+}} = 0 \times 10^{17} - 10 \times 10^{17} \text{ m}^{-3}$. The heating power, equally distributed over all core boundary cells and between electrons and ions, was fixed at values in the range $P_{\text{heat}} = 20 - 35 \text{ MW}$.

North (SOL), South (Inner/Outer PFR): For all particles these 3 boundaries consist a sink, enforced by a leakage option with the loss being proportional to the density. For the energy a decay length is set.

West/East (Inner/Outer Target): For charged particles and energy, at the targets sheath conditions are simulated, while the targets have no effect on neutral particles.

The introduction of heating power via the core boundary is in accordance with the experiment. As described above, the possibility of puffing fuel and impurity neutrals into the divertor region like in the experiment is implemented in these simulations but currently not used. Instead, fuel and impurity ions are introduced via the core boundary, while in the experiment the fuel ion source from NBI heating in the core is usually small. The introduction of fuel and impurity

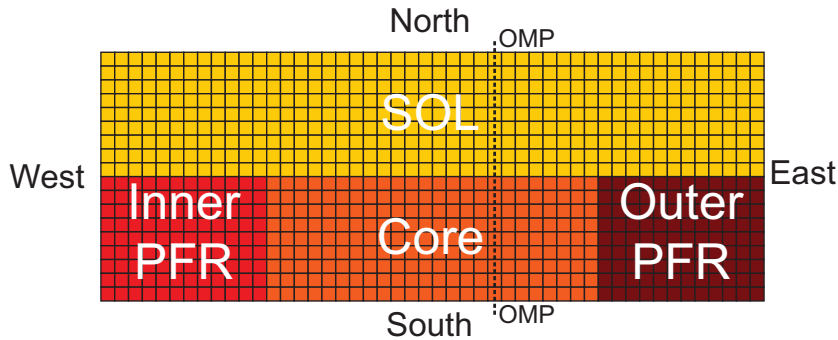


Figure 3.4: B2.5 computational grid (48×18) used in this thesis. In the grid 4 areas can be distinguished (corresponding to same-coloured areas in Fig. 3.2): the core (orange), the SOL (yellow), the inner and the outer PFR (light and dark red) below the X-point. The outer midplane (OMP) position is marked.

ions with a fixed core ion density was chosen in order to provide a faster convergence of the simulation cases due to the faster transport from the core to the edge than by the ionisation of neutrals. However, for impurities their introduction by the core could lead to excessive impurity concentration in the core area. Furthermore, in this setting the potential enrichment of impurity neutrals in the divertor area cannot be properly examined. Additional sources within the simulation domain were not used for now. In the experiment, however, it was found that large fractions of the NBI heating power are not deposited in the region that for the simulations presented here would be the core (see Fig. 5.20), hence tools were prepared to include radial heat and particle source profiles into the simulations in the future. The heating power of the simulations is set at the position of the core boundary of the simulation at $\rho_{\text{pol}} = 0.69$. Radiation from further inside would have to be added to the heating power and the core radiation power in order to receive their actual value. In the simulations, however, this region inside the core boundary is not taken into account and the radiation from there can only be estimated by a comparison with the experiment, which was done in section 6.2.

The radial transport parameters D_{\perp} (particles) and $\chi_{i,e}$ (heat) were fixed as shown in Fig. 3.5. They were chosen in an unseeded reference case ($P_{\text{heat}} = 20 \text{ MW}$, $n_{\text{D}^+} = 1.0 \times 10^{20} \text{ m}^{-3}$) in such a way to result in

- a midplane separatrix density of $n_{e,\text{sep},m} = 3.5 \times 10^{19} \text{ m}^{-3}$. This is well within the range of $n_{e,\text{sep},m,\text{max}} \approx 0.4\text{--}0.5 \cdot n_{\text{GW}} \approx 3.0 \times 10^{19}\text{--}4.5 \times 10^{19} \text{ m}^{-3}$ considered as upper limit of stable H-mode plasmas [190].
- a midplane separatrix temperature of $T_{e,\text{sep},m} = 91 \text{ eV} \approx 100 \text{ eV}$. The value of $T_{e,\text{sep},m} \approx 100 \text{ eV}$ is a commonly used assumption for H-mode discharges in JET. Due to uncertainties in the reconstruction of the magnetic field the separatrix position cannot be determined accurately. The separatrix temperature can be estimated from pedestal temperature profiles nonetheless, based on a two-point model with purely diffusive particle and heat transport [42, ch. 4.10 & 5.7]. Following [191], for some of the discharges treated in chapter 5 the radial pedestal temperature profile was used to determine the exponential temperature decay length $\lambda_{T_e} \approx 16 \text{ mm}$ and the SOL width $\lambda_q \approx 4.5 \text{ mm}$. According to [42, eq. 4.87] the

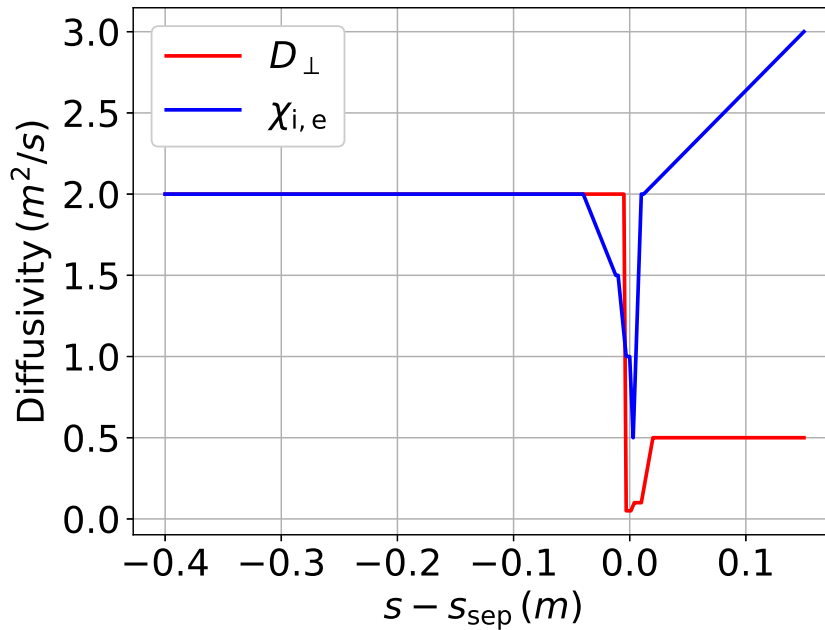


Figure 3.5: Transport parameters as set in `b2.transport.inputfile`. The coordinate $s - s_{\text{sep}}$ denotes the distance to the separatrix at the outer midplane. Close to the separatrix a decrease of the parameters serves to simulate the edge transport barrier which is responsible for the pedestal in H-mode.

separatrix temperature was found to be in the range of $T_{e,\text{sep},m} \approx 90\text{--}130\text{ eV}$, confirming the assumption above.

The transport parameters were not varied through the simulations. This choice was made to focus on the effects the neon seeding has on the profiles rather than the effects of variations in the transport. The possibility that this might render the simulations rather unrealistic in experimental terms, e.g. by midplane separatrix temperatures that are considerably lower than the around 100 eV one would assume in an H-mode experimental discharge, was accepted. Additional radial pinches were not added, drifts were not included in the simulations, and also the impact of ELMs on transport could not be considered.

4 The Joint European Torus (JET)

The Joint European Torus (JET) is a tokamak device hosted by the Culham Centre for Fusion Energy (CCFE) in Culham (United Kingdom) and since its inauguration in 1984 (see e.g. [24, 192, 193] for historic overviews) the world's largest fusion experiment. Since 1994 [193] JET is operated in divertor configuration. During a deuterium-tritium campaign in 1997 a fusion power of 16.1 MW was produced [14], corresponding to $Q = 0.64$ (see Eq. 1.3). In 2011 JET was equipped with an ITER-like wall (JET-ILW) [194, 195], i.e. with tungsten as divertor material and beryllium as the main chamber wall material, in contrast to the previous carbon wall and divertor (JET-C).

JET is managed by the EUROfusion Consortium, allowing scientists from all over Europe and beyond to conduct experiments at JET (see author list and affiliations of [138]). This thesis has been conducted within the framework of the EUROfusion Consortium at JET. The most important diagnostics and heating systems available at JET shall therefore be briefly introduced in the following and their respective role in the context of this thesis is emphasised. However, some diagnostics that could have given additional insight, e.g. divertor target infrared cameras, divertor spectroscopy of neon, Stark broadening spectroscopy, lithium beam diagnostic, were not used and therefore not presented here, mostly due to the unexceptional discharge parameters such as high density, heating power, or neon seeding and the consequent difficulties arising in data acquisition or evaluation. To conclude this chapter, JET results regarding divertor and detachment physics relevant for this thesis are briefly summarised.

4.1 JET Heating Systems

4.1.1 Ohmic Heating

The electric field induced by the central solenoid drives the poloidal current in order to create the poloidal magnetic field component. The positive direction of magnetic field and current in JET is defined such that in lower single null configuration it points clockwise when seen from above [196]. Since the plasma can be assigned a resistivity which is caused by electron-ion collisions the induced poloidal current heats the plasma [18, ch. 5.2][21, ch. 5.6], analogous to an electric current in a wire causing a power loss of I^2R . This heating mechanism is called Ohmic heating. In JET it can contribute roughly 1 MW of heating power [24]. Since the so called Spitzer resistivity is proportional to $T^{-3/2}$ [117, 197], this heating mechanism becomes more ineffective when higher temperatures are reached. Further external heating has to be applied to achieve the high temperatures that are required for ignition.

4.1.2 Ion Cyclotron Resonance Heating (ICRH)

In a plasma a multitude of wave phenomena can be found [17, 170] and electromagnetic waves can be absorbed or reflected at resonance frequencies. The excitation of the Ion Cyclotron Resonance Frequency (ICRF) can thus be used to heat the plasma. The ion cyclotron frequency is the gyration frequency of ions with mass m_i around the magnetic field lines

$$\omega_{ci} = \frac{eB}{m_i}. \quad (4.1)$$

The dependency of this frequency on the local magnetic field strength $B = B_{\text{tor}}(R) \propto \frac{1}{R}$ allows to specify the absorption region of an incident wave by tuning its frequency accordingly. Ion Cyclotron Resonance Heating (ICRH) is often applied to prevent the accumulation of impurities in the core [198]. In the experiments conducted for this thesis, with a similar toroidal magnetic field for all discharges, the ICRH was operated at frequencies of around 42 MHz.

4.1.3 Neutral Beam Injection Heating (NBI)

A plasma can also be heated by injecting energetic particles that transfer their energy to the plasma. Since charged particles are deflected by the magnetic field, only neutral particles can heat the plasma core. To create a beam of energetic neutral particles in the JET plug in neutral injectors (PINIs), hydrogen ions are created by a particle source and then accelerated by an electric potential of 125 kV [199]. Before entering the main plasma, the positive ions are neutralised by charge exchange reactions with a neutral gas target [18, ch. 5.5]. The neutral beam particles can then penetrate the main plasma and deposit their energy by charge exchange and ionisation reactions [18, ch. 5.3]. The poloidal energy deposition will depend on the density distribution and the cross-sections of these reactions which in turn depend on the temperature distribution and the beam energy. Codes like TRANSP [200] or PENCIL [201, 202] are used at JET to calculate the radial power deposition profile. In total, the 16 PINIs at JET, located at two toroidal positions with 8 PINIs each, are capable to generate up to 34 MW of heating power [199]. The injection of neutral particles and their ionisation constitutes not only a heat but also a particle source in the plasma centre.

4.2 Fuelling and Pumping

4.2.1 Gas Introduction Modules (GIMs)

The vacuum vessel of JET is filled with gas by gas introduction modules (GIMs) [203]. Up to 4 different gases per discharge can be injected at 10 poloidal positions. The JET divertor GIMs consist of a toroidally placed ring with points of gas entry in regular distances, ensuring a toroidally symmetric gas puff [204]. The gas injection can be performed either in feed-forward mode, in which the puffing rate is pre-set, or in feedback mode, where the injection rate is

permanently adapted in order to match a set plasma parameter, e.g. to maintain a specific density.

The discharges analysed for this thesis were all done in feed-forward mode. During the discharges deuterium was primarily puffed from the GIMs 10 (between the divertor tiles 7 and 8 on the LFS) and 12 (between tiles 1 and 3 on the HFS) into the SOL from the vertical targets (orange arrows in the enlarged area of Fig. 4.1) and neon was injected into the PFR from GIM 11 in the area of tile 4 (purple arrow). GIM 11 has proven in the past to be the most efficient for neon puffing in the sense that lower fluxes are required than through other GIMs to reach similar radiation levels [205].

4.2.2 Pumping

The JET vessel vacuum (base vacuum pressure: 5×10^{-8} mbar) is mainly created by 4 turbo-drag pumps [206]. For a more efficient impurity control a cryopump is installed close to the divertor. One of the advantages of the divertor configuration is that charged particles are transported into the divertor region where they are neutralised at the targets. Thus, in the divertor region the resulting high neutral densities facilitate pumping of neutral particles. The cryopump of JET can be found close to the outer divertor coil (marked in red in Fig. 4.1b). To shield the cryopump from radiation, wall elements called louvres are installed at the entrance to the sub-divertor area [188] (marked in red in the enlarged area of Fig. 4.1). For further protection it is equipped with a nitrogen-cooled chevron baffle [207]. The cryocondensation is realised with 6 tubes containing supercritical helium. For the pumping of helium an argon spray facility is included to remove the helium by cryosorption. Since the pump's inventory for condensed gasses is limited, it needs regular regeneration phases. After pumping them out, the gases are reprocessed by an active gas handling system [208].

4.3 JET Diagnostics

4.3.1 Foil Bolometers and Tomographic Reconstruction

The radiation power at JET is measured by foil bolometers. They contain a thin gold foil which absorbs incident radiation over a broad wavelength range [209] and converts it to heat. The heat is conducted to a meander structure below the foil that acts as a resistor and allows to determine the heat deposited on the foil by the change of its resistance. Two measuring bolometers and two covered reference bolometers are arranged in a circuit called Wheatstone Bridge (see e.g. depictions in [210] or [211]). An alternating voltage is applied to this circuit and the voltage U_b between two points of the Wheatstone Bridge is measured. From the bolometer equation [210]

$$P_{in} = C \left(\frac{dU_b}{dt} + \frac{U_b}{\tau} \right) \quad (4.2)$$

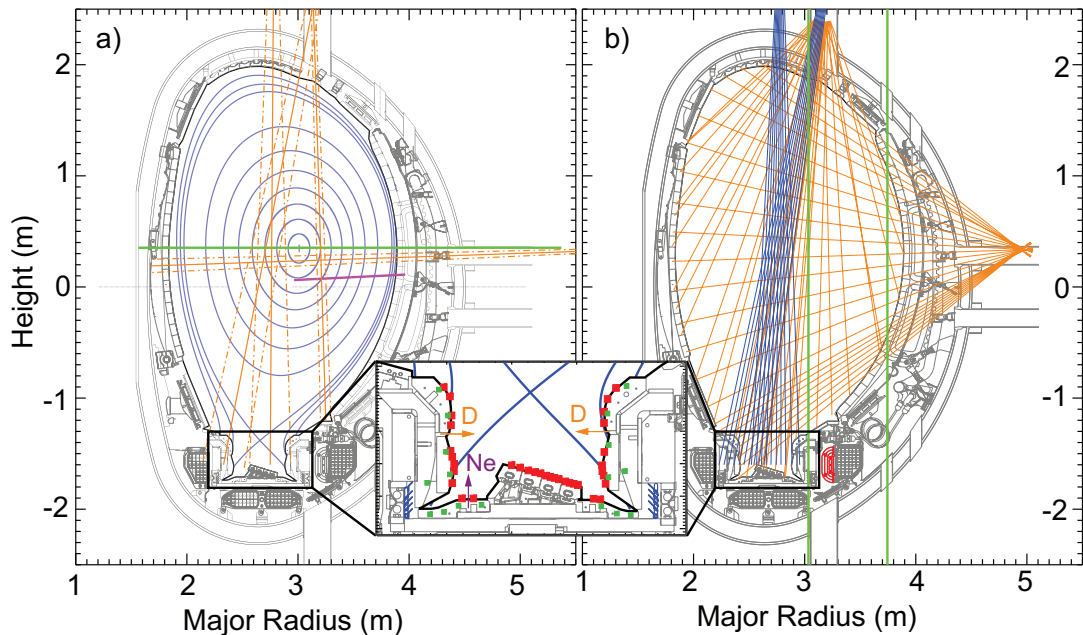


Figure 4.1: a) Typical magnetic flux surfaces (blue), Visible Light Spectrometer lines of sight of the global array (orange), High Resolution Thomson Scattering (magenta), Electron Cyclotron Emission (green). b) Horizontal and vertical bolometer lines of sight (orange), Visible Light Spectrometer lines of sight of the divertor array (blue), channels 3 (core) and 4 (edge) of the infrared interferometer system (green), and divertor cryopump (red). In the enlarged area: Divertor Langmuir probes (red), divertor thermocouples (green), locations of deuterium (orange) and neon puffs (purple), and louvres (blue).

the incident radiation power can be derived. The time constant τ and the material dependent constant C are determined prior to each discharge. In contrast to diode bolometers, foil bolometers can be absolutely calibrated and hence allow the measurement of the radiation power [211]. In JET the bolometer system consists of a vertical and a horizontal camera, each with 24 lines of sight (LOS) [212] (orange lines in Fig. 4.1b). 8 LOS of each camera allow a higher resolved view of the divertor region [213].

To receive a two-dimensional poloidal radiation power density profile, it is necessary to perform a tomographic reconstruction on all the lines of sight measurement data. There are various methods to implement such a tomographic reconstruction [214]. At JET the “anisotropic diffusion model tomography” [213, 215–217] is utilised in order to reconstruct radiation emission profiles. A comparison between numerical simulations and tomographic reconstruction in JET-ILW indicates that the radiation power might be overestimated by the tomographic reconstruction [161]. Since the tomographic reconstruction requires the manual adaption of reconstruction parameters in order to find physically meaningful solutions and can thus be quite time-consuming, this method is not suited to determine a full time-trace of the total radiated power over whole discharges, even though recently there are efforts to accelerate this by the use of neural networks [218]. For this purpose, a faster, but not necessarily as accurate, algorithm is implemented that is based on weighted summation of the vertical camera’s bolometer channels [219].

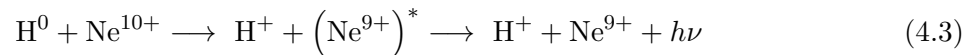
4.3.2 Visible Light Spectroscopy (VLS)

A passive optical spectroscopy system is installed at JET [220]. It not only allows wavelength-resolved measurements in the visible range (400 nm–700 nm) but also the measurement of single wavelengths at higher time resolutions [221]. The Visible Light Spectroscopy (VLS) can be subdivided in two major arrays:

- The global array (orange lines in Fig. 4.1a) provides 4 LOS viewing through the plasma core. Since two of these LOS do not include the divertor region their bremsstrahlung signal (523 nm) together with the High Resolution Thomson Scattering (HRTS) profiles of electron density n_e and electron temperature T_e can be used to derive the line-averaged effective charge state Z_{eff} (similar as in [222]).
- The divertor array consists of 10 LOS for each the inner and the outer divertor area (blue lines in Fig. 4.1). They are capable to measure the D_α (656 nm), Be II (527 nm) and W I (401 nm) lines which allows to use these lines to identify ELMs and transitions between H-mode and L-Mode confinement due to the transport of the ionic species towards the divertor and their recycling behaviour.

4.3.3 Charge Exchange Recombination Spectroscopy (CXRS)

Usually there are more diagnostics available to determine the electron temperature T_e . One of the few diagnostics to measure the ion temperature T_i is the Charge Exchange Recombination Spectroscopy (CXRS) [223]. When a neutral atom is injected into the plasma, e.g. a hydrogenic ion to heat the plasma, it can undergo a charge exchange reaction with a plasma ion, e.g. in our case an impurity neon ion:



At the back-transition from its excited state to a lower state the plasma ion emits line radiation. The line is broadened by the ions thermal motion and hence the broadening can be used to determine the ion temperature. Since the evaluation of CXRS data is quite time-consuming, its utilisation in the framework of this thesis was limited (and hence is not depicted). For JET Pulse Number (JPN) 92118 (neon seeding rate $\Gamma_{\text{Ne}} = 1.2 \times 10^{22} \text{ es}^{-1}$; heating power $P_{\text{heat}} = 23 \text{ MW}$) core and pedestal ion temperatures were determined by CXRS [224], showing equality with the electron temperatures over the entire radial profile, be it for a seeded or an unseeded time point. Compared to most of the neon-seeded discharges examined for this thesis, the neon seeding rate in JPN 92118 was equal or higher than in these discharges. Additionally, all these discharges have similarly high densities. These observations allow to assume $T_i = T_e$ in the following without being dependent on dedicated T_i measurements.

4.3.4 High Resolution Thomson Scattering (HRTS)

At non-relativistic speeds a charged particle can elastically scatter an electromagnetic wave. This principle can be used for diagnostic purposes [103]. The incident electromagnetic wave at JET is a Nd:YAG laser beam with a pulse rate of 20 Hz [225]. The light scattered at the electrons is measured by an optical system along a line including 63 points in the range $R = 2.9\text{--}3.9\text{ m}$ [226] (magenta line in Fig. 4.1a). The broadening of the scattered wave frequency allows the measurement of the electron temperature T_e and the intensity the measurement of the electron density n_e . Uncertainties in the magnetic field reconstruction, especially of the separatrix position, prevent a precise assignment of a poloidal coordinate to the measurement points. Therefore it is common practice to radially shift the profiles of the Thomson scattering diagnostic until the separatrix electron temperature in H-mode is around 100 eV. For few discharges presented in this work the separatrix electron temperature was estimated from the two-point model (see subsection 3.4.5). The estimate showed that the separatrix electron temperature of the examined discharges was in the range of 90–130 eV in H-mode and that this temperature can hence be used for shifting the HRTS profiles.

4.3.5 Electron Cyclotron Emission (ECE)

The gyrating motion of the electrons around the magnetic field lines leads to the emission of cyclotron radiation at the n -th harmonic of the resonance frequencies

$$n \cdot \omega_{ce} = n \cdot \frac{eB}{m_e} \quad (4.4)$$

The dependence of the magnetic field to the major radius ($B = B_{\text{tor}}(R) \propto \frac{1}{R}$) allows to locate the origin of the cyclotron radiation in terms of the major radius R along the measurement LOS (green line in Fig. 4.1a). The magnetic flux surfaces can act as the surfaces of a black body and hence the intensity of the emitted radiation is proportional to the electron temperature T_e of this surface [227]. The Electron Cyclotron Emission (ECE) radiometer at JET provides 96 channels in the low-field halve of the plasma cross-section [228]. The time resolution of 0.5 ms particularly allows the detection of fast events.

4.3.6 Far-Infrared Interferometer (FIR)

The principle of a Mach-Zehnder interferometer can be used to determine the line-integrated density of a plasma [229]. At JET far-infrared laser beams are sent through the plasma along 8 paths [230] (two of the horizontal channels through the edge and the core are shown in green in Fig. 4.1b). The horizontal edge channel of this diagnostic can be used to detect the characteristic increase of the pedestal density due to the pedestal formation when the plasma is transiting from L-mode to H-mode.

4.3.7 Divertor Langmuir Probes

One of the first diagnostics ever used to measure the properties of the plasma is the Langmuir probe, named after plasma physics pioneer Irving Langmuir. Due to high temperatures and power fluxes in most parts of the plasma [18, ch. 10.10], Langmuir probes are only to be used close to the wall. A metal wire is introduced into the plasma and an external voltage is applied to it. The current-voltage characteristic is determined by the sheath (see subsection 2.2.1) in front of the probe.

For applied voltages U which lie below the plasma potential V_p the I - U characteristic (current on the probe in relation to applied voltage) is described by [18, ch. 9.2 & 10.10][17, ch. 9.3]

$$I = j_{\text{sat},i} A \left(1 - \exp\left(\frac{e(U - V_p)}{T_e}\right) \right) \quad (4.5)$$

Here $j_{\text{sat},i}$ denotes the ion saturation current density and A the usually unknown probe surface. For low voltages the current approaches the ion saturation current $j_{\text{sat},i} = n_s e c_s$ (with n_s the plasma density at the sheath entrance and $c_s = \sqrt{\frac{T_e}{m_i}}$ the ion sound speed), i.e. only ions reach the probe surface and most electrons are repelled. With increasing probe potential more electrons are able to reach the probe. Eq. 4.5 assumes a Boltzmann distribution for the electron energies in order to receive the electron currents on the probe. The floating potential V_f marks the probe potential for which the electron current and the ion current are equal and which the probe would have if no external voltage was applied. At $U = V_p$ Eq. 4.5 loses its validity because for voltages larger than the plasma potential all electrons are already attracted to the probe. The probe current in this case is similar to the electron saturation current $j_{\text{sat},e}$, which actually saturates only in the ideal case of a planar probe while in actual measurements the surface shape of the probe leads to an expansion of the sheath with increasing potential and hence to a further increase of the current, although with a visible kink of the I - U characteristic at the plasma potential.

In a logarithmic representation the electron temperature can be determined from the slope of the I - U characteristic while the ion saturation current measured for low voltages can be used to measure the density. In the experiment this characteristic can be received by a voltage scan (in JET H-mode the voltage is swept with a frequency around 500 Hz [231]), thus retrieving also electron temperature, electron density and ion saturation current and hence allowing the calculation of the pressure $p_e = n_e T_e$ and according to Eq. 2.8 the power density to the divertor targets $q_{\text{div}} = \frac{\gamma}{e} \cdot j_{\text{sat},e} \cdot T_e$.

For low temperatures the slope of Eq. 4.5 becomes very steep. This sets a sensitivity limit for Langmuir probes in the experiment since the voltage might not be swept in small enough steps to depict this increase. Furthermore, the current is limited by the internal resistance of the probe and its electric circuit cables, therefore restricting a precise measurement of the current. At JET this sensitivity limit is at around 5 eV. In fact, by comparing the temperatures measured by the Langmuir probes in JET-ILW with numerical simulations it was shown that at lowest temperatures the measured values are not reliable, but can only be used to show trends [161].

The divertor Langmuir at JET probes were originally designed as triple probes. At most of the 35 poloidal divertor positions (red squares in the enlarged area of Fig. 4.1) 3 probes are installed, allowing the measurement at 3 different, fix voltages and the derivation of the plasma parameters from these measurements [232, 233]. Avoiding a voltage scan, this technique would allow a higher time resolution. Due to the unavailability of at least one probe per position all probes were operated as swept single probes.

4.3.8 Divertor Thermocouples

A thermocouple is a temperature sensor based on the Seebeck effect. On the rear of some of the divertor target tiles such thermocouples are installed (green squares in the enlarged area of Fig. 4.1) to measure the temperature of these tiles. The tiles are heated by the power fluxes onto them during plasma discharges. For this thesis the temperature measurements will be used to get a rough estimate of the power fluxes onto the target tiles: increasing temperatures indicate power fluxes to the target and hence a rather attached state while decreasing temperatures are an indicator for comparably lower power fluxes and some degree of detachment. Since the tiles are not thermally connected to their surroundings, their only way to cool is by radiation [234]. Their cooling time is much longer than the duration of a plasma discharge and therefore the analysis of the temperature decay after a discharge can be used for a calorimetric analysis of the energy that was deposited on the tiles during the discharge [144, 234].

4.4 Divertor Physics in JET

The experiments presented in this work are designed on the basis of previous findings regarding the divertor and detachment physics in JET. Some of these findings are presented in this section using examples from JET, even though some results might be observed in other machines as well.

4.4.1 In-Out Asymmetry

As in many experiments an in-out divertor asymmetry can be observed at JET: the power load to the outer divertor leg is increased with respect to the inner one; similarly the temperature at the inner target is lower and the density and the radiation power higher. This leads to a detachment of the inner divertor at lower density or at lower impurity concentration as for the outer divertor. Ideally, both targets have to be detached in order to protect the whole divertor from high heat and particle fluxes. Experiments with reversed magnetic field and numerical simulations showed that drifts play a major role in this divertor asymmetry [124, 235–237]. Reversing the direction of the toroidal magnetic field can reduce this asymmetry but leads to other disadvantages, e.g. regarding the L-H threshold [122, ch. 4.5].

4.4.2 Divertor Wall Material

In JET the most noticeable change in terms of wall material was the replacement of the carbon divertor with a tungsten divertor in 2011. The two divertors are commonly denoted JET-C (JET with carbon divertor) and JET-ILW (JET with ITER-like wall, referring to the combination of wall materials foreseen for ITER: beryllium in the main chamber and tungsten in the divertor). General overviews over the changes between JET-C and JET-ILW can be found in [142, 194, 195, 238] and references therein.

Despite its higher sputtering yield and concentration in the plasma (some percent [239]), carbon has a minor impact on the main plasma as it radiates primarily in the divertor, the SOL, and the edge and is fully ionised in the core. Tungsten instead will never be fully ionised in the core, requiring to avoid an accumulation of tungsten in the core, which can occur naturally for peaked density profiles and due to inward pinches. This can be achieved by decreasing the tungsten sources at the targets and by increasing the outward transport [240, 241]. The tungsten source terms can be reduced increasing the fuelling above $1 \times 10^{22} \text{ es}^{-1}$ [240, 242], or seeding of impurities [240, 243] to decrease the target temperatures. The largest tungsten source stems from periods during ELMs and the source depends strongly on the divertor conditions [244]. An increase of fuelling also causes an increased ELM frequency at decreased amplitudes, which for ELM frequencies above 30–50 Hz leads to a stronger flushing out of impurities from the confined plasma [240, 242]. In such cases with sufficient fuelling the tungsten sources do not play the major role for a tungsten accumulation in the core, but transport does. One common way to increase the outward transport of tungsten is the use of ICRH [198, 245].

Due to the lower impurity concentration in JET-ILW with respect to JET-C, Z_{eff} and the intrinsic radiation power, also in the core plasma, decreased, resulting in an about 30 % lower threshold power for the L-H transition compared to JET-C [195, 246]. The often used Martin scaling [70] for the L-H power threshold contains only few metal machines and thus its predictive capabilities for ITER or JET-ILW are questionable [142].

The limited operational space, e.g. by the need for increased fuelling to prevent tungsten sputtering, leads to a lower energy confinement in JET-ILW ELMy H-mode discharges compared to JET-C [247–249]. A higher fuelling was already shown in JET-C to reduce confinement [247]. In particular, a decrease of the pedestal pressure was observed in JET-ILW, caused by a decreased pedestal temperature [248]. Due to the stiffness of core profiles, this also leads to a reduced core temperature and a decreased energy confinement [240]. In some cases, especially with high triangularity, the confinement could be partly recovered by nitrogen seeding [240, 250]. A numerical analysis of such nitrogen-seeded high triangularity discharges can be found in [251]. It was also found that in the proximity of the L-H threshold ($1 < P_{\text{SOL}}/P_{\text{LH}} < 2$) the confinement factor $H_{98(y,2)}$ was lower than in comparable JET-C discharges [248].

4.4.3 Divertor Geometry and Magnetic Field Geometry

Not only the material of the divertor walls can impact the plasma but also the divertor geometry and the shape of the magnetic field lines intersecting the targets. In JET-ILW the positions of

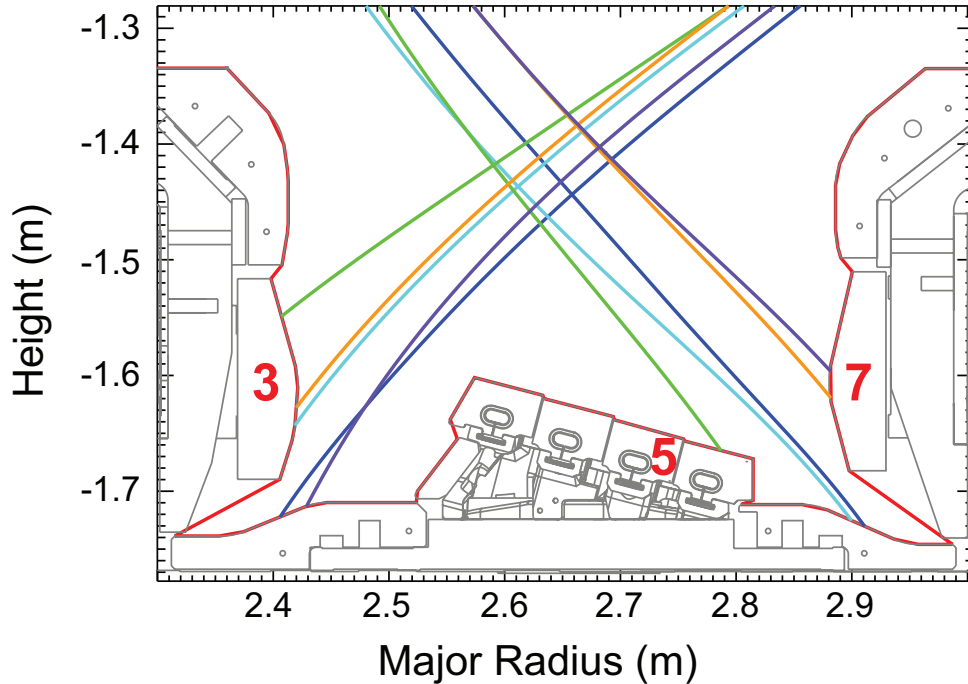


Figure 4.2: Examples of the most common divertor geometries at JET-ILW: V/H (green), V/V (orange), C/C (blue), C/V (purple), V/C (cyan). The numbers of inner vertical (3), horizontal (5) and outer vertical (7) target tiles are displayed.

the divertor strike points can be widely varied: the inner as well as the outer strike point can be placed on the respective vertical target, horizontal target, or the corner. Figure 4.2 depicts some of the most common configurations: the horizontal target (V/H or HT) configuration with the inner strike point on the vertical tile 3 and the outer strike point on the horizontal tile 5; the vertical target configuration (V/V or VT) with the inner strike point on tile 3 and the outer strike point on the vertical tile 7; the corner-corner configuration (C/C) with both strike points in the corners of the divertor, close to the pumping ducts; furthermore C/V and V/C.

Plasma particles that are recycled at a surface are on average re-emitted perpendicularly to that surface [196]. The shape and orientation of the divertor target hence determines where neutrals are reflected and re-ionised. While a horizontal target reflects the neutrals into the outer SOL, a vertical target reflects them towards the inner SOL and therefore close to the separatrix and to high power fluxes [196, 252]. Reaching low target temperatures, necessary for recombination to set in, requires ion-neutral interactions, ionisation, and radiation. A high neutral density close to the separatrix is therefore highly advantageous for vertical divertor targets to detach at lower densities than horizontal targets. High neutral divertor densities not only facilitate the onset of detachment [122, ch. 4.6] but can also improve pumping. The closure of a divertor, i.e. its capability to prevent neutrals from escaping it, is therefore important and can also lead to an improved core confinement. Two-dimensional simulation codes, such as SOLPS-ITER or EDGE2D-EIRENE, can be used to develop suitable divertor designs.

The degree of detachment of the vertical target can depend on the vertical strike point position on the target [124], with better detachment on the lower part of the target, close to the corner. Furthermore, the spreading of magnetic field lines can be used in order to widen the plasma wetted area on the target and to make it more difficult for neutrals to escape the divertor [122, ch. 4.6]. In the V/V configuration [195] and in the C/C configuration [249, ch. 4.3] the neutral pressure in the subdivertor area has shown to be significantly higher than in the H/H or the V/H configuration, respectively. In a comparison between V/H, V/C, and C/V it was shown [253] that the corner-configuration V/C has a higher $H_{98(y,2)}$ than the vertical configuration C/V and the horizontal configuration V/H. For the vertical configuration C/V the sub-divertor neutral pressure was found to be highest, facilitating the pumping, but possibly also negatively impacting the core area and the confinement. In another study with low triangularity discharges in JET-ILW, no significant difference in energy confinement between a V/H and a V/V divertor was seen [254].

The divertor geometry turned out to play a major role for the L-H transition, first seen by varying the strike point positions, and thus the triangularity, in different V/H configurations [246]. In V/V configuration P_{LH} was a factor of 2 above its value in V/H configuration [255] for high densities. The minimum P_{LH} in V/V configuration was observed at lower densities [256] and a link to divertor oscillations and the asymmetric detachment of the inner divertor was examined [257]. The differences between a horizontal V/H and a vertical V/V target configuration in high triangularity discharges were reproduced and examined in EDGE2D simulations [163]. As observed in the experiment, in the vertical target configuration the outer target detaches at lower densities or lower SOL radiation than at the horizontal target configuration. No major difference was seen between the two configurations in terms of the peak heat flux onto the outer target or impurity content. For the vertical target a higher sub-divertor pressure was observed, together with a reduced ionisation source inside the separatrix, as it was expected for a more closed divertor configuration. With nitrogen seeding, in vertical configuration a reduction and in horizontal configuration an increase of the pedestal density was found, as observed in the experiment.

4.4.4 Impact of Radiation

It has been observed over many years in JET-C that an increase of the radiative power fraction by impurity seeding can lead to a transition from type I to type III ELMs, i.e. to an increase of the ELM frequency and a decrease of their amplitude [151, 205, 258]. The impurity radiation lead to a pedestal degradation, a confinement reduction, and (at least partial) detachment. In similar discharges in JET-ILW the transition from type III to type I ELM regime could be reached at lower pedestal temperatures, though at reduced confinement. Nitrogen seeding could be used to recover the degradation of pedestal and confinement, but also lead to a decrease of the type I ELM frequency [36, 247]. The seeding caused an increase in pedestal pressure, in horizontal (V/H) target configuration caused by an increase in both, temperature and density, while in vertical (V/V) target configuration only the temperature increased [250]. With increased fuelling a general decrease of confinement was observed [248].

4.5 Relevance for This Thesis

The JET experiments treated in this thesis were performed at highest heating powers, i.e. the heating systems introduced above were all used to nearly their full capacity. The variety of diagnostics allowed a detailed observation of these experiments, even though some diagnostics struggled with the high densities and with the neon radiation and were thus not used. The ITER-like metallic wall of JET allowed experiments that are relevant for future reactors, especially with regard to the transport of tungsten into the core in highly neon-seeded discharges. The magnetic field in the divertor was chosen to be in V/V configuration to facilitate detachment and despite the lower confinement compared to the C/C configuration. The confinement was also lowered by the high fuelling, as observed in previous experiments. The low triangularity was chosen to support numerical modelling of the experiments. In the simulations the in-out-asymmetry described above was observed as well, while in the relevant periods of the experiment both targets were detached.

5 Experimental Analysis

In the framework of the JET campaigns M13-17 and M15-20 dedicated high radiation discharges with neon as radiating impurity have been performed in order to examine the impact of neon on the poloidal radiation distribution, the pedestal, the confinement, and the divertor [37, 38, 259] (see Appendix A for list of all JET pulses used here). The results obtained in the analysis of these neon-seeded discharges are presented in this chapter. In section 5.2 an introduction to the evaluated discharges and their basic set-up will be given, followed by the characterisation of three typical discharges at high neon seeding rates and three different heating powers. The investigation into increased energy confinement is presented in section 5.3, the one of the core plasma's impurity content in section 5.4. Details on the poloidal radiation distribution will be given in section 5.5, with a focus on the relation between core and edge radiation as well as a correlation of the X-point radiator with the pedestal density degradation and detachment of the targets in neon-seeded discharges with H-mode and M-mode phases.

The content of this chapter was previously published in [38, 259].

5.1 Experimental Setup

The operational space of the neon-seeded experiments can be characterised by the variation of the following main parameters (see Fig. 5.1):

- Deuterium puff into the divertor SOL: $\Gamma_D = 0.2 \times 10^{23} - 1.0 \times 10^{23} \text{ es}^{-1}$
- Neon puff into the private flux region: $\Gamma_{Ne} = 0.4 \times 10^{22} - 2.2 \times 10^{22} \text{ es}^{-1}$
- Heating power: $P_{\text{heat}} = 14 - 29 \text{ MW}$; for $P_{\text{heat}} < 20 \text{ MW}$ with only ohmic and NBI heating, for $P_{\text{heat}} > 20 \text{ MW}$ with additional ICRH.

The plasma current of $I_P = -2.5 \text{ MA}$, the toroidal magnetic field strength $B_T = -2.65 \text{ T}$ as well as the flux surfaces were kept constant through all discharges examined here. The flux surfaces (see Fig. 4.1a) were in vertical target (V/V or VT) configuration, with the strike lines lying on the vertical tiles 3 (inner) and 7 (outer). The vertical target configuration was selected due to its higher relevance for future tokamaks (see subsection 4.4.3) despite it having a lower confinement than the corner (C/C) configuration under conditions similar to the discharges presented here [253]. Modelling activities were supported by a low triangularity configuration and its broader SOL. The Greenwald density in all the discharges was around $n_G = 0.9 \times 10^{20} \text{ m}^{-3}$. The diagnostics used in order to characterise the discharges in this chapter were introduced in chapter 4.

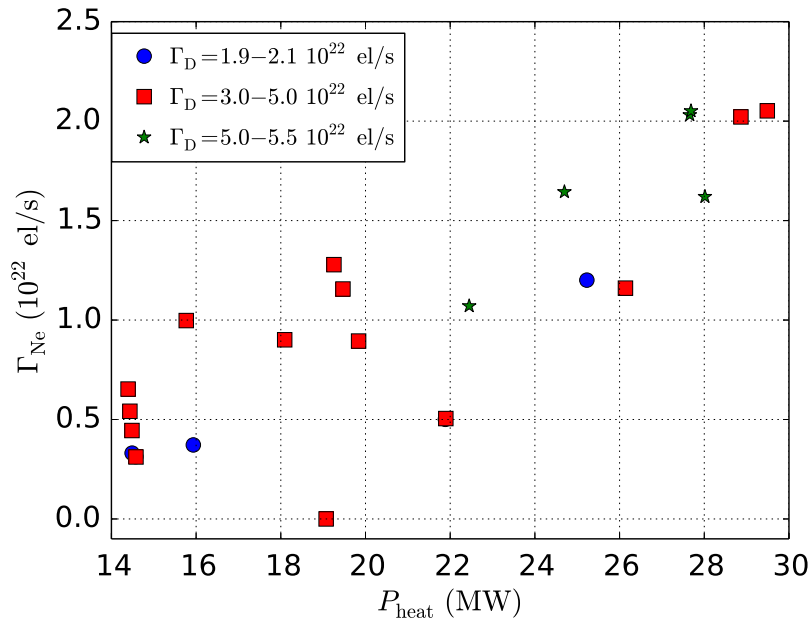


Figure 5.1: Operational space of the examined neon-seeded JET-ILW discharges, described by total heating power P_{heat} and neon puff rate Γ_{Ne} . The different symbols and colours indicate the 3 stages of the deuterium puff rate Γ_{D} . Published in [259].

5.2 Characterisation of Neon-Seeded JET Discharges

This section presents results of 3 experiments which are characteristic for their respective heating power at comparably high neon seeding rates: low power heating at 15 MW in subsection 5.2.1, medium power at 19 MW in subsection 5.2.2, and high power at 29 MW in subsection 5.2.3. The conditions for a transition to a regime without large type I ELMs are discussed in subsection 5.2.4.

5.2.1 Low Heating Power (15 MW)

In the least heated discharge, JPN 87196, the heating power was 15 MW (see Fig. 5.2a). The plasma is in an ELMy H-mode phase when the neon puff begins to affect the plasma (from around $t = 10.0$ s on, see Fig. 5.2d). After $t = 11.0$ s ELMs are not observed anymore (see Fig. 5.2c). From the radial T_e and n_e profiles (see Fig. 5.3) a transition from H-mode to L-mode can hardly be derived, also in the line-integrated density (see Fig. 5.2e) no major change could be observed. The presence of type III ELMs before $t = 11.0$ s and the absence of ELMs afterwards indicate, though, that the plasma underwent a transition from a highly degraded H-mode to L-mode at $t = 11.0$ s. The energy confinement time (see Fig. 5.2b) does not decrease during this transition. The same applies for the confinement factor $H_{98(y,2)} = \tau_E / \tau_{98(y,2)}$ (with the energy confinement time $\tau_{98(y,2)}$ according to the IPB98(y,2) scaling [46]) which remains at a constant value of $H_{98(y,2)} \approx 0.60$. It was observed, not only in this discharge but in all discharges presented in the following, that τ_E and $H_{98(y,2)}$ were barely changed with the onset of neon puffing. It has to be taken into consideration that their values are comparably low already

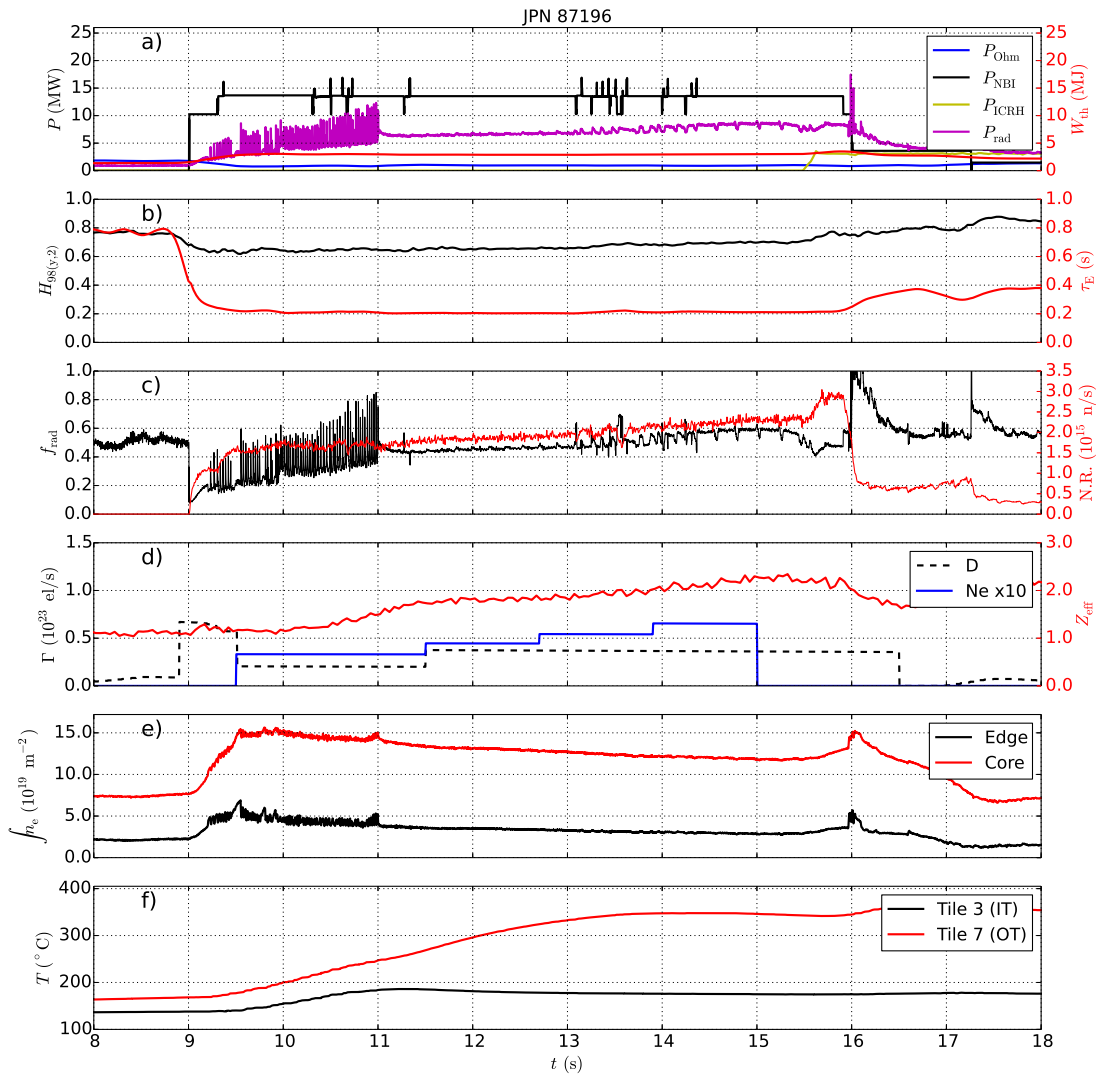


Figure 5.2: Timetraces of JPN 87196, a low power discharge ($P_{\text{heat}} = 15$ MW) with three neon seeding steps. From top: a) heating and radiation powers, energy content W_{th} ; b) energy confinement time τ_E and $H_{98(y,2)}$; c) f_{rad} and neutron rate; d) deuterium and neon puff strengths, Z_{eff} ; e) the line-integrated density from an edge and a core IR interferometry channel (see Fig. 4.1); f) temperatures of thermocouples close to the strike points in the vertical tiles 3 and 7. The neon puff, starting at $t = 9.5$ s, begins to affect the plasma at around $t = 10.0$ s, indicated by the increasing Z_{eff} . Published in [38].

at the beginning of the discharge when no neon was seeded. This can be attributed to the high deuterium puffing rates that were applied to increase the neutral pressure in the divertor. High D_2 puffs have been shown to decrease the pedestal temperature [249] and $H_{98(y,2)}$ [248, 260].

The region of major radiation power density is located at the high-field side (HFS) before the neon puff and after it takes effect until $t = 14.2$ s. The radiation power density is more than double with neon seeding and additionally the radiation inside the confined region close to the X-point is increased as well (see Fig. 5.4). From $t = 14.2$ s until after the end of the neon puff, the highest radiation power density can be measured around the X-point, also inside the separatrix, as observed in previous experiments (see subsection 2.5.2). On the first neon seeding step (see Fig. 5.2d) the radiative power fraction $f_{\text{rad}} \approx 0.50$ (see Fig. 5.2c) is lower than values

that have been achieved in other experiments (up to 0.75 in nitrogen-seeded discharges, up to 0.66 with neon). Only on the fourth neon seeding step, a radiative power fraction of around 0.65 is reached.

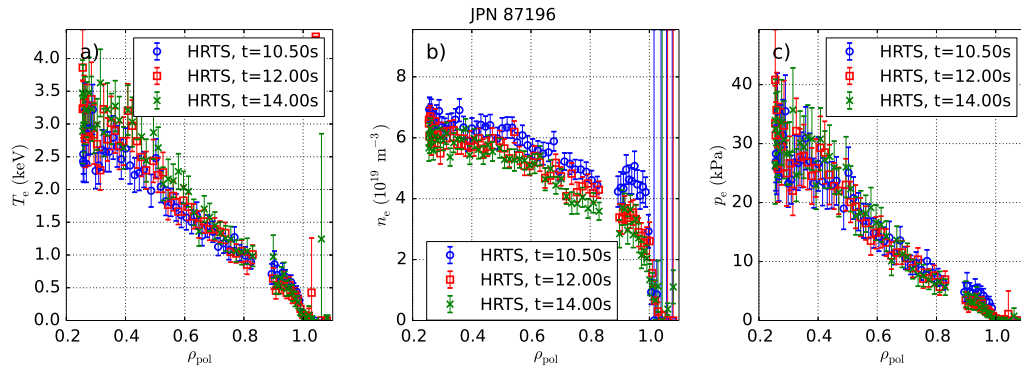


Figure 5.3: Median radial a) electron temperature, b) electron density, and c) electron pressure profiles in the unseeded phase (blue), on the second step (red) and on the fourth step of neon seeding (green) of JPN 87196 ($P_{\text{heat}} = 15 \text{ MW}$). A minor increase of the core T_e and a slight degradation of the pedestal n_e can be observed the more neon is seeded. As the profiles for the unseeded and the seeded time points are very similar, there is no indication that the neon puff might have caused a transition from H-mode to L-mode. Published in [38].

From the divertor thermocouples located in the inner target tiles an increase of about 50°C up to $t = 11 \text{ s}$ is measured (see Fig. 5.2f), followed by a slight temperature drop. At the outer target tiles a significant increase in temperature of up to 290°C until $t = 14 \text{ s}$ could be measured. This is in the same order of magnitude as the unseeded reference discharge JPN 84884 ($P_{\text{heat}} = 19 \text{ MW}$) where an increase of about 270°C could be measured. The temperature increase in both discharges is stopped only by the end of the discharge. These data give a hint that the power flux to the inner target is reduced while the power flux to the outer target is not. The Langmuir probes at the targets (see Fig. 5.5) show that the saturation current and the pressure are reduced at the inner target after the impurity puff at $t = 12.0 \text{ s}$, but instead the peak electron temperature at the outer target increases from about 20 to 35 eV. This means that still a rather large amount of power is deposited on the outer divertor target and, thus, that the outer target is still attached during the L-mode phase with neon seeding. A statement on pressure loss between the midplane and the target can not be made.

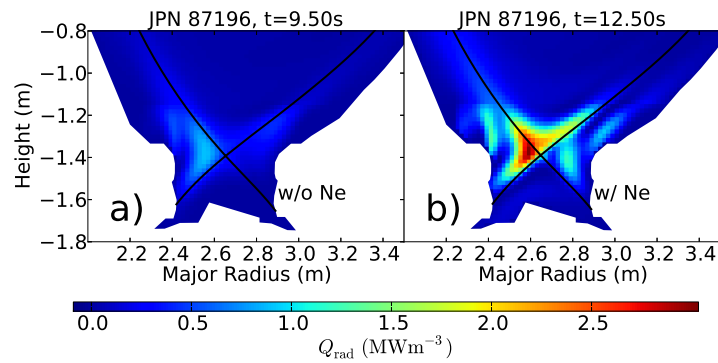


Figure 5.4: Tomographic reconstructions of bolometer data of a) an unseeded and b) a neon-seeded phase of JPN 87196 ($P_{\text{heat}} = 15$ MW). The neon puffing causes the radiation power density at the high-field side to increase but the poloidal distribution remains similar. Published in [38].

5.2.2 Medium Heating Power (19 MW)

The medium power discharge, JPN 85443, has a heating power of 19 MW (see Fig. 5.6a). Until after the beginning of the neon puff at $t = 10.5$ s (see Fig. 5.6d), the discharge is found to be in ELMy H-mode with a transition from type I to type III ELMs at $t = 11.0$ s. At $t = 11.4$ s, the discharge undergoes a transition back to L-mode and reaches again H-mode at $t = 11.6$ s, which can be seen in the D_α signal (see Fig. 5.7a; in Fig. 5.6b the related drop in $H_{98(y,2)}$ is barely visible due to the low time resolution of this signal). The divertor D_α signal is often used to detect the changes in energy and particle fluxes into the divertor related to a transition between H-mode and L-mode (and vice versa) [261, 262]. In this second phase, no ELMs can be detected and instead a regular oscillation at 1 kHz–2 kHz can be seen in the D_α signal. In a spectrogram (see Fig. 5.7b) of a poloidal Mirnov coil above the inner divertor periodic oscillations at 1–2 kHz can be observed which is a characteristic indicator for an M-mode at JET [78].

The M-mode is a regime observed at JET which is intermediate between H-mode and L-mode (see subsection 2.1.3). In Fig. 5.7a the transition from a type III ELMy H-mode (until $t = 11.4$ s) to L-mode and to M-mode (at $t = 11.6$ s) can be seen in the D_α signal: a rapid increase of the D_α signal determines the transition to an L-mode while a drop suggest a transition to H-mode or M-mode. In the following, the M-mode phases are interrupted by transient back-transitions to L-mode. The following scheme for the M-L-M transitions is proposed [140]: It is assumed that with the characteristically increasing density in M-mode compared to L-mode the radiation is increased and hence the power transported over the separatrix, P_{SOL} , is decreased until it is below the L-H threshold power, P_{LH} . An increased outward transport of neon during the L-mode phase, causing a reduction of radiation and an increase of P_{SOL} (or of $Q_{i,\text{edge}}$, according to [263]) above the L-H threshold again, might be a possible explanation for the back-transition to H-mode. A similar transport cycle was reported with krypton seeding at JET in order to describe dithering between H-mode and L-mode [140]. In the experiments presented here it was observed that the back-transitions to H-mode are triggered by sawtooth crashes.

From the poloidal reconstruction of the bolometer signals it can be seen that after the beginning of the neon seeding in JPN 85443 the region of the strongest radiation power density is shifted

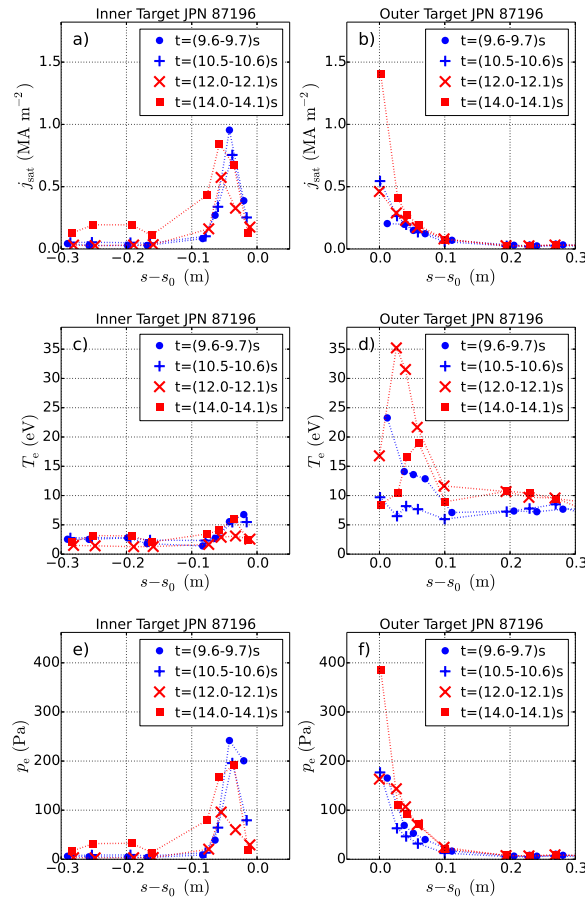


Figure 5.5: Time-averaged (median) target profiles for ion saturation current j_{sat} (top), target electron temperature T_e (middle) and electron pressure p_e (bottom) at the inner (left) and outer (right) target of pulse 87196 ($P_{\text{heat}} = 15$ MW). The coordinate $s - s_0$ marks the LP positions along the target with respect to the strike point. The inner target first detaches with more neon-seeded (blue points: H-mode; red points: L-mode), but on the fourth neon step p_e and j_{sat} increase again to the initial values. The outer target is attached through the whole discharge, even though on the fourth neon seeding step the temperature is decreasing. Published in [38].

from the HFS to the X-point, inside the confined region (see Fig. 5.8). This phenomenon has been observed in previous experiments with nitrogen and neon seeding on ASDEX Upgrade and JET [37, 140, 264].

The energy confinement time remains constant with neon seeding (see Fig. 5.6b). In contrast to the discharge with 15 MW heating power, where the radial density and temperature profiles and hence the energy confinement time were barely altered with neon seeded (see Fig. 5.3), clear changes can be observed in the radial profiles of JPN 85443 at a heating power of 19 MW: the electron density pedestal is strongly degraded (from $n_e = 6 \times 10^{19} \text{ m}^{-3}$ to $2.5 \times 10^{19} \text{ m}^{-3}$ at the pedestal top position $\rho_{\text{pol}} \approx 0.95$) after the onset of the neon puff but due to a steeper gradient the core density remains constant (see Fig. 5.9). T_e , however, increases in the core. The thermocouples in the inner target observe an increase of about 50°C (see Fig. 5.6f), at the outer target of around 100°C until $t = 11.5$ s when at both targets the temperatures start to decrease again when the neon takes effect. The targets are detached during M-mode phases

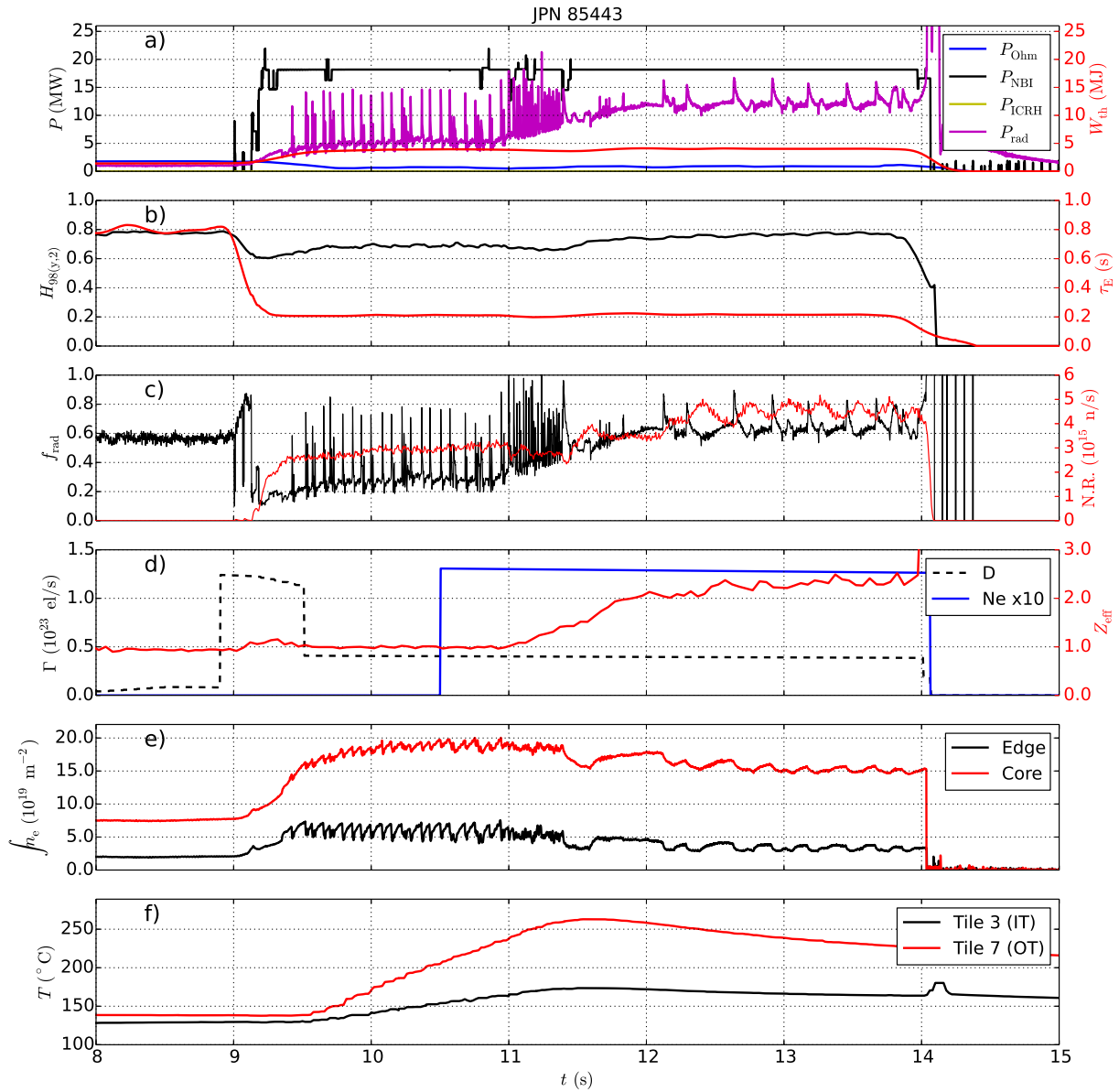


Figure 5.6: Timetraces of JPN 85443, a medium power discharge ($P_{\text{heat}} = 19 \text{ MW}$) with strong neon seeding. Quantities as described in Fig. 5.2. The neon puff (starting at $t = 10.5 \text{ s}$) causes the plasma to go from type I to type III ELMs at $t = 11.0 \text{ s}$ first, followed by an L-mode phase and finally a transition to M-mode at $t = 12.0 \text{ s}$, interrupted by transient back-transitions to L-mode. Published in [38].

with the observed X-point radiator but attached during L-mode (see Fig. 5.10, first described in [140]).

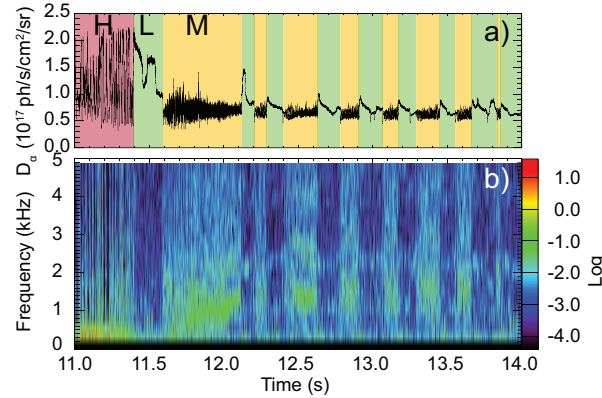


Figure 5.7: a) D_α signal from the inner divertor of JPN 85443 ($P_{\text{heat}} = 19$ MW). b) FFT spectrogram of poloidal Mirnov coil I803 (located at the lower HFS) for the neon-seeded phase of JPN 85443. The oscillation at 1–2 kHz indicates that the plasma is in M-mode. Up to $t = 11.3$ s ELMs can be seen until the plasma transits to L-mode and then to M-mode. In the following, further transitions to L-mode (characterised by a peaking in the D_α signal) and back to M-mode can be observed. Published in [38].

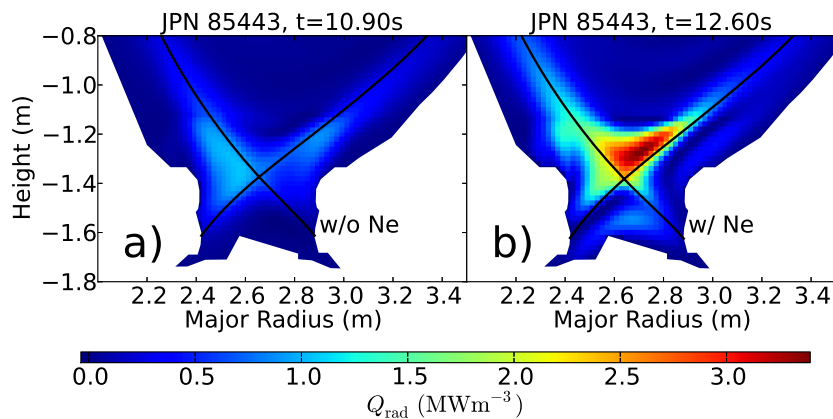


Figure 5.8: Tomographic reconstructions of bolometer data of a) an unseeded and b) a neon-seeded phase of JPN 85443 ($P_{\text{heat}} = 19$ MW). With neon puffing the region with highest radiation power density shifts from the HFS into the confined region close to the X-point. Published in [38].

5.2.3 High Heating Power (29 MW)

In the high power discharge, JPN 92357 with 29 MW heating power (see Fig. 5.11a), the neon puff was started during the ramp-up phase (see Fig. 5.11d) in order to cool the divertor and prevent tungsten sputtering. For this reason the initial ELMy H-mode phase is shorter than in discharges presented above. At $t = 9.8$ s and 10.1 s short transient back-transitions to L-mode can be observed. Until shortly after the end of the neon puff at $t = 14.0$ s the ELMs vanish. Oscillations with a frequency of around 1.5 kHz can be found in the voltage signal of outer divertor pick-up coils and in the temperature signal of pedestal ECE channels, suggesting that the plasma is in M-mode. Since an M-mode usually is observed close to the L-H power threshold this implies that a large fraction of the heating power must be radiated inside the

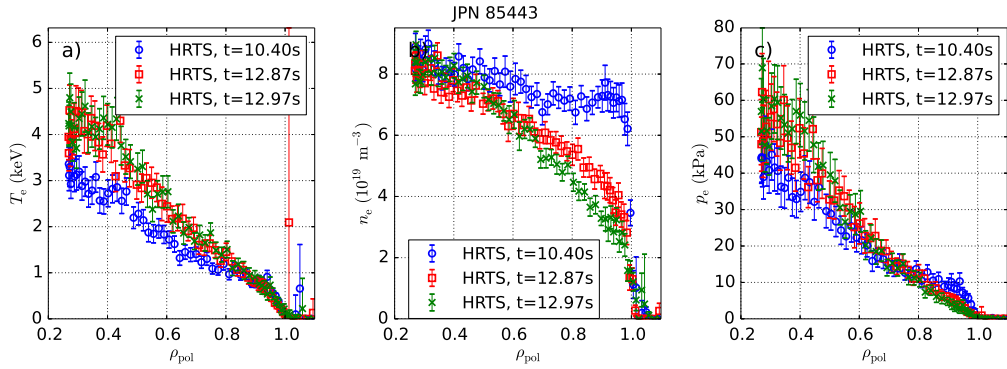


Figure 5.9: Median radial profiles of JPN 85443 ($P_{\text{heat}} = 19 \text{ MW}$) as in Fig. 5.3. The n_e profile of the neon-seeded time points (red and green) are strongly degraded with respect to the unseeded one (blue), especially in the pedestal region, and only reach the level of the unseeded time point in the core region. The density is slightly increased during M-mode phases (red) compared to L-mode phases (green). The T_e profiles have a similar shape in the pedestal region, while towards the core T_e is increased with neon seeding. Published in [38].

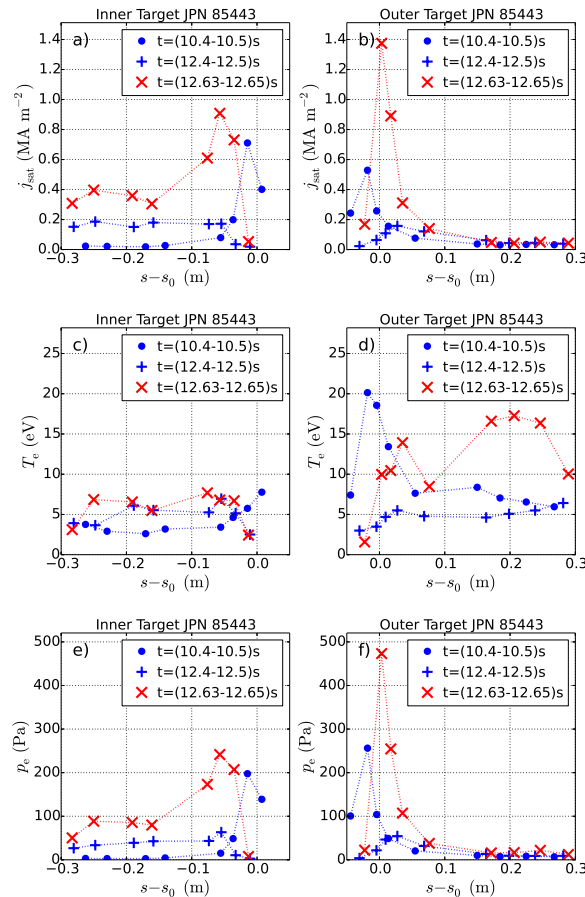


Figure 5.10: Time-averaged (median) target profiles of JPN 85443 ($P_{\text{heat}} = 19 \text{ MW}$) as in Fig. 5.5. In L-mode phases (red) the targets are attached while in H-mode (blue) they are in complete detachment. Published in [38].

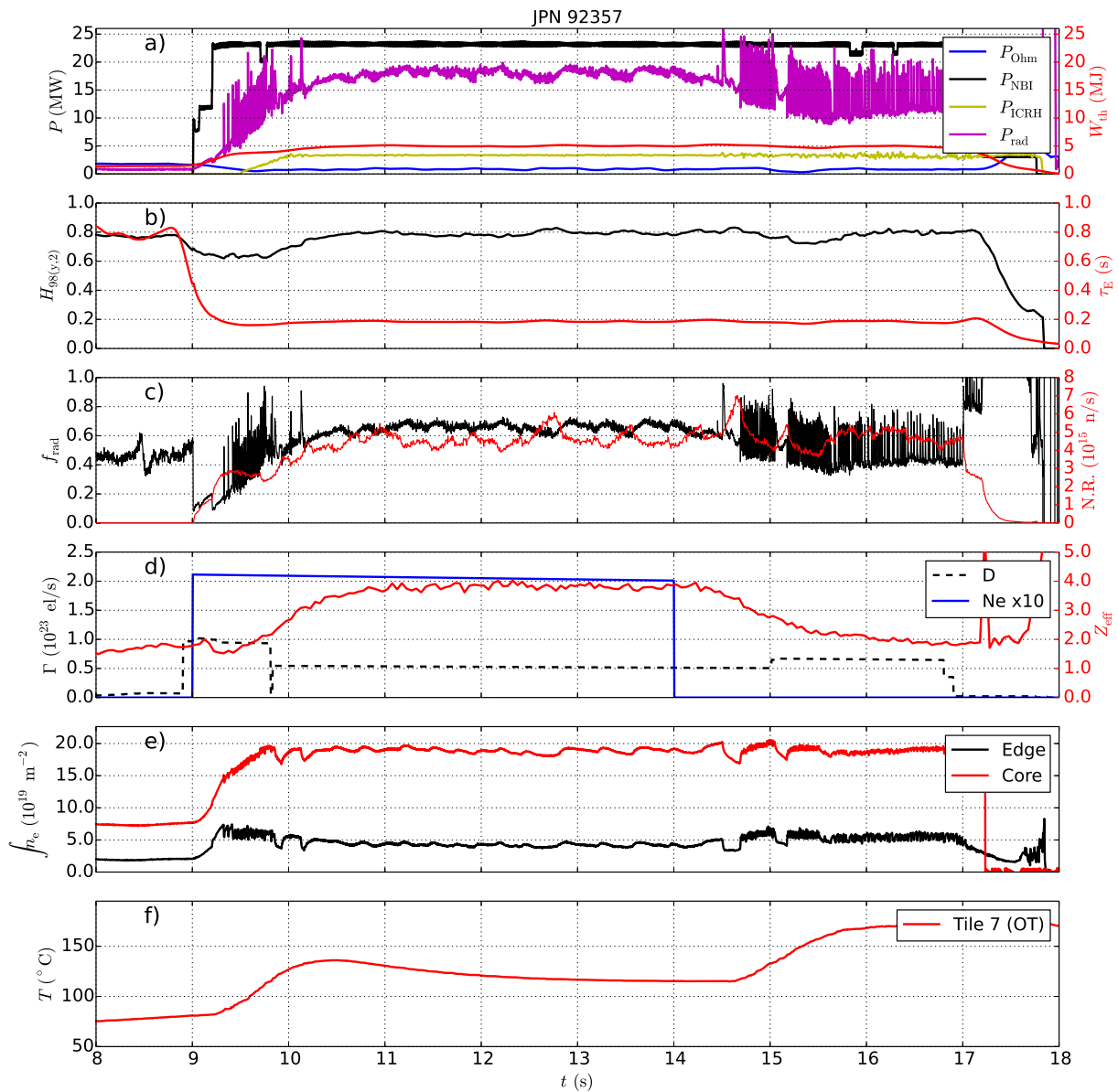


Figure 5.11: Timetraces of JPN 92357, a high power discharge ($P_{\text{heat}} = 29$ MW) with strong neon seeding. Quantities as described in Fig. 5.2. The neon puff starts at $t = 9.0$ s, leading to a transition to M-mode at $t = 10.2$ s where the plasma remains until after the end of the neon puff (at $t = 14.0$ s). Published in [38].

separatrix. Otherwise the discharge would be significantly over the L-H power threshold at the given heating power.

The discharge has a high radiative power fraction of $f_{\text{rad}} = 0.66$ (see Fig. 5.11c), while the highest radiation power density is at the X-point, inside the separatrix (see Fig. 5.12). Additionally, in this discharge it can be found that the radiation of the plasma centre increases, which could not be observed in the discharges discussed above. After the end of the neon puff this central radiation gradually disappears. At a core temperature of about 5 keV neon can be excluded as cause for this increased core radiation. As shown later in section 5.4 the tungsten concentration

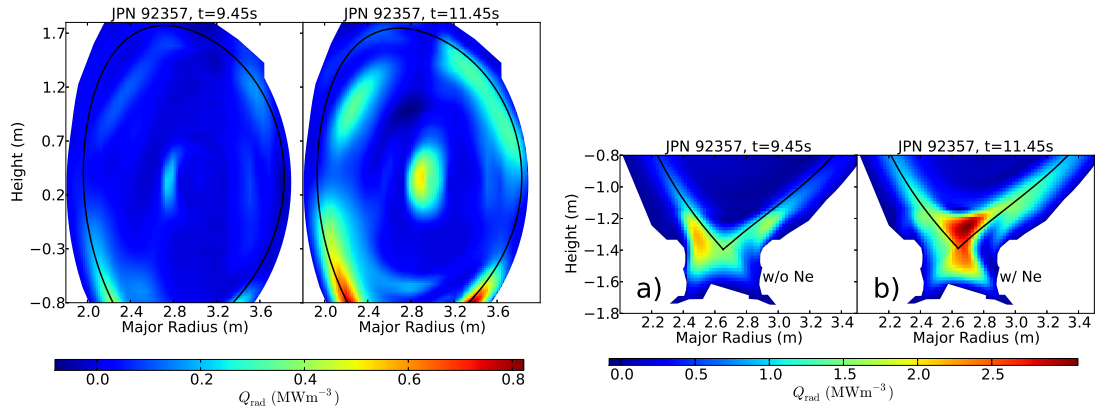


Figure 5.12: Core (left) and divertor view (right) of tomographic reconstructions of bolometer data of a) an unseeded and b) a neon-seeded phase of JPN 92357 ($P_{\text{heat}} = 29$ MW; note the different colour scales). With neon puffing the region with highest radiation power density shifts from the HFS into the confined region close to the X-point. With neon seeding increased radiation in the central core is observed, but it is unclear which effect causes it or if it is an artefact of the tomographic reconstruction. Published in [38].

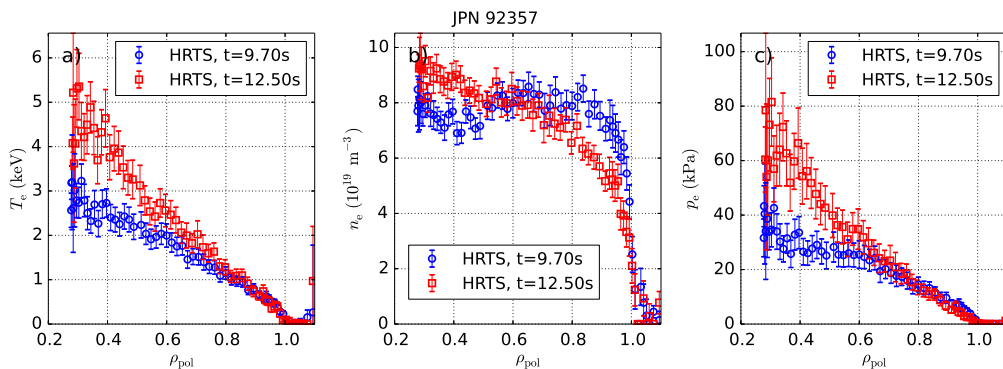


Figure 5.13: Median radial profiles of JPN 92357 ($P_{\text{heat}} = 29$ MW). The description and observations are similar as in Fig. 5.3. Published in [38].

is decreased during the neon seeding and can therefore be excluded as radiator as well. It is possible that the increased core radiation is an artefact from the tomographic reconstruction.

With neon seeding the n_e profile is degraded at the pedestal top while in the core it remains unchanged. T_e is increased in the core (see Fig. 5.13). Despite these significant changes the profiles undergo with neon seeding, the energy confinement time remains constant. The thermocouples at the outer target (see Fig. 5.11f; no data is available for the inner target) measure an increase in temperature between 35 and 55 °C, peaking at $t = 10.0$ s, shortly after the beginning of the neon puff, and then decreasing until after the end of the neon puff where it starts to rise again. The targets are completely detached (see Fig. 5.14). The temperature drops below the sensitivity level of the Langmuir probes of about 5 eV at the outer target with neon seeding, at the inner target these low temperatures are already measured earlier. The ion saturation current is increased at the outer target and an increase can be observed also at the inner target close to the

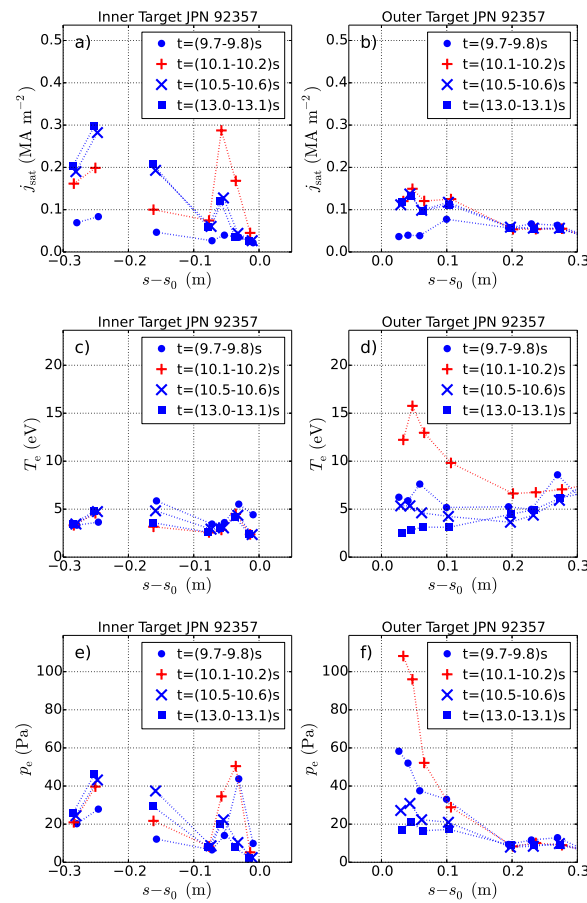


Figure 5.14: Time-averaged (median) target profiles of JPN 92357 ($P_{\text{heat}} = 29 \text{ MW}$) as in Fig. 5.5. In L-mode phases (red) the targets are attached while in H-mode (blue) they are in complete detachment. At the inner target one LP at $s - s_0 \approx -0.2 \text{ m}$ was broken and seems to have influenced adjacent probes. Published in [38].

strike point position. Both increases are small compared to the ion saturation current measured during an L-mode phase during ramp-up. For positions further from the strike point position at the inner target no statement about the ion saturation current can be made because a broken Langmuir probe at $s - s_0 \approx -0.2 \text{ m}$ seems to have affected the measurements of adjacent probes.

5.2.4 Influence of the Neon Puff on the L-H Transition

In the previous sections the influence of the heating power on the stability of the discharges at strong neon seeding was shown: at $P_{\text{heat}} = 15$ MW the discharge transits back to L-mode with the onset of neon puffing, at $P_{\text{heat}} = 19$ MW it switches between M-mode and L-mode, and even at $P_{\text{heat}} = 29$ MW the presence of an M-mode indicates the vicinity to the L-H threshold. It has to be noted, though, that the core radiation power in the discharges examined here was significant. Usually the L-H power threshold is estimated by the scaling presented in [70]. As the data used for this scaling were derived from machines with carbon as wall material, it might not be as accurate for devices with metallic walls as is JET-ILW with its tungsten divertor and beryllium first wall. In Fig. 5.15 the scaling

$$P_{\text{LH},18} = 0.031 \cdot B_{\text{axis}}^{1.29} \cdot \bar{n}_e \cdot S^1 \quad (5.1)$$

(with the following quantities, as used in this thesis: B_{axis} being the magnetic field at the plasma centre, \bar{n}_e the line-averaged density, and S the surface area of the separatrix) which was derived from JET-ILW data in VT configuration [73] (red points) was used to examine the proximity of the net heating power crossing the separatrix P_{SOL} to the L-H power threshold P_{LH} in several neon-seeded high radiation discharges. The scaling for VT configuration was chosen because the divertor configuration in JET has a strong influence on the L-H threshold.

Because current L-H scalings are derived from discharges with low f_{rad} (typically below 0.50), their results for discharges with a high radiative power fraction as presented here might be invalid. It can be seen in Fig. 5.15 that for all heating powers P_{SOL} almost all data points lie between 0.9 and $1.5 \cdot P_{\text{LH}}$, independently of the neon puff rate applied. The results presented here are in agreement with the previous observations of transitions to L-mode, transitions between L-mode and M-mode, and M-mode that implied the proximity of most of the examined discharges to the L-H threshold even at highest heating powers.

Although the heating power plays a major role for the characteristics observed in the discharges presented above, at a fixed heating power the plasma regime also strongly depends on the neon seeding level. JPN 87190 has a similar heating power (22 MW) as JPN 85443 but a neon puff rate of only about 50 % of this discharge (compare Figs. 5.6 and 5.16). In this less seeded discharge the plasma does not permanently enter the M-mode but mostly stays in ELMy H-mode. In contrast to the previously presented discharge JPN 92357 ($\Gamma_{\text{Ne}} = 2.0 \times 10^{22} \text{ es}^{-1}$, see Fig. 5.11), at high heating power ($P_{\text{heat}} = 29$ MW) the plasma in JPN 92359 (see Fig. 5.17) is not in an M-mode but in an ELMy H-mode with the first step of neon seeding ($\Gamma_{\text{Ne}} = 0.9 \times 10^{22} \text{ es}^{-1}$). An increase of the neon puff rate at $t = 11.5$ s to $\Gamma_{\text{Ne}} = 1.6 \times 10^{22} \text{ es}^{-1}$ leads to a transition to an M-mode regime with back-transitions to L-mode.

Figure 5.18 shows the fraction of radiated power as a function of the neon seeding rate in several high radiation discharges. With increased neon seeding the radiative power fraction f_{rad} increases, until a neon puff rate of $\Gamma_{\text{Ne}} \approx 1.0 \times 10^{22} \text{ es}^{-1}$ is reached where f_{rad} seems to saturate at values of $f_{\text{rad}} = 0.60$. A further increase of the neon puff rate over $2.0 \times 10^{22} \text{ es}^{-1}$ leads only to a small increase in the radiative power fraction up to $f_{\text{rad}} = 0.66$. This

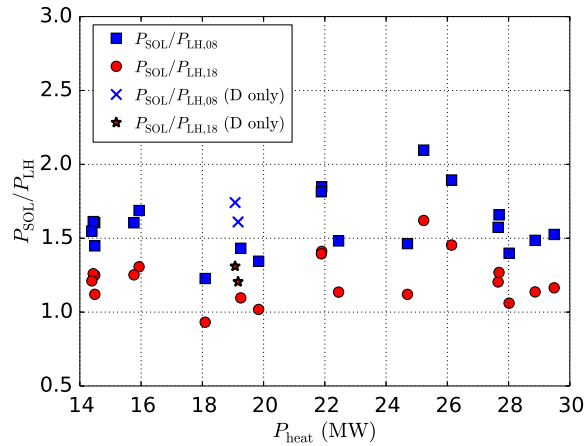


Figure 5.15: Power transported in the scrape-off layer P_{SOL} (see Eq. 2.7; including the X-point radiator) compared to the L-H threshold powers $P_{\text{LH},08}$ [70] (blue) and $P_{\text{LH},18}$ [73] (red; scaling for JET-ILW in VT configuration) as function of total heating power P_{heat} . For most heating powers P_{SOL} exceeds P_{LH} only by up to 50%. Only at highest heating powers P_{SOL} is significantly higher than P_{LH} . Published in [38].

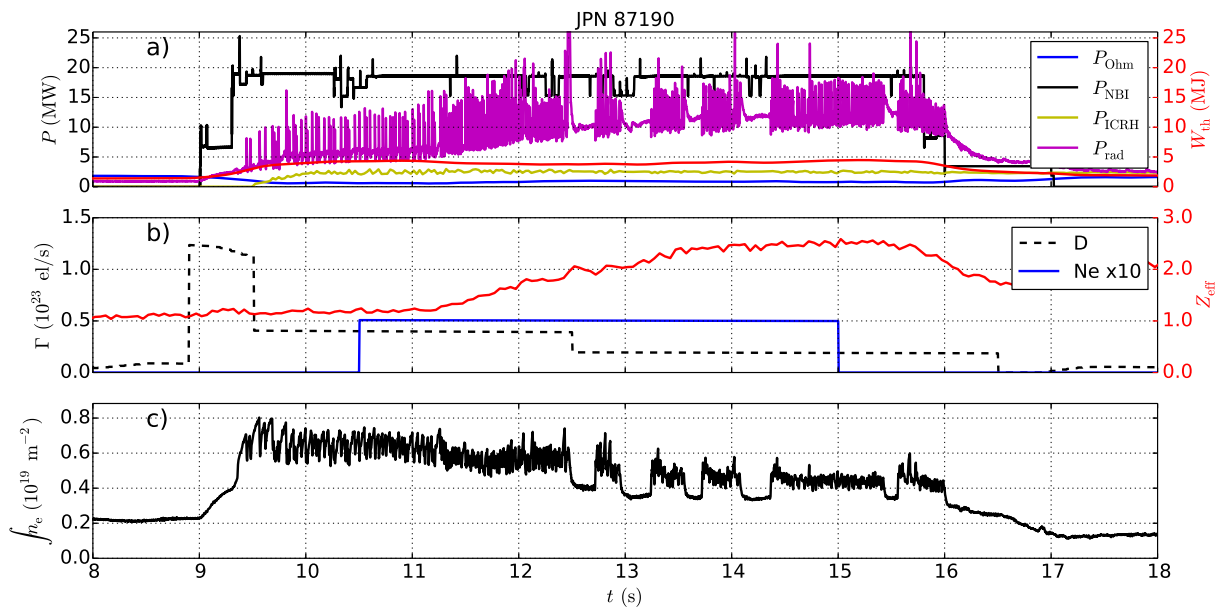


Figure 5.16: Timetraces of JPN 87190, a medium heated discharge ($P_{\text{heat}} = 22$ MW) with medium neon seeding. Quantities as described in Fig. 5.2. Published in [38].

value remains slightly below the JET maximum of $f_{\text{rad,max,JET}} = 0.75$ observed in complete detachment during nitrogen-seeded experiments [37]. The low maximum value of f_{rad} even under completely detached conditions indicates a discrepancy in the power balance at JET which is currently under investigation [144, 145].

In general, to permanently stay in the M-mode regime without transitions to L-mode a high neon seeding rate of $\Gamma_{\text{Ne}} > 1.0 \times 10^{22} \text{ es}^{-1}$ and a high heating power over 25 MW were necessary. All examined discharges in this M-mode without transitions to L-mode have a core radiation

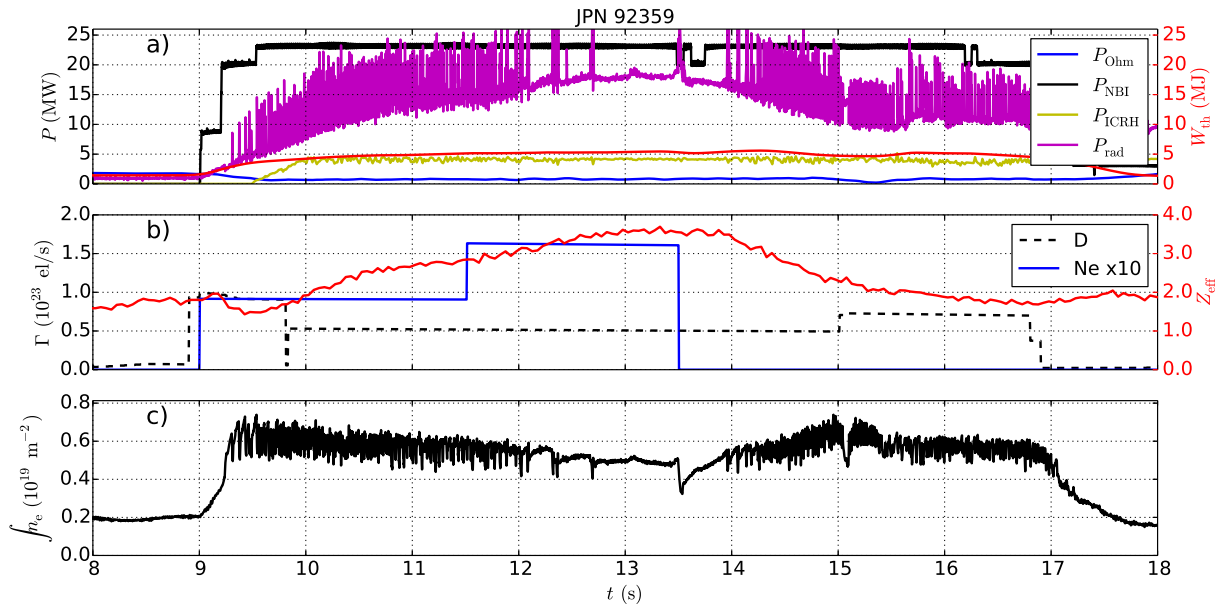


Figure 5.17: Timetraces of JPN 92359, a high heated discharge ($P_{\text{heat}} = 29 \text{ MW}$) with medium neon seeding. Quantities as described in Fig. 5.2. Published in [38].

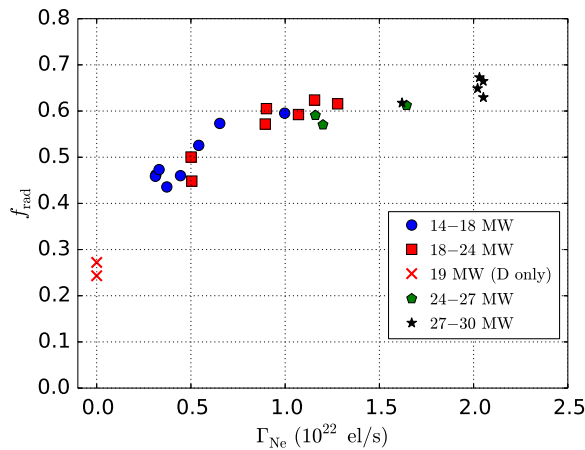


Figure 5.18: Radiated power fraction f_{rad} as function of the neon puff rate Γ_{Ne} . For puff strengths up to $\Gamma_{\text{Ne}} \approx 1.0 \times 10^{22} \text{ es}^{-1}$ the radiation is increased with increasing neon puff, for higher puff strengths the curve is in quasi-saturation. By increasing the neon puff, only minor increases in radiation can be achieved. The reasons for the low f_{rad} even with completely detached targets are yet to be determined [144, 145]. Published in [38].

power $P_{\text{rad,core}}$ of over 10 MW. The highest values of f_{rad} could only be reached with a neon puff rate of $\Gamma_{\text{Ne}} > 2.0 \times 10^{22} \text{ es}^{-1}$, though. Since the difference in terms of f_{rad} between discharges with $\Gamma_{\text{Ne}} = 1.0 \times 10^{22} \text{ es}^{-1}$ – $2.0 \times 10^{22} \text{ es}^{-1}$ and such with $\Gamma_{\text{Ne}} > 2.0 \times 10^{22} \text{ es}^{-1}$ is quite small (see Fig. 5.18), the radiative power fraction does not seem to play a role in the transition to a stable M-mode without transitions to L-mode, another plasma property affected by the neon puff might contribute to the suppression of transitions to L-mode.

5.3 Improved Core Energy Confinement

In the radial profiles of the discharges examined above the injection of neon leads to an increase in core temperature and a drop of pedestal density. At the same time the energy confinement improved. In this section it is analysed why the core temperature increases despite the increased radiation from inside the separatrix (Fig. 5.19), whether the density peaking has its origin actually in the pedestal (subsection 5.3.2) and what impact these effects have on the energy confinement (subsection 5.3.3) and on the fusion performance (subsection 5.3.4).

5.3.1 ASTRA-TGLF Transport Prediction of Core Temperature Profiles¹

To examine the increase of core temperature and the slight increase of the energy confinement time (see Figs. 5.2, 5.6, and 5.11) in all neon-seeded phases, a time point from the unseeded reference discharge JPN 84884 as well as one from the neon-seeded discharge JPN 85443 at medium heating power ($P_{\text{heat}} = 19 \text{ MW}$) have been simulated with the ASTRA-TGLF [265–268] transport code. The dots in Fig. 5.19 indicate the experimental data, red dots those from the unseeded and blue dots those from the neon-seeded discharge. Those in grey areas, i.e. the full n_e profile and the T_i profile for $\rho_{\text{tor}} > 0.75$, were used as prescribed input of the simulations. $T_i = T_e$ was assumed. The total NBI heating power in both discharges was similar. Since it has been observed in the experiment that due to the lower edge density the NBI penetrates further into the plasma, the radial NBI heating profiles (see Fig. 5.20) were considered in the simulations. The radiation strongly increases in the edge with neon seeding and was hence included in the simulations as well. Assuming that neon was the only impurity species, the neon content in the seeded case was estimated from Z_{eff} , resulting in a uniform concentration of around 1.3%. The core temperatures were predicted using the TGLF transport model. The solid lines indicate the simulation results derived from these data. The simulated electron temperatures reproduce the $T_{e/i}$ increase seen in the experimental profiles. A third dashed line shows the result of a simulation similar to the one of the neon-seeded time point with the only difference being that the neon species has been removed from the simulation. This means that $n_i = n_e$. All other quantities, including the entire n_e profiles, $T_{e/i}$ (for $\rho_{\text{tor}} > 0.75$), Q_{rad} and Q_{NBI} profiles, and Z_{eff} remained as given by the neon-seeded experimental data.

When in simulations based on profiles for the seeded phase (solid blue line in Fig. 5.19) neon is removed (dashed blue line), the temperature drops below the values from the simulation of the unseeded phase (red line). This shows that effects introduced by the impurity other than radiation are responsible for the core confinement improvement. The ASTRA-TGLF simulations suggest that a dilution of the main ion density by the neon impurity reduced the edge ion pressure gradient and thus stabilises the ion temperature gradient (ITG) mode. The ITG turbulence is driven by the majority ion species (D) at the most unstable wavenumber. Due to the addition of neon, the deuterium ion density decreases with respect to the electron density, which pushes the turbulence from the ITG towards the electron drift wave. Hence, the ITG turbulence decreases in amplitude and the ion heat diffusivity is reduced, allowing T_e to increase. This so-called “dilution” effect is valid until neon becomes the majority species. Since ITG turbulence is

¹Analysis performed by Emiliano Fable. Published in [38].

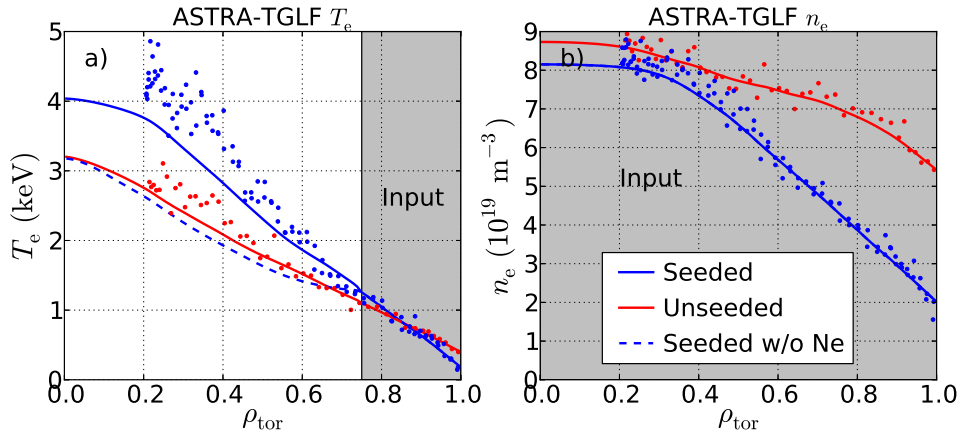


Figure 5.19: Experimental electron density and temperature data (dots) of a neon-seeded (blue, JPN 85443, $t = 12.8$ s) and an unseeded (red, JPN 84884, $t = 13.0$ s) discharge, compared to ASTRA-TGLF simulation results (solid lines) based on the experimental data in the grey areas. The dashed line marks the results of a simulation of the neon-seeded time point with the neon species removed from the simulation while all other parameters were kept constant. Published in [38].

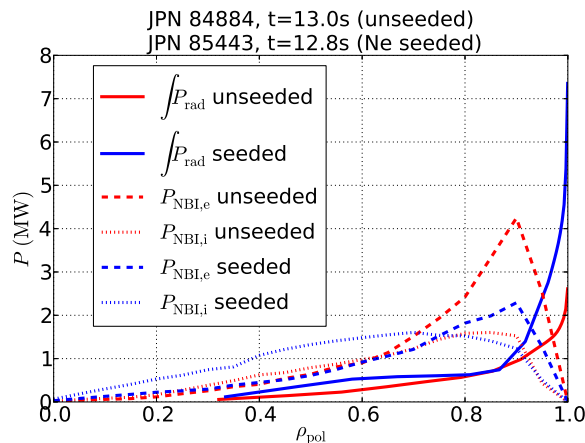


Figure 5.20: Radial profiles of deposited power by the NBI heating (dashed and dotted lines) and radially integrated radiation (solid lines) for time points with (blue) and without (red) neon seeded. Due to lower edge density, the NBI deposition is shifted towards the core when neon is seeded. The radiation at $\rho_{\text{pol}} > 0.90$ is significantly increased with neon seeding. Published in [38].

driven by the ion temperature gradient, the reduction in density gradient, which acts as a passive element, is not relevant for this process. This stabilisation of ITG modes leads to increased core temperatures and therefore to an improved core energy confinement [269, 270]. The effect of increased confinement observed in the core is to distinguish from a potentially counter-acting effect in the pedestal region where the increased radiation might lead to a reduced energy confinement. In fact, the overall confinement time remains nearly constant, suggesting an effect opposed to the core confinement improvement. In other JET discharges with neon seeding rates in the range up to $5 \times 10^{21} \text{ es}^{-1}$ it was also found that the neon seeding had no effect on the confinement, but on the fusion performance due to increasing density and decreasing temperature (which is in contrast to the decreasing density and increasing temperature reported above) [271].

A doping effect, i.e. that the neon affects the plasma beyond the replacement of deuterium, as described in [272], was observed in these low neon-seeded discharges. This effect could not be observed in the highly seeded discharges presented in this thesis which might be attributed to their lower Z_{eff} level.

5.3.2 Density Peaking

In another study of neon-seeded JET discharges at significantly lower neon seeding rates a peaking of the electron density [272, 273], i.e. an increase of the ratio of core to pedestal density, $n_{e,\text{core}}/n_{e,\text{ped}}$ (with the core position at $\rho_{\text{pol}} = 0.25$), was observed while the volume averaged density was decreased [271]. This was caused by an inward particle pinch. In our experiments with higher neon seeding rates a density peaking could be observed as well (see Fig. 5.21). In Fig. 5.21 the core and pedestal top electron densities relative to the line-averaged electron density \bar{n}_e are shown. Due to the degradation of the pedestal and hence the absence of a proper pedestal top position, the pedestal top position was taken from the unseeded reference discharge, at $R_{n,\text{ped}} = 3.79$ m; the core density was measured at a line of sight with $R_{n,\text{core}} = 3.30$ m. It is clearly visible that with increased neon puffing rate the relative core density remains constant while only the relative pedestal top density decreases. The density peaking can therefore be attributed to a density decrease in the pedestal region rather than an increase in the core. The reason for the degraded pedestal density as well as the expected impact of the larger gradient on the transport has yet to be investigated.

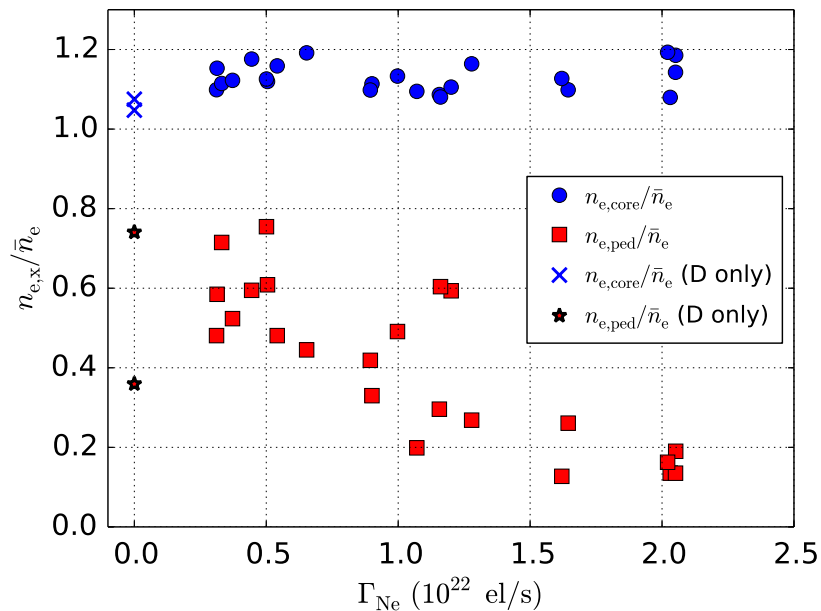


Figure 5.21: Electron density in the core (blue, measured at $R = 3.30$ m) and at the pedestal top (red, measured at $R = 3.79$ m) relative to the line-averaged density \bar{n}_e . Due to the degraded pedestal the pedestal top position was defined by the pedestal top position of an unseeded reference discharge. The neon puffing seems to affect only the pedestal region. Published in [38].

With a decreasing pedestal top density and a nearly constant pedestal top temperature the pedestal top pressure is decreasing as well. It can be observed, though, that $H_{98(y,2)}$ does not correlate with the pedestal top pressure (see Fig. 5.22). Thus, the decrease of the pedestal top pressure does not affect the global energy confinement time. Instead, the effect of more stable ITG modes in the core was shown to be the dominating influence on the confinement.

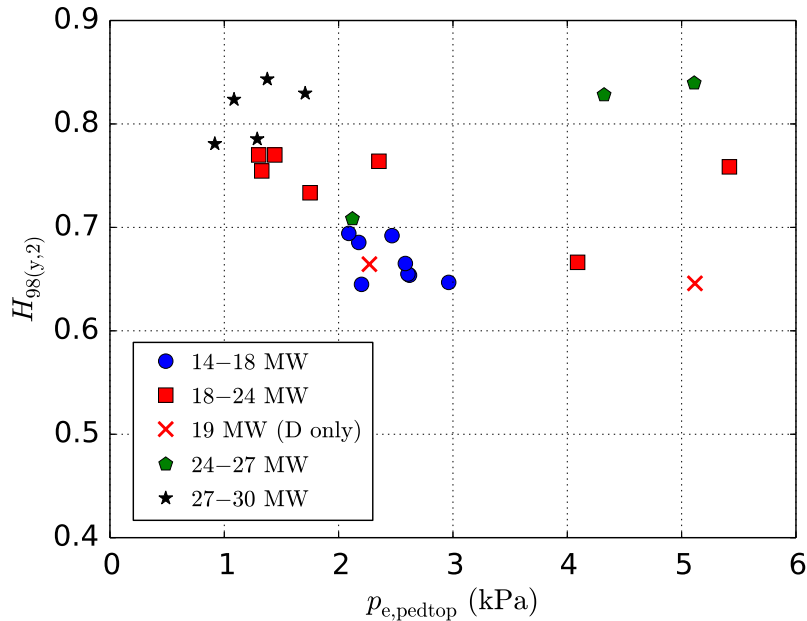


Figure 5.22: $H_{98(y,2)}$ as function of pedestal top pressure p_{pedtop} . A correlation can not be found. Published in [38].

5.3.3 Energy Confinement

With respect to future fusion devices the effect of neon seeding on the energy confinement has to be studied. In Fig. 5.23 the confinement factor $H_{98(y,2)}$ versus the normalised plasma β_N (see Eq. 2.3) is shown. For ITER, at $\beta_N = 1.8$ an $H_{98(y,2)}$ of 1.0 is required to reach the scientific goal of $Q = 10$ (see subsection 2.1.1) [47]. In the present discharges a maximum value of only $H_{98(y,2)} = 0.85$ was reached at highest heating powers. It has to be considered, though, that the unseeded discharges have already a low $H_{98(y,2)}$ value. As it was shown in the previous sections, neither the energy confinement time τ_E nor the confinement factor $H_{98(y,2)}$ change significantly with the onset of the neon puff. However, it has already been found that the vertical target configuration leads to lower confinement than the corner configuration (see subsection 4.4.3) [249, 253] and that high D_2 puff rates decrease the confinement as well [248, 249, 260]. In the JET campaign M18-38 similar neon-seeded discharges at lower densities were performed but the observed higher $H_{98(y,2)}$ of up to 0.95 is likely related to their higher β_N (up to about 1.8). Furthermore, the lower densities in these pulses might have caused a reduction in core radiation power and hence impact P_{SOL} and the stability of the M-mode phase. Thus, the cause for the low $H_{98(y,2)}$ lies rather in the target configuration and in the high D_2 puffs than in the neon puff. Though, a deeper analysis of these experiments has yet to be performed.

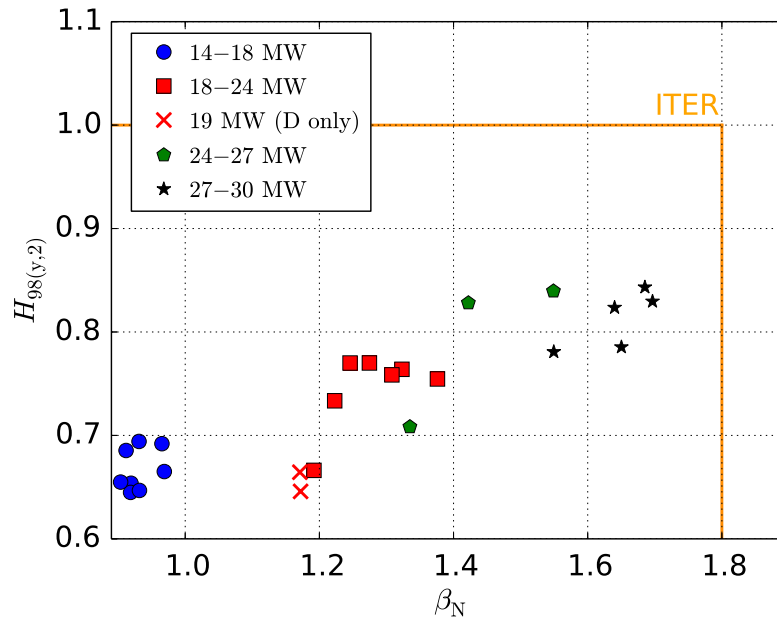


Figure 5.23: Confinement factor $H_{98(y,2)}$ as function of normalised β_N . The ITER target value of $H_{98(y,2)} = 1.0$ at $\beta_N = 1.8$ [47] could not be met with the neon-seeded discharges. The unseeded discharges have equally low values due to the high deuterium puff. Published in [38].

5.3.4 Neutron Rate

In present-day tokamaks like JET the neutrons are primarily created by the interaction of the NBI deuterons with the thermal deuterons (so-called beam-target reactions) rather than by the interaction of thermal deuterons amongst each other. In Fig. 5.24 it is shown how the neutron rate increases with increased neon puffing. The dependence on the heating power is less pronounced. The result shown here is in contrast to [271–273], where a decrease of the neutron rate from $4.5 \times 10^{15} \text{ s}^{-1}$ to $2.5 \times 10^{15} \text{ s}^{-1}$ has been observed in a comparison between a discharge that was seeded at a puff rate of $\Gamma_{\text{Ne}} = 2 \times 10^{21} \text{ es}^{-1}$ and an unseeded discharge [272, 273]. This is explained by the authors with a decrease in the core ion temperature. In the experiments presented in this thesis the opposite is observed: an increased core ion temperature and an increased neutron rate with neon seeding. Further reasons for the increase of the neutron rate in the highly neon-seeded discharges are yet to investigate. It is possible that the deeper penetration of the NBI beams in the plasma due to the degraded pedestal density (while the core density remains constant and the ion temperature increases) might have an impact on the neutron rate, e.g. due to a better confinement and increased slowing down time of the fast beam particles. An increasing neutron rate was also observed in nitrogen and neon-seeded discharges under a similar experimental setup [143].

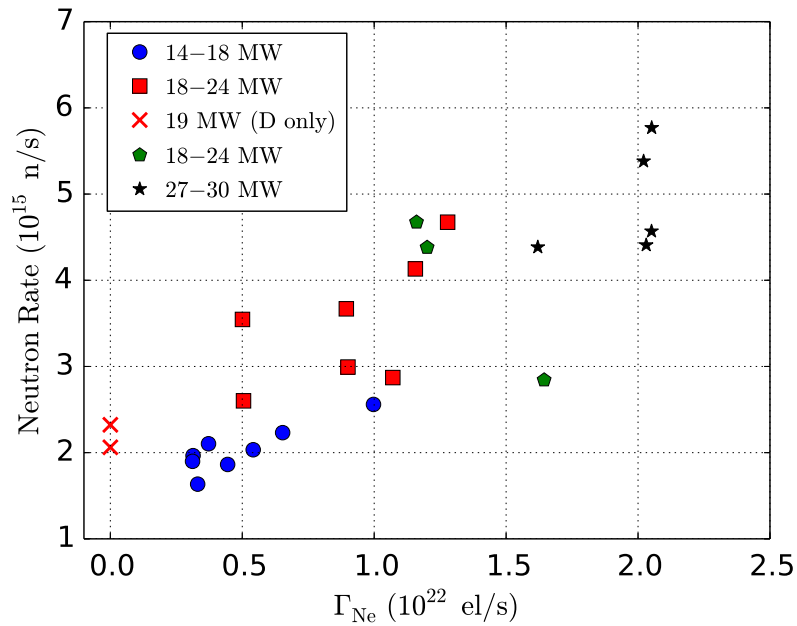


Figure 5.24: Neutron rate as function of the neon seeding rate Γ_{Ne} . An increase of the neutron rate with increased neon seeding can be seen. Published in [38].

5.4 Impurity Content²

The core impurity concentration in fusion plasmas is to be kept as low as possible. The deteriorating effect of an impurity depends mainly on its charge state [34]. E.g., the maximum permitted tungsten concentration is in the order of some 1×10^{-5} . Since seeded impurities could increase the sputtering of wall material the influence of neon seeding on the concentrations of typical wall materials are studied. The concentrations of up to 4 different impurity species can be determined in JET-ILW in a recently developed approach [275, 276] which aims to match the measurements from the following diagnostics: soft X-ray emission, passive vacuum-ultra-violet spectroscopy, the line-of-sight integrated measurement of the effective charge Z_{eff} , the observed poloidal asymmetry of the SXR emission and the line-of-sight integrals of the total radiation as measured by bolometry [274]. The spatially constant neon concentration can be calculated from Z_{eff} under the assumption that the concentration of beryllium from the main chamber wall of JET-ILW is also constant over space and time. Considering the radiation from neon and beryllium the tungsten concentration is determined from the SXR emission. Nickel was included to represent the radiation of metallic impurities and is expected to have a similar density distribution as W [274, 276].

The results of this analysis are shown in Fig. 5.25 for JPN 92357. It is observed that after the end of the neon puff at $t = 14.0$ s the tungsten density increases slightly, implying that the detached divertor diminished the tungsten sputtering despite the increased sputtering potential of neon. This observation is verified by the W I signal of the visible light spectroscopy in the inner divertor that demonstrates an equal or reduced gross tungsten erosion in the three neon-seeded

²Analysis performed and parts of text provided by Marco Sertoli [274]. Published in [38].

pulses presented in section 5.2 compared to the unseeded reference pulse JPN 84884. Since in the analysis method the nickel density distribution is based on the tungsten density distribution the trends for nickel are the same. In JPN 87195 (similar to JPN 87196 presented above) with the onset of the neon seeding the nickel and the tungsten concentrations decrease. The tungsten concentration in JPN 85443 demonstrates a contrary behaviour: after the beginning of the neon seeding the tungsten concentration increases. An increase of these concentrations during the starting phase of the discharge was observed also in JPN 87195, but in JPN 85443 the concentrations do not decrease when the neon is puffed. This might be attributed to the H-L-H-transitions which are not present in the other two discharges.

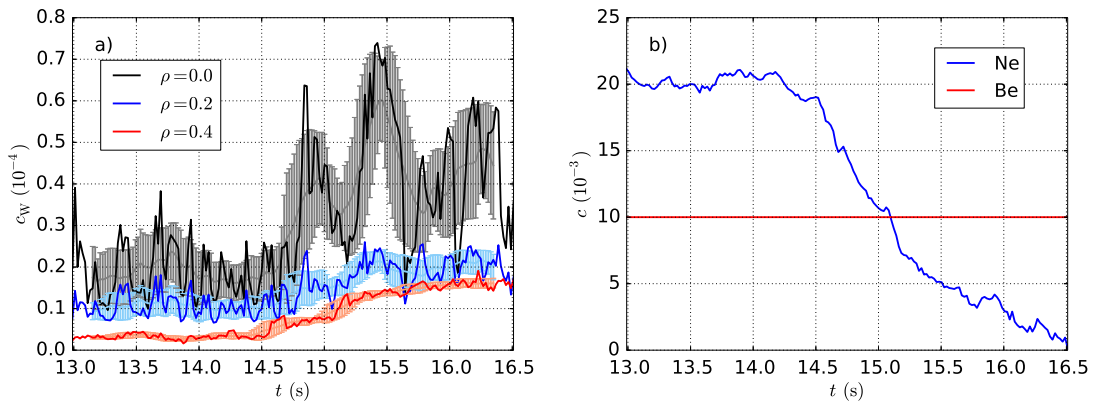


Figure 5.25: Results of the impurity content analysis [275, 276] for JPN 92357. a) Time evolution of the tungsten concentration c_W at three different radial positions. The light-coloured lines and errorbars exhibit the moving average mean and standard deviation (window size: 320 ms). After the end of the neon puff at $t = 14.0$ s c_W increases. Since the nickel concentration depends on the tungsten concentration in the analysis, it exhibits the same trend. b) Time evolution of the neon concentration (fixed in radius) and the beryllium concentration (fixed in radius and time). Published in [38].

As a measure for the generalised impurity concentration of the plasma, Z_{eff} can be studied. Figure 5.26 shows that with increased neon seeding also Z_{eff} increases. This seems conflicting with the increase of the neutron rate with increased neon seeding because an increased impurity content leads to a dilution of the plasma and to decreased beam-target reactions. A hollow neon density profile as a possible explanation is rather unlikely since the impurity content analysis as well as the ASTRA-TGLF simulations assumed flat neon density profiles and successfully reproduced experimental measurements. There are no spectroscopic measurements of the radial neon distribution yet. As discussed at the end of the previous section, another reason for the increasing neutron rate could lie in the decreased pedestal density which permits a larger fraction of the NBI beam power to be deposited in the core, outweighing the dilution by neon.

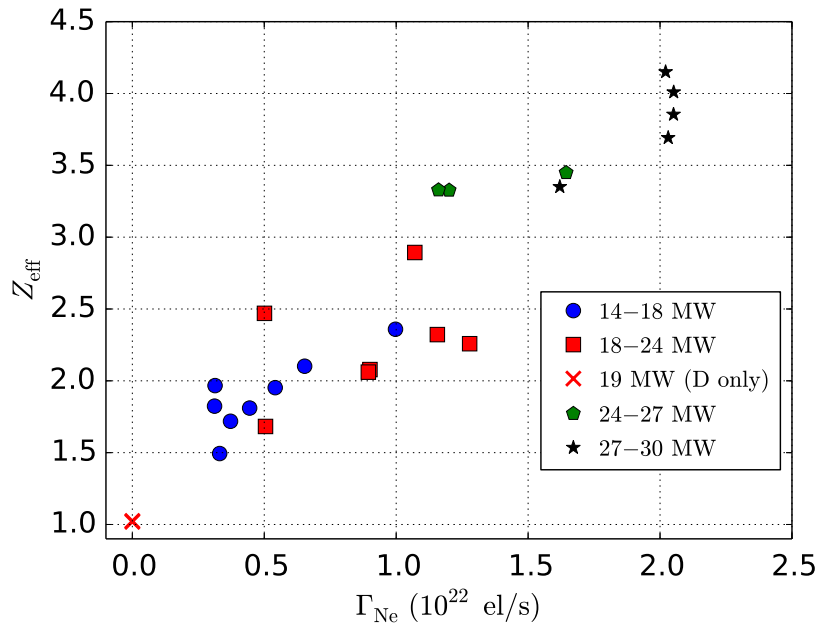


Figure 5.26: Line-averaged effective charge state Z_{eff} as function of the neon puff Γ_{Ne} . Published in [38].

5.5 Poloidal Radiation Distribution

It was shown in Fig. 5.18 that the radiative power fraction almost saturates when the neon seeding rate is increased above $\Gamma_{\text{Ne}} \approx 1.0 \times 10^{22} \text{ es}^{-1}$. The distribution of the radiation might change at the highest neon puffing rates, though. Figure 5.27 (left) shows the radiation powers from the divertor, the core (defined as the region inside $\rho_{\text{pol}} = 0.95$) and the pedestal region ($0.95 < \rho_{\text{pol}} < 1.0$, including also an eventually existing X-point radiator) as function of the neon puff rate (for a graphical representation of the area definitions see Fig. 6.2(right)). While at low neon puff rates the divertor radiation power is similar to the core and the pedestal radiation power (around 2 MW each), the radiation from the core and particularly from the pedestal region are increased up to 6–8 MW with increasing neon seeding. The divertor radiation barely increases (only up to 4 MW), which is in accordance with [37], where a maximum of the divertor radiation power as function of the neon seeding rate has been found. Figure 5.27 (right), where the radiation powers were divided by the respective heating powers (i.e. the radiative power fractions) are shown, even suggests that the effect of saturating/decreasing divertor radiation is independent of the heating power.

For the dependency of the radiation powers on the heating power a similar picture can be found (not shown): up to a heating power of $P_{\text{heat}} = 24 \text{ MW}$ divertor, pedestal, and core radiation powers are similar, increasing up to 4 MW. With increasing heating powers pedestal and core radiation powers increase further up to around 7 MW while the divertor radiation power decreases to 2 MW. The line-averaged densities of the neon-seeded discharges presented in this thesis are in the same range (around $5 \times 10^{19} - 7 \times 10^{19} \text{ m}^{-3}$), thus a density dependence cannot be discriminated. It should be noted, though, that the accuracy of the magnetic equilibrium reconstruction and the spatial resolution of the bolometer system do not permit exact calcula-

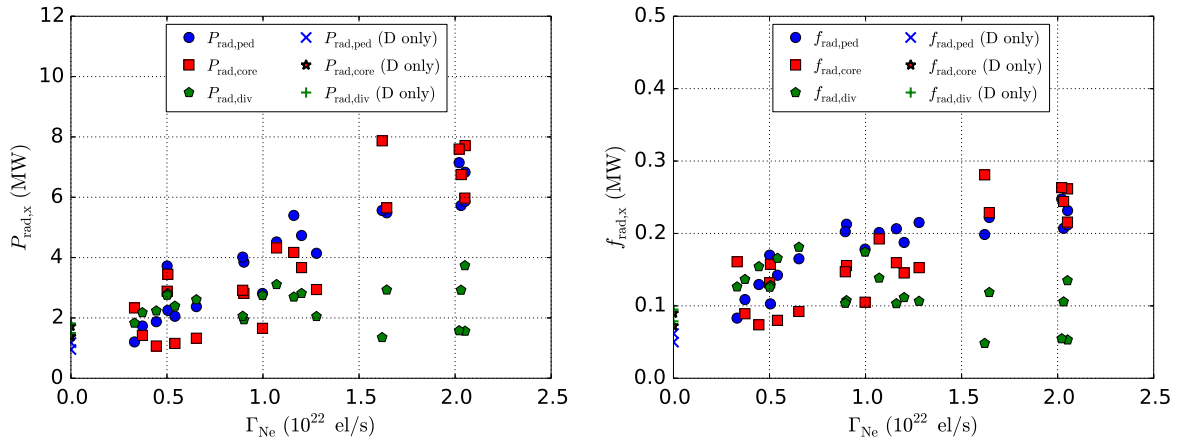


Figure 5.27: Radiation powers (left) and radiative power fractions (right) of divertor, core (inside a roughly estimated pedestal top position, $\rho_{\text{pol}} < 0.95$) and pedestal (between pedestal and separatrix, $\rho_{\text{pol}} < 0.95$) as function of Γ_{Ne} . For a graphical representation of the area definitions see Fig. 6.2 (right). The radiation power is primarily increasing in the pedestal region and in the core (by a factor of 5–6 between the lowest heated and the highest heated discharge), while the radiation power in the divertor increases by up to a factor 4 for its highest values and even saturates and decreases for its lowest values. The right figure shows that this effect of decreasing divertor radiation is independent of the heating power. Left figure published in [38].

tions of radiation powers for the single areas – especially in the narrow pedestal region – and that the values presented here can therefore only give indications.

A correlation between the radiation power of the X-point region (defined as the region with $\rho_{\text{pol}} \leq 1.0$ and $z \leq -1.2$ m) and the core radiation power could be observed: With increasing core radiation power the radiation power of the X-point increases approximately linearly. A correlation between the formation of the X-point radiator and the neon seeding rate was not observed. Even though all discharges with neon puff rates $> 0.5 \times 10^{22} \text{ es}^{-1}$ had an X-point radiator, there were also discharges found with lower neon seeding rates and X-point radiator. The density range of the presented discharges was too small to see clear dependencies of the X-point radiator on the line-averaged density, especially at low heating powers. The maximum X-point radiation power is around 1–2 MW. A detailed analysis of the X-point radiator by spectroscopic or numerical means (as shown for ASDEX Upgrade in [139, 152]) are yet to be performed.

In all of the neon-seeded discharges examined for this thesis, it was observed that the appearance of the X-point radiator (see subsection 2.5.2), the degradation of the pedestal density, and the detachment of both divertor targets are correlated with each other under the following conditions:

1. The plasma is in stable H-mode or M-mode. During L-mode phases, during L-H/H-L-transitions, and during the plasma ramp-up phase one or more of the aforementioned phenomena, and therefore also their correlation, might not be observed.
2. Neon is being puffed. At the beginning of the neon puff, it takes some time (1.0–1.5 s) until the neon takes effect; in this period these phenomena might not be observed. After

the end of the neon puff the neon is pumped out and thus, both the X-point radiator and the pedestal degradation are not observed any longer.

In neon-seeded discharges with an initial type I ELMy H-mode phase it is observed that with the formation of the X-point radiator and the degradation of the density pedestal the plasmas undergo a transition from type I to type III ELMs. A correlation of the formation of the X-point radiator with the transition to M-mode was not observed.

5.6 Summary and Discussion

The seeding of impurities is crucial in future fusion devices like DEMO in order to protect the divertor target tiles. In this chapter it has been discussed what impact strong neon seeding can have on the core, pedestal, and divertor conditions. In M-mode phases, which are in JET typically found close to the L-H power threshold, the joint appearance of an X-point radiator, a degraded density pedestal, and the detached targets was observed. In L-mode phases it was noted that at least one of the divertor targets was attached, independently of the presence of an X-point radiator. A degradation of the density pedestal could not be seen in L-mode. The detached M-mode phases might not be problematic with regard to future fusion devices, the back-transitions into attached L-mode surely are due to their peak heat load. Only at high heating powers ($P_{\text{heat}} > 25 \text{ MW}$) and high neon puff rates ($\Gamma_{\text{Ne}} > 1.0 \times 10^{22} \text{ es}^{-1}$) the plasma enters an M-mode regime without back-transitions to L-mode. In these discharges the targets are completely detached.

Through ASTRA-TGFL simulations it could be found that neon stabilises the ITG mode in the core due to the dilution effect, leading to higher core temperatures and together with a somewhat degraded pedestal approximately constant energy confinement times. While the core profiles are not negatively affected by neon seeding, in the pedestal a degradation of the electron density is observed. As this coincides with a strong increase of radiation power density in the edge including the X-point region, a correlation between the increased edge radiation and the pedestal density degradation might be possible.

Detachment is characterised by a drop of pressure between the midplane and the target position. Since, compared to core and pedestal radiation, only a small increase of divertor radiation power of maximum 2 MW was observed, it is questionable if an increased divertor radiation leads to the pressure drop in front of the targets. Based on the available data it was experimentally not possible to determine if a degraded pressure profile upstream at the separatrix causes the pressure drop at the targets.

Due to the strong seeding with high radiative power fractions, detached targets, and no loss of energy confinement, the regime found in these experiments seems to be potentially interesting for future fusion devices. Its suitability for such devices is worth to be further examined. Even though the divertor radiation power was limited, the radiation inside the separatrix could be increased without a degradation of the energy confinement. The low energy confinement at unseeded time points are caused by the target configuration and the high deuterium puff. The energy confinement might increase in more favourable target configurations and at lower den-

sities. It should be clarified if in such discharges with higher energy confinement at unseeded time points the trend of a constant or slightly increasing energy confinement with neon seeding can be observed similarly as presented here.

Even though the dilution of the main ion species with neon leads to a beneficial stabilisation of the ITG mode in the core and to a decreasing tungsten concentration, especially in the core, the neon itself might also enrich in the plasma core. Further spectroscopic measurements are required to tackle this question. This might determine if the flushing effect of ELMs is required to keep the core plasma clean.

Numerical modelling, e.g. by core transport codes, pedestal stability analysis, or two-dimensional SOL codes, can support the understanding of the experimental findings. In the following chapter the results of two-dimensional SOLPS-ITER simulations are presented. Their setup was based on the features of the pulses shown in this chapter, which allows to validate their results against the experimental results. The main focus of the simulations was on reproducing the most important experimental findings, especially the poloidal radiation distribution: does the seeding of neon lead to increased core and edge radiation powers, to a saturation of the divertor radiation power, and to the formation of an X-point radiator? This might give valuable information about the quality of the applied model. So far, at JET the EDGE2D-EIRENE simulation of the X-point radiator with nitrogen seeding led to numerical issues [163]. At ASDEX Upgrade, the X-point radiator could be reproduced with SOLPS modelling with nitrogen seeded [152]. The simulations also allow to analyse the role of the X-point radiator in the detachment process and their relation with the degradation of the pedestal pressure.

6 SOLPS-ITER Modelling

Since the experimental results presented in chapter 5 are promising in view of future devices, numerical SOLPS-ITER simulations of scenarios similar to the experiment were set up. They can provide further, partly experimentally inaccessible, insight into the effect of neon seeding on the radiation distribution (especially in view of the X-point radiator) and the ability to reduce the heat load onto the targets. The goal of the simulations presented below was not to reproduce experimentally measured quantities (even though experimental parameters were used in the setup of the simulations; see section 3.4) but rather to reproduce qualitative characteristics of neon-seeded plasmas. At first, the setup of the simulations is introduced in section 6.1. In the following, the radiation distribution is analysed in section 6.2, the loss of pressure at the targets in section 6.3, and the impurity distribution in section 6.4. The results of the simulations as well as effects not considered in the simulations and their possible consequences on the simulations are discussed in section 6.5.

6.1 Setup

In the following sections the features of a set of simulations with

- constant heating power $P_{\text{heat}} = 20 \text{ MW}$
- constant deuterium core density $n_{\text{D}^+, \text{core}} = 1 \times 10^{20} \text{ m}^{-3}$
- increasing neon core density $n_{\text{Ne}^{10+}, \text{core}} = 0 \times 10^{17} - 9 \times 10^{17} \text{ m}^{-3}$ (in steps of $1 \times 10^{17} \text{ m}^{-3}$)

are characterised. The maximum neon core density was chosen in order to reach similar values for the midplane-averaged effective charge as in the experiment ($Z_{\text{eff}, \text{max}} \approx 3-4$), but also because cases with higher neon content proved to be numerically unstable. The majority of results in this chapter was derived from the series of simulations just introduced. However, an advantage of numerical simulations is that their parameter range can be expanded rather easily and beyond experimental references. This was done in a further series of simulations with the parameter ranges

- $P_{\text{heat}} = 20-35 \text{ MW}$ (in steps of 5 MW)
- $n_{\text{D}^+, \text{core}} = 7 \times 10^{19} - 10 \times 10^{19} \text{ m}^{-3}$ (in steps of $1 \times 10^{19} \text{ m}^{-3}$)
- $n_{\text{Ne}^{10+}, \text{core}} = 0 \times 10^{17} - 8 \times 10^{17} \text{ m}^{-3}$ (in steps of $1 \times 10^{17} \text{ m}^{-3}$)

They were created by first step-wise decreasing the density of the first simulation series, followed by a variation of the heating power. The results of this second series are only of limited use due to numeric instabilities at high neon densities in the first series. If not mentioned otherwise, data presented below are therefore from the first series in which only the neon content is varied.

6.2 Poloidal Radiation Distribution

The poloidal radiation distribution has a major impact on the plasma and is strongly altered by the seeding of neon. In Fig. 6.1 the radiation power densities in the divertor area of an unseeded (left) and a neon-seeded SOLPS-ITER case (right; $n_{\text{Ne}10+, \text{core}} = 7.0 \times 10^{17} \text{ m}^{-3}$) are compared. In the unseeded simulation case the radiation is concentrated in the divertor legs, especially in the proximity of the targets. With neon seeding the radiating zone extends along the divertor legs and along the separatrix into the pedestal region and the inner SOL. The radiation around the X-point is increased with respect to the unseeded case, but the highest radiation power densities are still located close to the targets, indicating that no X-point radiator is present in this case.

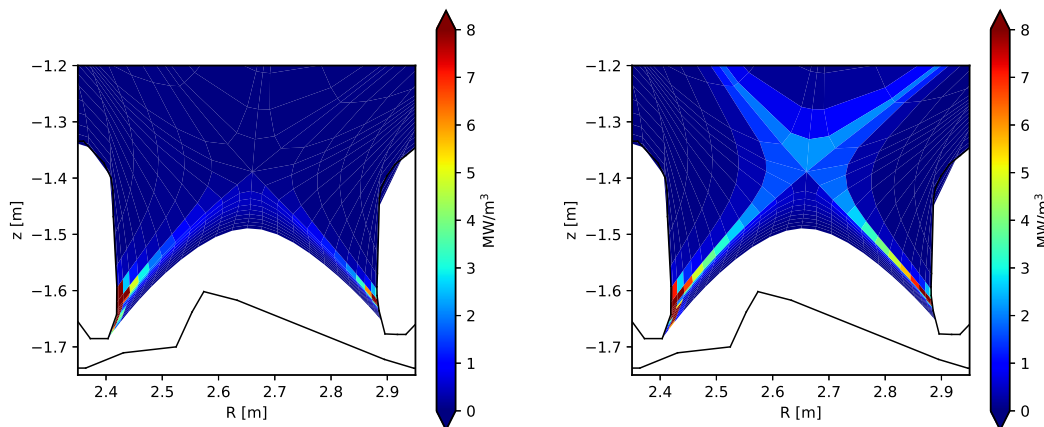
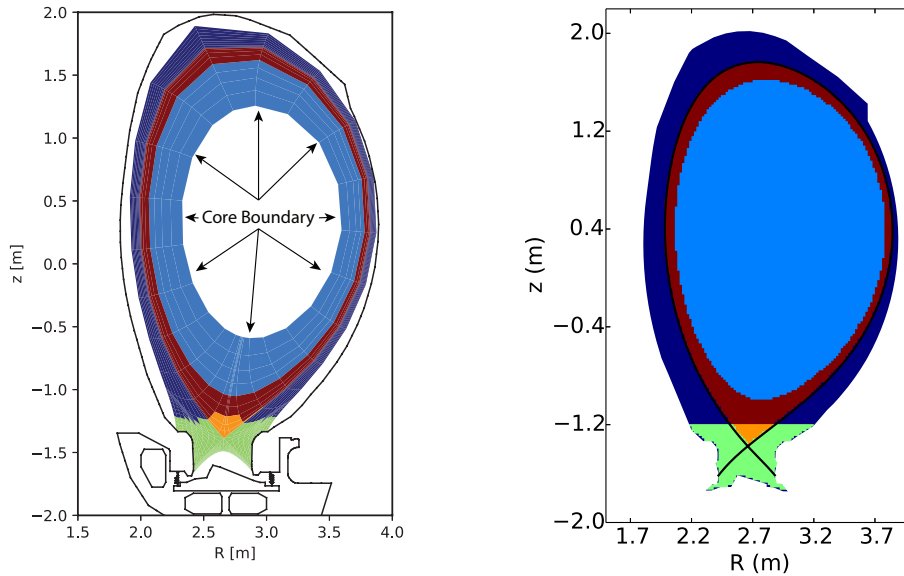


Figure 6.1: Radiation power density in an enlarged view of the divertor area for an unseeded (left) and a neon-seeded SOLPS-ITER case (right; $n_{\text{Ne}10+, \text{core}} = 7.0 \times 10^{17} \text{ m}^{-3}$). In the unseeded case the radiation is concentrated in the divertor area, in particular close to the targets. With neon the radiation extends to a ring along the separatrix.

The development of the poloidal radiation distribution was analysed for the set of SOLPS-ITER simulations at varying neon core densities in Fig. 6.3, also in order to allow comparisons to Fig. 5.27. Therefore, the definitions of the poloidal regions were chosen as close to those in Fig. 5.27 as possible, but some discrepancies remain (see Fig. 6.2). It should also be noted that Fig. 5.27 contains data points with varying heating powers, whereas in Fig. 6.3 the heating power was constant. To distinguish the simulated quantities from their experimental counterparts, “sim” or “exp” are added to their indices within this chapter accordingly.



Region	Simulation	Experiment
Core (light blue)	from 6th cell inside separatrix up to the core boundary	$\rho_{\text{pol}} < 0.95$ and $z > z_{\text{X-point}}$
Edge/Ped. (red)	from separatrix up to 5th cell towards the core boundary	$0.95 < \rho_{\text{pol}} < 1.00$ and $z > z_{\text{X-point}}$
Divertor (green)	$(-1.20 \text{ m} > z > z_{\text{X-point}}$ and $\rho_{\text{pol}} > 1)$ or $z < z_{\text{X-point}}$	$(-1.20 \text{ m} > z > z_{\text{X-point}}$ and $\rho_{\text{pol}} > 1)$ or $z < z_{\text{X-point}}$
X-point (orange)	from separatrix up to 5th cell and $z < -1.20 \text{ m}$	$0.95 < \rho_{\text{pol}} < 1.00$ and $z > z_{\text{X-point}}$
SOL (dark blue)	$z > -1.20 \text{ m}$ and $\rho_{\text{pol}} > 1.00$	$z > -1.20 \text{ m}$ and $\rho_{\text{pol}} > 1.00$

Figure 6.2: Poloidal regions in SOLPS-ITER simulations (top left) and experiment (top right) and their definitions (table, bottom). The coordinates z and ρ_{pol} refer to the centre points of the cells in the simulation grid and in the (experimental) bolometric reconstruction. For this reason, for the simulation regions the cut-off at $z = -1.20 \text{ m}$ is not perfectly horizontal. Note that, by above definitions, the pedestal region also includes the X-point region. The simulation domain contains only the part of the core region with $\rho_{\text{pol}} > 0.69$. The definitions of the SOL are mentioned here for the sake of completeness, but are not used in any analysis in this thesis.

As shown in Fig. 6.3, the total radiation power $P_{\text{rad,tot,sim}}$ is increasing from around 1 MW up to a maximum value of 8.5 MW for the highest stable simulation, corresponding to $f_{\text{rad,sim}} = 0.43$. For a high radiation simulation this is a quite low power fraction. Since the numerical grid of the simulations does only include core areas with $\rho_{\text{pol}} > 0.69$, the radiation power from inside this position (the south or core boundary) is not considered in the simulations. The core radiation is therefore actually higher than indicated. The same is true for the actual heating power which must be higher than the heating power at the south boundary in order to compensate for the additional radiation power from inside the south boundary. This might also lead to a higher radiative power fraction. The size of this effect, namely the radiation power inside the south boundary $P_{\text{rad,SB,sim}}$, can be estimated from $P_{\text{rad,core,exp}}$ (depicted in Fig. 5.27), even though

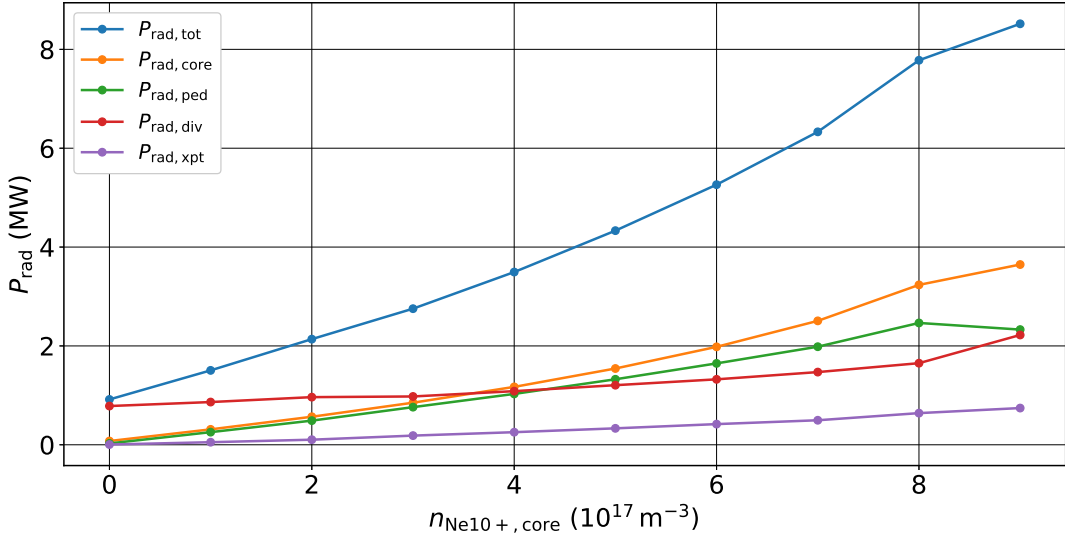


Figure 6.3: Radiation powers from different regions (see definitions in Fig. 6.2) as function of neon core density in a $P_{\text{heat}} = 20 \text{ MW}$, $n_{\text{D}+, \text{core}} = 1 \times 10^{20} \text{ m}^{-3}$ SOLPS-ITER simulation series. The neon seeding leads to an increase of the total radiated power by increasing primarily the core and pedestal radiation. The divertor radiation power remains on a low level. The low radiation power from the X-point region indicates the absence of an X-point radiator.

these values come with a margin of uncertainty. It is assumed that at $Z_{\text{eff,max,sim}} \approx Z_{\text{eff,max,exp}}$ in the highest seeded cases also the total core radiation power fulfils

$$P_{\text{rad,core,sim}} + P_{\text{rad,SB,sim}} \approx P_{\text{rad,core,exp}}. \quad (6.1)$$

With the known values of $P_{\text{rad,core,sim}} = 3.6 \text{ MW}$ (see Fig. 6.3) and $P_{\text{rad,core,exp}} = 6\text{--}8 \text{ MW}$ (see Fig. 5.27) this results in a radiation power inside the core boundary of $P_{\text{rad,SB,sim}} = 2.4\text{--}4.4 \text{ MW}$. Taking into account the radiation from inside the core boundary, the radiative power fraction of the highest seeded simulation

$$f_{\text{rad,sim}} = \frac{P_{\text{rad,tot,sim}}}{P_{\text{heat,sim}}} = \frac{8.6 \text{ MW}}{20.0 \text{ MW}} = 0.43 \quad (6.2)$$

would increase to

$$f_{\text{rad,sim,corr}} = \frac{P_{\text{rad,tot,sim}} + P_{\text{rad,SB,sim}}}{P_{\text{heat,sim}} + P_{\text{rad,SB,sim}}} = \frac{8.6 \text{ MW} + \{2.4 \text{ MW} - 4.4 \text{ MW}\}}{20.0 \text{ MW} + \{2.4 \text{ MW} - 4.4 \text{ MW}\}} = 0.49\text{--}0.53. \quad (6.3)$$

This demonstrates that the neglected radiation from inside the core boundary is partly, but not fully, responsible for the low value of $f_{\text{rad,sim}}$ (compared to $f_{\text{rad,exp,max}} = 0.66$).

In the unseeded SOLPS-ITER case, the divertor radiation constitutes nearly all of the total radiation power of 1 MW (see Fig. 6.3). For higher seeding levels the divertor radiation doesn't

increase as strongly as the radiation from the core or the edge, and assumes only a value of $P_{\text{rad,div,sim}} = 2.2 \text{ MW}$ in the highest seeded case. The core and pedestal radiation instead are quasi-negligible in the unseeded case and increase up to $P_{\text{rad,core,sim}} = 3.6 \text{ MW}$ and $P_{\text{rad,ped,sim}} = 2.3 \text{ MW}$. This demonstrates that neon in fact radiates primarily in the core and in the pedestal, and less in the divertor. A part of the pedestal radiation comprises the radiation from the X-point, which also increased, but with its $P_{\text{rad,xpt,sim}} = 0.7 \text{ MW}$ in the highest seeded case it only contributes a minor fraction to the overall radiation power (compared to 40% of the total radiation power found in experiments [140]), confirming that an X-point radiator is not present so far.

Simulations with slightly higher neon content (up to $n_{\text{Ne}10+, \text{core}} = 9.5 \times 10^{17} \text{ m}^{-3}$) have been performed but have not converged. In these cases the zone with the highest radiation power density propagates along the inner divertor leg towards the X-point and an X-point radiator is actually formed in the simulation with the highest neon seeding, resulting in (compare to Fig. 6.3) a higher $P_{\text{rad,core,sim}} = 5.3 \text{ MW}$, a decreasing $P_{\text{rad,div,sim}} < 2 \text{ MW}$ and an increase in the total radiation of $P_{\text{rad,tot,sim}} \approx 11 \text{ MW}$ (with a corresponding $f_{\text{rad,sim,nc}} = 0.55$). These results have to be taken with caution since the underlying cases are not converged, but they can give an indication where numerically more stable simulations might head.

6.3 Detachment and Pressure Loss

Impurities are seeded to reduce target temperature and particle fluxes by increasing the radiation power. Since neon radiates primarily in the core and pedestal region, it is expected to have an impact on the radial temperature and density distribution. In the experiment it was suspected that the pressure loss from inside the separatrix might be a cause for the detachment of the targets.

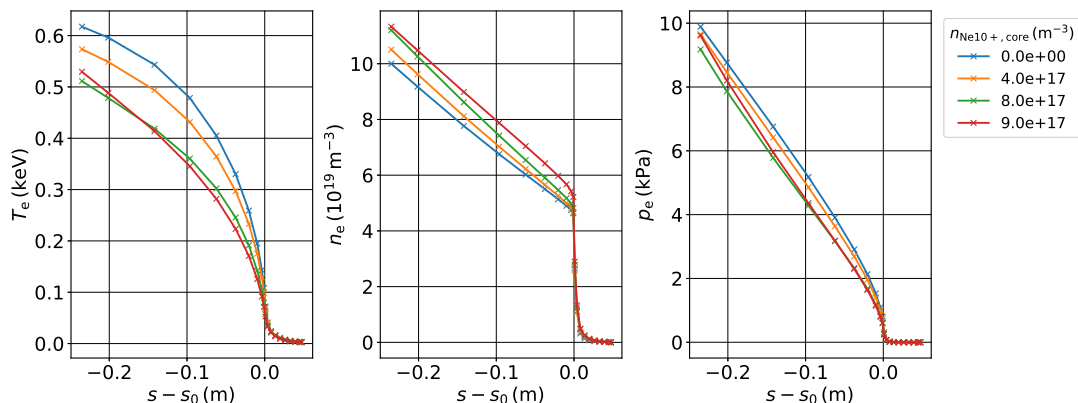


Figure 6.4: Profiles of electron temperature, density, and pressure at the outer midplane as function of neon core density in a $P_{\text{heat}} = 20 \text{ MW}$, $n_{\text{D}+, \text{core}} = 1 \times 10^{20} \text{ m}^{-3}$ SOLPS-ITER simulation series. The pressure drop is attributed to the decrease of temperature over the whole profile due to radiation. The density is slightly increased due to neon.

In Fig. 6.4 the radial profiles for electron temperature, density and pressure are shown. In cases with $n_{\text{Ne}10+, \text{core}} \leq 8.0 \times 10^{17} \text{ m}^{-3}$ the electron density increases by up to 10% in both, the

core and consequently also in the pedestal area, which can be attributed to the introduction of neon at the core boundary: as neon is introduced as Ne^{10+} , the quasi-neutrality of the plasma leads to an increased electron density. The deuterium core density was not varied in this set of simulations and has therefore no impact on the electron density. In the case with the highest neon seeding level $n_{\text{Ne}^{10+},\text{core}} = 9.0 \times 10^{17} \text{ m}^{-3}$ the pedestal electron density is increased by about 20% compared to the lower seeded cases. A corresponding increase of the core density cannot be observed in this case, indicating that the increase in the pedestal is due to sources outside the separatrix, such as the ionisation sources observed outside the high field side separatrix in Fig. 6.6. The electron temperature is decreasing for $n_{\text{Ne}^{10+},\text{core}} \leq 8.0 \times 10^{17} \text{ m}^{-3}$ over the whole radial profile. For the case with $n_{\text{Ne}^{10+},\text{core}} = 9.0 \times 10^{17} \text{ m}^{-3}$ the core temperature does not follow this trend, while the pedestal temperature continues to decrease. From Fig. 6.3 a decrease of radiation power in the core can be excluded as cause for this increase.

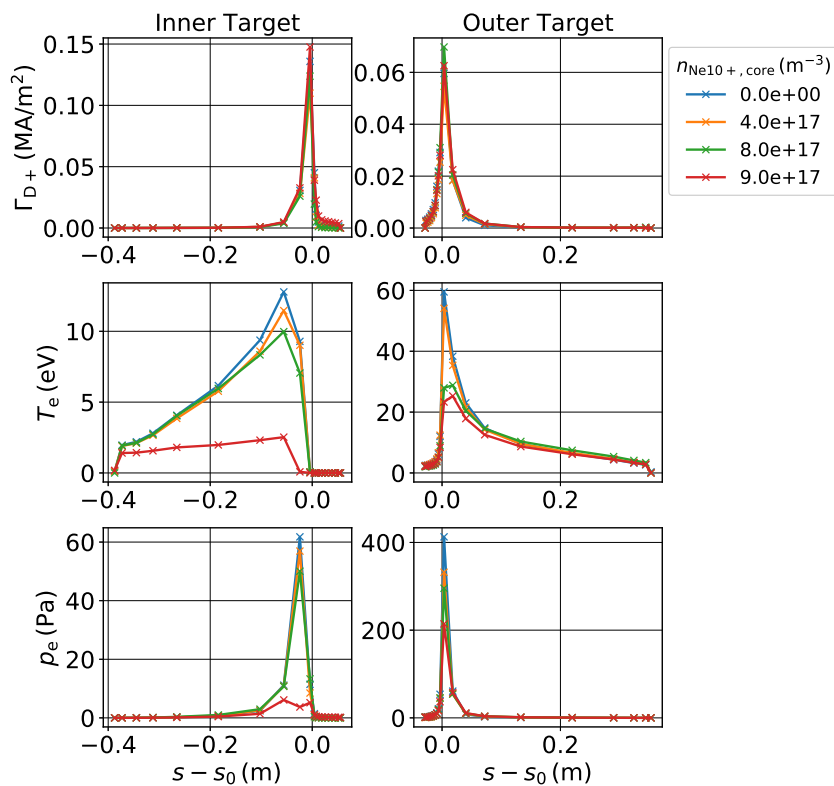


Figure 6.5: Profiles of poloidal deuterium ion flux Γ_{D+} , electron temperature, and static electron pressure for inner (left) and outer (right) target as function of neon core density in a $P_{\text{heat}} = 20 \text{ MW}$, $n_{D+, \text{core}} = 1 \times 10^{20} \text{ m}^{-3}$ SOLPS-ITER simulation series (for better visibility only selected simulations from the series are shown). The neon leads to a cooling of the outer target, but not to detachment. The inner target reaches detachment with the highest neon seeding level. On both targets, a pressure drop is observed, which is more pronounced at the inner target.

In the outer midplane profiles a drop in pedestal pressure can be observed with increased neon core density, which might also impact the targets. However, the inner and the outer target can behave differently (see subsection 4.4.1). Figure 6.5 shows profiles of the poloidal deuterium ion flux Γ_{D+} , the target temperature T_e and the static electron pressure p_e at the inner and the outer target. At the inner target the temperature is already relatively low in the unseeded case (12 eV)

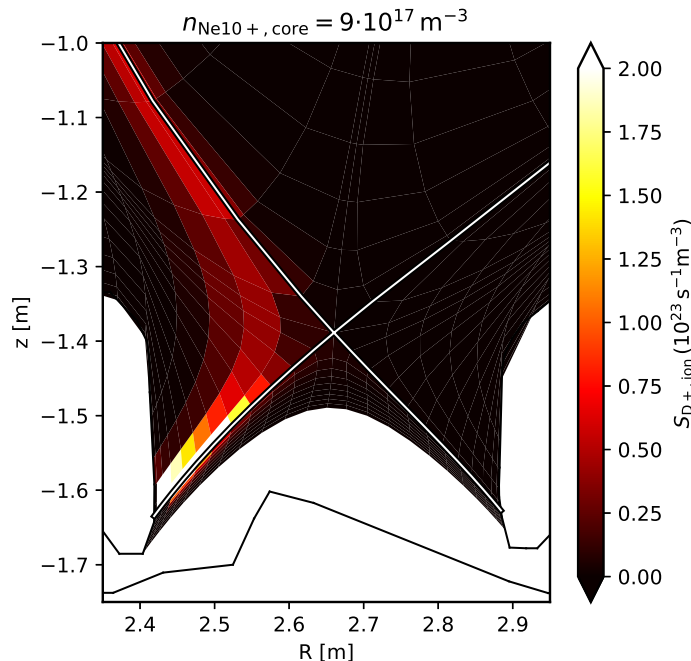


Figure 6.6: Deuterium ionisation rate in a $P_{\text{heat}} = 20 \text{ MW}$, $n_{\text{D}^+, \text{core}} = 1 \times 10^{20} \text{ m}^{-3}$, $n_{\text{Ne}10^+, \text{core}} = 9 \times 10^{17} \text{ m}^{-3}$ SOLPS-ITER simulation. Only very low ionisation sources are present in the outer divertor, suggesting a low recycling regime. Along the inner divertor leg, in vicinity to the inner target, ionisation is strongest. While the sources in the SOL above the X-point are only observed in this intensity at the highest neon seeding level (shown here), the sources along the divertor leg are present for all examined neon seeding levels, indicating a high recycling regime.

and decreases only slightly with increasing neon core density. For neon core densities below $n_{\text{Ne}10^+, \text{core}} = 9.0 \times 10^{17} \text{ m}^{-3}$ the inner divertor is in the high recycling regime. This is indicated by the temperature drop between the outer midplane and the target ($T_{e,t}/T_{e,\text{OMP}} \approx 0.2\text{--}0.25$) and the presence of deuterium ionisation sources which are located along the inner divertor leg outside the separatrix (see Fig. 6.6) for all examined neon seeding levels. For the highest neon core density of $n_{\text{Ne}10^+, \text{core}} = 9.0 \times 10^{17} \text{ m}^{-3}$ the temperature drops drastically to $T_{e,t} = 2 \text{ eV}$ and is thus reaching a temperature regime where ionisation is reduced and recombination starts to become more effective. In this highest seeded case recombination is observed in the first target cell outside the separatrix. Due to the limitation of the target temperatures to 2 eV in the simulation settings it cannot be determined if a further temperature decrease could be achieved.

At the outer target a reduction in temperature can be observed as well, though, only from 60 eV to 25 eV. This is far above the values at the inner target, similar to the in-out asymmetry observed in the experiment, even though drift effects are not considered in the simulations treated here. In the simulations the outer divertor seems to be in the low recycling regime: the temperature drop along the SOL is slightly increasing with more neon (the ratio $T_{e,t}/T_{e,\text{OMP}} \approx 0.95\text{--}0.75$ is decreasing) but still barely existent. Despite the higher temperatures in the outer divertor, ionisation sources are not present in the outer divertor (see Fig. 6.6), which implies that recycled neutrals from the outer divertor are re-ionised somewhere else. This might be attributed to the electron and (deuterium) ion density being lower in the outer than in the inner

divertor. In the outer divertor the heat fluxes are not only significantly higher but can also reach the target nearly unhindered. The lack of energy and momentum sinks in the outer divertor is related to the high temperatures (and low neutral densities, see section 6.4). It was shown (e.g. in [277]) that the loss of pressure in front of a target is most effective at temperatures below 5 eV, which the outer target does not reach by far.

It has to be noted that, due to setting the transport coefficients spatially constant, the particle and heat fluxes into the divertor parts are generally not symmetric due to the compression of the magnetic field lines at the low field side (Shafranov shift) and the different connection lengths from the low field side to the inner and the outer divertor. In Fig. 6.5 the deuterium ion fluxes to both targets show a minor increase (with a lower flux at the outer target), including a small drop at the outer target for the highest neon seeding level. They might arise from increased upstream ionisation, especially at the high field side, as shown in Fig. 6.6.

The low temperatures at the inner target for $n_{\text{Ne}10+, \text{core}} = 9.0 \times 10^{17} \text{ m}^{-3}$ suggest that the inner target is detached in this case. This could be confirmed by the observation of a pressure drop between the midplane and the inner target. In Fig. 6.5 a strong decrease of pressure at the inner target can be seen (as well as a reduction of pressure at the outer target). The midplane profiles in Fig. 6.4 show that with increased neon seeding the static electron pressure is decreased, in the core as well as at the pedestal. This pressure drop originates from a temperature drop along the whole radial profile, from the core to the pedestal, and is probably related to the increased core radiation.

As it is crucial whether the pressure drop observed at the inner target originates from a pressure drop at the upstream position (and hence in the core) or from within the SOL, the origin of the pressure drop is analysed in Fig. 6.7: the figure shows the total pressure (i.e. including static and dynamic pressure of electrons and ions)

$$p_{\text{tot}} = p_{e, \text{stat}} + p_{i, \text{stat}} + p_{e, \text{dyn}} + p_{i, \text{dyn}} \quad (6.4)$$

along the first row of cells outside the separatrix. Between inner midplane and X-point position the total pressure drops by around 25%. This pressure drop is highest at low neon seeding rates and is barely existent at the highest neon seeding stage, as in this case more pressure is lost inside the separatrix and thus the midplane SOL pressure is lower. The decreasing total pressure in the main chamber SOL (between inner and outer midplane positions) indicates an impact of the increased neon content and hence increased core radiation. Compared to the pressure loss at the high field side, the loss between the outer midplane and the outer target is by far not as strong. Since this pressure loss is not increasing further towards the targets, it seems that the neon seeding does not add significant additional SOL pressure loss. The major part of the pressure loss towards the inner target, however, occurs in front of the target, for all neon seeding stages. For $n_{\text{Ne}10+, \text{core}} = 9.0 \times 10^{17} \text{ m}^{-3}$, though, nearly all pressure is lost. With these strong losses also taking place close to the inner target, it appears that the upstream pressure losses are not the main cause for the pressure loss between midplane and target but rather volumetric processes in the divertor. The strong pressure loss in the SOL is a clear indicator for a detached inner target. In contrast, the decrease of pressure at the outer target with increased neon seeding has its origin primarily in the decreased pedestal/core pressure.

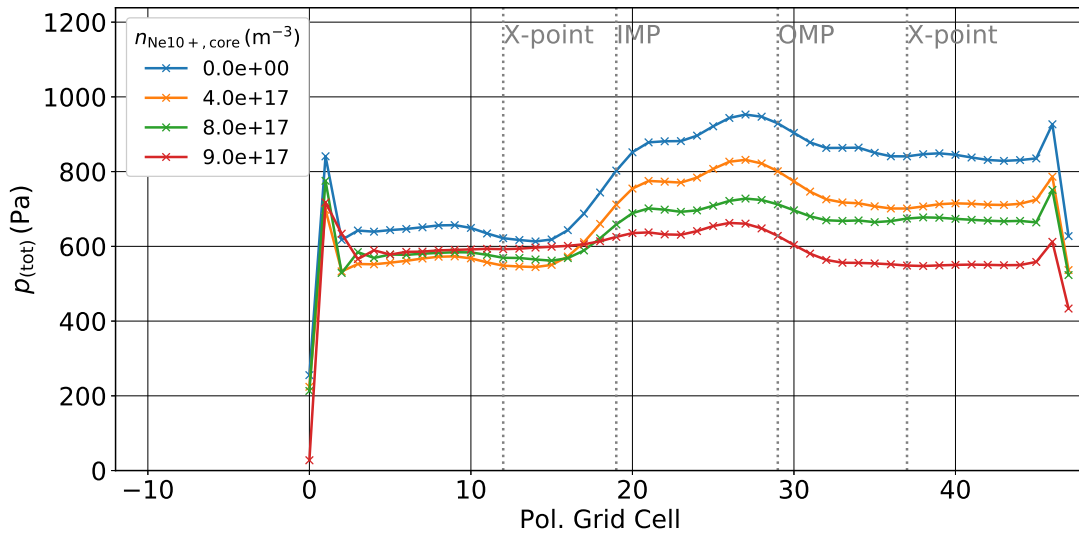


Figure 6.7: Total (static and dynamic, electrons and ions; see Eq. 6.4) pressure along the first poloidal row of cells outside the separatrix in a $P_{\text{heat}} = 20 \text{ MW}$, $n_{D+, \text{core}} = 1 \times 10^{20} \text{ m}^{-3}$ SOLPS-ITER simulation series for different neon core densities. The pressure at the inner target (left) is much lower than at the outer target (right). While the neon seeding causes a decrease of pressure on the way between the outer midplane position and the outer, the pressure in the inner divertor increases (but decreases at the target).

The origin of the pressure drop towards the inner target also becomes clear from Fig. 6.8. In this figure the total pressure of some exemplary cells of the simulation grid is shown, as function of the neon core density and normalised to their respective values in the unseeded case. For most of the seeding levels the pressure decreases uniformly. It can be observed that the losses in the core are slightly lower than those in the pedestal and in the SOL. The losses at the targets are mostly similar to those in the other regions. At the highest neon seeding level the pressure at the inner target drops to low values, indicating detachment. The fact that the other pressures remain rather high imply that this pressure drop actually originates from the divertor rather than from the upstream SOL or pedestal.

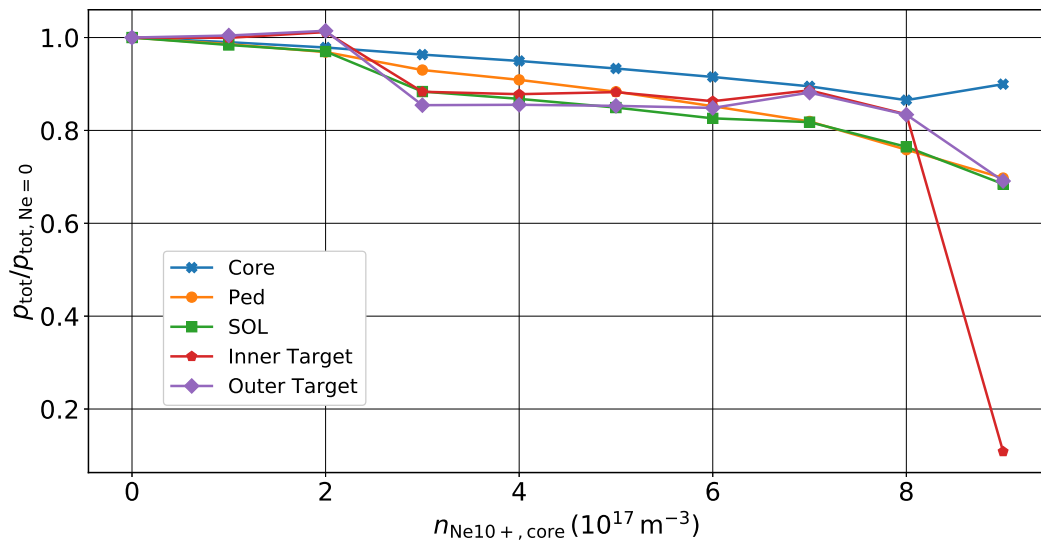


Figure 6.8: Drop of total pressure in some grid cells, as function of neon core density and normalised to their values in the unseeded case, in a $P_{\text{heat}} = 20 \text{ MW}$, $n_{\text{D}+, \text{core}} = 1 \times 10^{20} \text{ m}^{-3}$ SOLPS-ITER simulation series. The normalised values are depicted for: core (first cell at the core boundary, midplane), pedestal (first cell inside the separatrix, midplane), SOL (first cell outside the separatrix, midplane), and the inner and outer target (first cell outside the separatrix). The pressure losses by neon seeding are quite uniformly, only at the highest seeding level the inner target detaches.

6.4 Deuterium and Impurity Distribution

For a better understanding of the phenomena described above, it is crucial to examine the distribution of fuel and impurity ions and neutrals. As shown in Fig. 6.6, deuterium is primarily ionised in the inner divertor while in the outer divertor no considerable ionisation can be observed, implying that the ionisation takes place somewhere else and that neutrals can escape the outer divertor. A comparison between the simulated fluxes towards the wall and the particle fluxes onto the targets measured in the experiment by Langmuir probes (as a proxy for recycling fluxes) shows that this lack of divertor neutral density might be an issue also in the simulations presented in this chapter: While the external deuterium sources were in the same order of magnitude for experiment and the highest seeded simulation ($\Gamma_{\text{D}, \text{puff}, \text{exp}} \leq 5 \times 10^{22} \text{ es}^{-1}$, $\Gamma_{\text{D}, \text{core}, \text{sim}} \approx 3.5 \times 10^{22} \text{ es}^{-1}$), the experimental particle fluxes ($\Gamma_{\text{wall}, \text{exp}} \approx 1 \times 10^{25} - 2 \times 10^{25} \text{ es}^{-1}$) were much higher than those from the simulations ($\Gamma_{\text{wall}, \text{sim}} \approx 5 \times 10^{23} \text{ es}^{-1}$). This is a strong indicator that in fact the low neutral density in the divertor might be the reason for the low divertor and X-point radiation power as well as the absence of charge exchange interaction and ionisation in the outer divertor. Attempts to increase the divertor neutral density and hence the radiation power by reducing the pump albedo or by injecting additional deuterium into the divertor failed, as the simulations became unstable already at low increases of the density in the divertor. The approach taken in these simulations to control the density not by neutral particle injections into the divertor but through the core boundary is justified by these results. As a further possible way to increase the density in the divertor, the transport parameter D_{\perp} was increased in the far SOL from $0.5 \text{ m}^2/\text{s}$ (see Fig. 3.5) up to $10 \text{ m}^2/\text{s}$, without considerable impact, though.

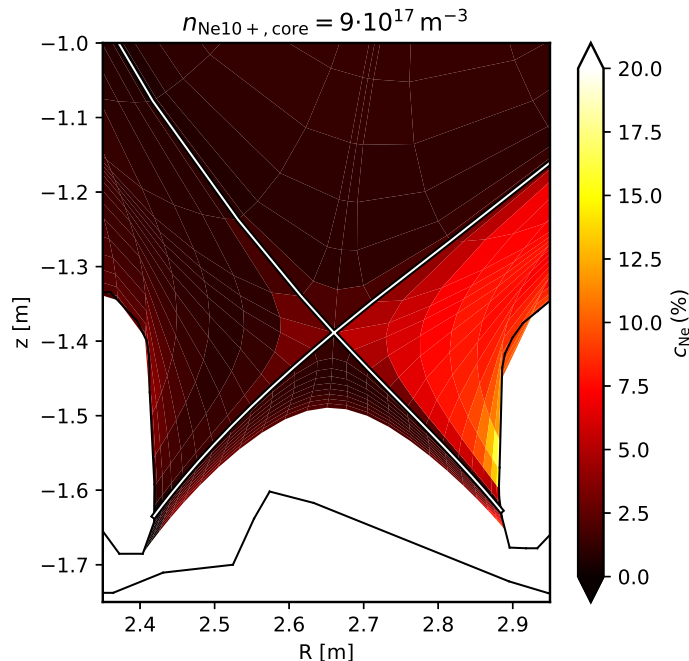


Figure 6.9: Neon concentration $c_{\text{Ne}} = n_{\text{Ne}}/n_e$ in a $P_{\text{heat}} = 20$ MW, $n_{\text{D}^+, \text{core}} = 1 \times 10^{20} \text{ m}^{-3}$, $n_{\text{Ne}^{10+}, \text{core}} = 9 \times 10^{17} \text{ m}^{-3}$ SOLPS-ITER simulation. The neon is clearly concentrated in the outer divertor area.

In the present simulations the neon core density was ramped up until the simulations became numerically unstable. In the highest seeded case, Z_{eff} reached a medium value along the radial profile at the outer midplane (in analogy to the experimental determination) of 3.0–3.5, and therefore in a similar range as highly seeded experimental discharges. However, the impurities in the simulation are not poloidally equally distributed (as assumed for the experimental examinations performed in sections 5.3.1 and 5.4) but are strongly located in the low field side SOL and in the outer divertor (see Fig. 6.9 where the neon concentration is shown). It is notable that despite much higher neon concentrations in the divertor $P_{\text{rad,div}}$ does not increase stronger and instead the neon has a much higher impact on the core radiation. This effect might be caused by the low recycling fluxes and the low divertor neutral densities. In fact, the neon species $\text{Ne}^{7+} - \text{Ne}^{9+}$ contribute most to the total radiation. The highest abundances of these species were observed inside the separatrix, especially in the pedestal, at the X-point, and (Ne^{9+}) in the core region. Ne^{10+} contributes few radiation power as it is only present close to the core boundary. The contribution of deuterium is nearly unchanged by the neon seeding.

Recently, the issue of impurity transport and divertor retention in SOLPS simulations was treated in [155, 156] (and references therein). Impurities are kept in the divertor if their ionisation happens downstream of the impurity stagnation point, i.e. the point below which impurities flow into the divertor. The position of this impurity stagnation point is determined by two major forces: the friction force of impurities with the main plasma ions $F_{\text{fr}} \propto Z^2 (u_{\text{D}^+} - u_{\text{NeZ}^+})$ and the thermal force $F_{\text{th}} \propto Z^2 \nabla T$, which balance at the stagnation point. This stagnation point is not necessarily similar for neighbouring flux surfaces, also reversal flows are possible when impurities are transported towards the target on flux surfaces in the far SOL and moved

upstream in the near SOL. This is also the case at the inner target in the simulations treated here. On the first flux surface the neon stagnation point is located below the point with the highest ionisation. For the second flux surface the stagnation point is located above the point of the highest ionisation, hence causing neon transport back to the target. A similar picture is found in the third flux surface. At the outer target, however, the situation is different: since no major ionisation sources are located in the outer divertor, neither for deuterium nor for neon, the neon stagnation point cannot be found close to the divertor. Therefore, the criterion introduced above does not apply. Since the outer divertor is in the low recycling regime, a temperature gradient is not present and the friction force can dominate the impurity transport, leading to a flushing of neon into the divertor with the main ions. There is no sign for a flow inversion (as described in [155]) since at no point the deuterium ionisation in the outer divertor exceeds the ionisation in the inner divertor. The high neon concentration at the LFS might be a reason for the comparably low $P_{\text{rad,tot}}$ at relatively high Z_{eff} values at the outer midplane. As pointed out in [278], the ionisation and recombination rates might also play a role in underestimated radiation powers. So far, for neon only ionisation and recombination are contained in the ADAS database, neglecting the effect of neon charge exchange reactions. It was shown in [278] that corrected reaction rates led to higher ionisation of neon in the pedestal of ASDEX Upgrade, leading to higher neon densities and higher radiation power.

Seed impurities cannot only increase the radiation power and decrease the target temperatures and particle fluxes but can also influence the core and hence the fusion performance of future reactors. In [128, 129] a possible compromise between a high divertor radiation (high neon concentration c_{Ne}) and a low impact on the core plasma (low c_{Ne}) was examined using SOLPS simulations of ITER. Neon is going to radiate in the divertor and at the separatrix. The upstream electron density $n_{e,\text{sep}}$ was used as proxy for the core density and therefore the fusion power. For the neon concentration at the separatrix (taken as the mean value over the first SOL flux surface ring above the X-point) the proportionality $\langle c_{\text{Ne}} \rangle_{\text{sep}} \propto n_{e,\text{sep}}^{-\alpha}$ was found, with α ranging between 4 for low divertor radiation powers and 2 for highest radiation powers. From simple models like the Lengyel model [125] an exponent of $\alpha = 2$ was expected. In the same study, independently of $P_{\text{rad,div}}$ the relation $\langle c_{\text{Ne}} \rangle_{\text{div}} \propto n_{e,\text{sep}}^{2.8}$ was found for the neon concentration along the first SOL flux surface at the outer divertor leg [129]. The impact of neon seeding on the separatrix density is even more of importance for the cases treated in this thesis due to the radiation from inside the separatrix. A comparable analysis as in [128, 129] was therefore also performed for the series of SOLPS-ITER simulations with varying P_{heat} , $n_{\text{D}^+, \text{core}}$, and $n_{\text{Ne}^{10+}, \text{core}}$ (see introduction of this chapter). The simulations in this second series were based on the first series with varying neon core density. In the following, first their density was decreased and then the heating power varied. To avoid the risk that the transition to a solution with a detached inner target in the first series at $n_{\text{Ne}^{10+}, \text{core}} = 9 \times 10^{17} \text{ m}^{-3}$ might be present also in simulations of the second series where it weren't in a usual neon ramp-up series, only solutions with $n_{\text{Ne}^{10+}, \text{core}} \leq 8 \times 10^{17} \text{ m}^{-3}$ were considered.

Figure 6.10 shows the mean neon concentration of the first row of cells outside the main chamber separatrix for simulations of the second series. Similar to [128, 129] it was examined if the exponent α of the fit was varied with $P_{\text{rad,div}}$. The converged simulation cases were therefore grouped in classes of different divertor radiation powers with class sizes of 0.1 MW (see legend of Fig. 6.10). Classes that contained less than 8 data points were omitted in order to allow

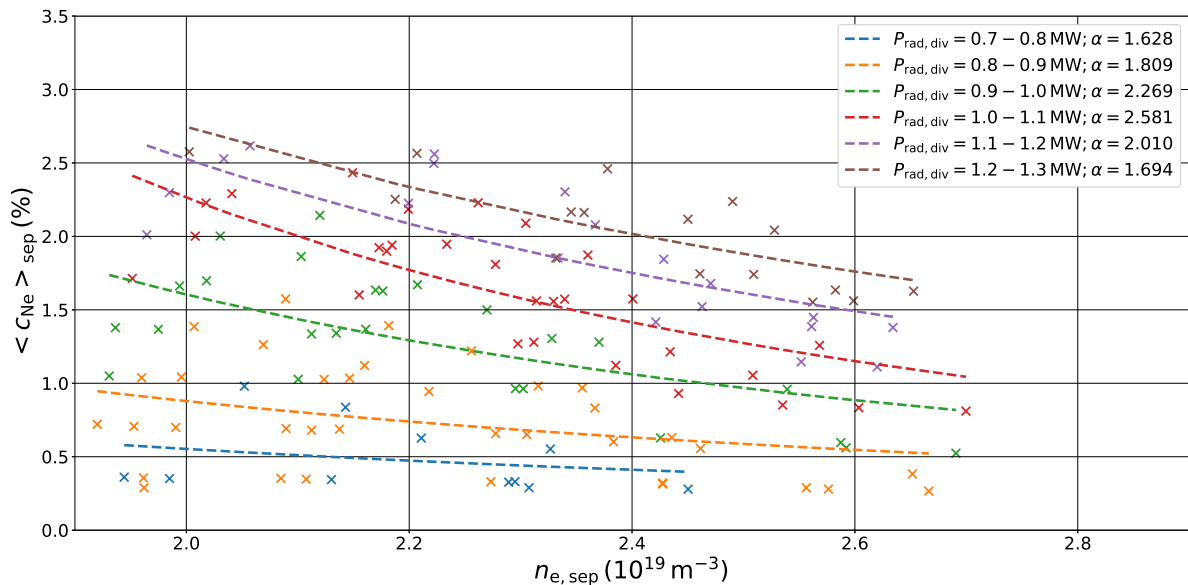


Figure 6.10: Mean separatrix neon density $\langle c_{Ne} \rangle_{sep}$ (mean value over the first row of cells outside the separatrix above the X-point) as function of the separatrix electron density $n_{e,sep}$ with fit functions of the form $\langle c_{Ne} \rangle_{sep} \propto n_{e,sep}^{-\alpha}$. $\alpha \approx 2$, which in [128, 129] was found for highest divertor radiation powers.

meaningful interpolations. The fit parameter α displays some variation in the range 1.6–2.6. In [128, 129] $\alpha \approx 2$ was only found for the simulations with the highest divertor radiation power and the strongest detachment. For lower divertor radiation powers α decreases to about 4. Since in the simulations shown in this thesis $\alpha \approx 2$ rather than $\alpha \approx 4$ it is concluded that the divertor radiation power of these simulations is already at a maximum achievable with neon seeding. This is in line with slow increase of $P_{rad,div}$ in Fig. 6.3 and with the fact that in ITER neon is a divertor radiator while in JET it is a SOL and pedestal radiator. Apart from other obvious differences between the two analyses, it has to be considered, though, that in the original ITER analysis the separatrix density varied in the range of 3×10^{19} – $6 \times 10^{19} \text{ m}^{-3}$ (fuelled by puffs into the divertor) and therefore over a much larger density range as in the analysis presented here.

6.5 Summary and Discussion

In the SOLPS-ITER simulation series shown in this chapter, neon’s suitability as a core and edge radiator was demonstrated in JET, although with some restrictions. The neon content in the simulations was limited by numerical instabilities and asymmetries caused by the neon seeding. Neon led to a growing core and edge radiation power and at the same time a divertor radiation that was stable on a low level. This is in accordance with the experimental observations. The radiation power density near the X-point was increased, but is still lower than in the region close to the targets. The fact that in simulation cases with higher neon seeding, which were not converged, a pronounced X-point-radiator was found shows that the physics related to the formation of an X-point radiator is in general included in the simulation model, but its stability may not. While the inner target reached detachment, the outer target was still in the low-recycling regime. The only weakly pronounced X-point radiator and the pedestal pressure loss

which is not high enough to be responsible for the detachment of the inner target suggest that under the conditions given in the simulations a correlation between these phenomena, as observed in the experiment, cannot be assumed. It can't be excluded, though, that at higher neon seeding rates such a correlation might be found. It is, hence, crucial to discuss possible reasons for the limited neon seeding rates in the simulations. The low divertor radiation and the attached outer target might be attributed to the low density in the divertor: the radiation power depends on n_e (see Eq. 2.12) and with reduced radiation and reduced ion-neutral interaction (due to the lack of ions and neutrals) two main drivers of detachment are not as strong as expected. Such a lack of density in the divertor was reported also from previous EDGE2D-EIRENE simulations of JET (e.g. [162, 279–282]) as well as from SOLPS simulations of ASDEX Upgrade [283, ch. 5.6.1]. The low recycling fluxes in the SOLPS-ITER simulations presented in this thesis indicate that they are also due to a low density in the divertor. Attempts to overcome this issue by a reduction of the pump albedo, an additional puff of neutral particles into the divertor, or an adaptation of the far SOL transport parameter were not successful in significantly increasing the density in the divertor. The simulations might behave differently if they were not fuelled via the core, like all simulations treated here, but through neutral puffs into the divertor, where retention effects might come into play.

The strongly asymmetric density distribution in the divertor might hinder the outer target from assuming a more favourable state than the low recycling regime. One possible way to overcome these asymmetries is the activation of drifts in SOLPS-ITER. Since cases with activated drift terms tend to be numerically challenging and hence unstable, this effort is often omitted, also in this thesis. They can, however, have great impact on the solution. In previous works they were shown to be crucial in order to reproduce experimentally measured profiles [152, 153, 237, 284]. They can contribute to increasing pressure losses and radiation in the outer divertor [283, ch. 5.9]. In particular, they are crucial for a correct modelling of the impurity fluxes into and out of the divertor (divertor retention) [156, 160]. The asymmetry between the power fluxes on inner and outer targets is enhanced when drifts are activated [237]. In SOLPS5.0 simulations of nitrogen-seeded ASDEX Upgrade plasmas [153], the activation of drift effects allowed to numerically reproduce the high field side high density region and hence to increase the divertor neutral density and the radiation power to experimentally observed levels. Drifts were also shown to stabilize the X-point radiator in SOLPS-ITER simulations of nitrogen seeding in ASDEX Upgrade [160], with both targets being in full detachment. All the above-mentioned works in simulation, especially [153, 160], suggest that the activation of drifts might definitely have an impact on the results of the simulations presented in this thesis and a better agreement with the experiment. This impact cannot be estimated quantitatively, though, as it can vary depending on many parameters such as machine size and respective magnetic field [158, 159].

The simulations successfully demonstrated the main radiation distribution features, namely the increase of core and pedestal radiation while the divertor radiation remained low, as well as the detachment of the inner target. An early stage of an X-point radiator was found. The drop of the pedestal pressure with neon seeding was not found to be the cause for the detachment of the inner divertor in the simulations. Finding ways to increase the density in the divertor as well as to reduce the divertor asymmetry could further improve the suitability of the simulations for studying the relation between the formation of the X-point radiator, the decrease of pedestal pressure and the detachment of the divertor, as observed in the experiment.

7 Conclusion

In order to protect the inner wall and the divertor targets of future fusion reactors like DEMO, a high power dissipation by radiation is required, especially from the plasma edge. To this end, impurities such as neon, nitrogen or argon are injected, or “seeded”, into the plasma. As this includes the risk of restricting or disabling the fusion processes in the core by diluting the D-T fuel with impurities, adequate plasma scenarios have to be developed and examined in advance in smaller experiments. With the analysis of experiments and numerical simulations of neon-seeded JET discharges, this thesis aimed to contribute to these efforts.

In the analysis of neon-seeded experiments in the currently largest tokamak JET, phases of a high confinement mode without the typical characteristic instabilities (M-mode) were observed. These M-mode phases were found at high heating powers and high neon seeding rates, and in proximity to the transition into the low confinement mode. During such M-mode phases the strong concentration of the radiation at the magnetic X-point, within the separatrix, was accompanied by a decrease of the density at the steep pressure gradient region in the edge (pedestal) and a strong reduction of power and particle fluxes onto the target (detachment). The simultaneity of these phenomena suggested their correlation. Other properties of this regime, that can be considered favourable for future devices, like reduced influx of wall material and a density peaking in the core, were found. Although the energy confinement quality measured by $H_{98(y,2)}$ was comparably low due to the experiments’ general setup, it was not further decreased by the neon seeding. The properties just described make this M-mode regime promising in view of future fusion reactors and worth to be further examined.

To investigate the possible correlation between X-point radiator, pedestal pressure drop and detachment, numerical simulations with the SOLPS-ITER plasma boundary transport code were performed on the basis of the experiments. In these simulations the neon content that could be seeded into the plasma was limited due to numerical instabilities. The simulations were able to reproduce some key experimental features like an increase of core and edge radiation with increasing neon seeding or a detachment of the inner target at highest seeding rates. An X-point radiator, though, was only found in simulation cases which were not converged due to their high neon seeding. The pressure loss necessary for the detachment of the target primarily originated from a region close to the inner divertor target and quantitatively the pressure losses from inside the separatrix played only a minor role for the detachment of the inner target. Unlike in the experiment, the outer target was not in detachment. The overall low radiation powers as well as the outer target not being in detachment might be attributed to the low divertor neutral particle density as well as to asymmetries between inner and outer divertor. These limitations of the simulations could be solved by changing the location of the neon seeding and by activating drifts.

It was demonstrated that numerical simulations are generally capable of reproducing, at least partly, the key features of this M-mode regime which is potentially interesting for future fusion devices. Overcoming the current limitations in the simulations could possibly lead to simulations of higher neon seeding rates and to even better matches with the experimental findings. The numerical simulations can then be an important element to further explore this regime and to fill gaps which are inaccessible to the experiment. In further simulations with improved boundary conditions as well as in experimental analyses still to be done, the focus should be on the control of the M-mode regime, i.e. narrowing further down the prerequisites necessary to reach the regime or its key features in order to allow predictions for future fusion machines.

Bibliography

- [1] International Energy Agency. *Key World Energy Statistics 2019*. OECD, 2019. ISBN: 9789264847880. DOI: 10.1787/71b3ce84-en.
- [2] International Energy Agency. *World Energy Outlook 2019*. OECD, 2019. ISBN: 9789264973008. DOI: 10.1787/caf32f3b-en.
- [3] IPCC Core Writing Team. *Climate Change 2014: Synthesis Report. Contribution of Working Groups I, II and III to the Fifth Assessment Report of the Intergovernmental Panel on Climate Change*. Ed. by R. K. Pachauri and L. A. Meyer. Geneva, Switzerland: IPCC, 2014. ISBN: 9789291691432. URL: <https://www.ipcc.ch/report/ar5/syr/>.
- [4] B. P. Heard et al. “Burden of proof: A comprehensive review of the feasibility of 100% renewable-electricity systems”. In: *Renewable and Sustainable Energy Reviews* 76 (2017), pp. 1122–1133. DOI: 10.1016/j.rser.2017.03.114.
- [5] T. W. Brown et al. “Response to ‘Burden of proof: A comprehensive review of the feasibility of 100% renewable-electricity systems’”. In: *Renewable and Sustainable Energy Reviews* 92 (2018), pp. 834–847. DOI: 10.1016/j.rser.2018.04.113.
- [6] International Renewable Energy Agency. *Global Energy Transformation: A Roadmap to 2050 (2019 edition)*. Abu Dhabi: International Renewable Energy Agency, 2019. ISBN: 9789292600594. URL: <https://www.irena.org/publications/2019/Apr/Global-energy-transformation-A-roadmap-to-2050-2019Edition>.
- [7] International Atomic Energy Agency. *Fusion Physics*. Non-serial Publications. Vienna: International Atomic Energy Agency, 2012. ISBN: 978-92-0-130410-0. URL: <https://www.iaea.org/publications/8879/fusion-physics>.
- [8] A. S. Eddington. “The Internal Constitution of the Stars”. In: *The Scientific Monthly* 11.4 (1920), pp. 297–303. URL: <http://www.jstor.org/stable/6491>.
- [9] M. Salaris and S. Cassisi. *Evolution of Stars and Stellar Populations*. eng. Hoboken, NJ, USA: J. Wiley, 2005. ISBN: 9780470092194.
- [10] J.-L. Basdevant, J. Rich, and M. Spiro. *Fundamentals in Nuclear Physics*. Springer-Verlag GmbH, 2005. ISBN: 0387016724.
- [11] M. Berglund and M. E. Wieser. “Isotopic compositions of the elements 2009 (IUPAC Technical Report)”. In: *Pure and Applied Chemistry* 83.2 (2011), pp. 397–410. DOI: 10.1351/pac-rep-10-06-02.
- [12] L. L. Lucas and M. P. Unterweger. “Comprehensive review and critical evaluation of the half-life of tritium”. In: *Journal of Research of the National Institute of Standards and Technology* 105.4 (2000), p. 541. DOI: 10.6028/jres.105.043.
- [13] T. Tanabe. *Tritium: Fuel of Fusion Reactors*. Ed. by T. Tanabe. Springer Japan, 2017. ISBN: 978-4-431-56460-7. DOI: 10.1007/978-4-431-56460-7.

-
- [14] M. Keilhacker et al. “High fusion performance from deuterium-tritium plasmas in JET”. In: *Nuclear Fusion* 39.2 (1999), pp. 209–234. DOI: 10.1088/0029-5515/39/2/306.
- [15] J. D. Lawson. “Some Criteria for a Power Producing Thermonuclear Reactor”. In: *Proceedings of the Physical Society. Section B* 70.1 (1957), pp. 6–10. DOI: 10.1088/0370-1301/70/1/303.
- [16] G. Pucella and S. E. Segre. *Fisica dei plasmi*. Zanichelli, 2010. ISBN: 9788808063830.
- [17] U. Stroth. *Plasmaphysik*. Springer Berlin Heidelberg, 2018. ISBN: 978-3-662-55236-0. DOI: 10.1007/978-3-662-55236-0.
- [18] J. Wesson. *Tokamaks*. Oxford University Press, 2011. 832 pp. ISBN: 9780199592234.
- [19] J. Nuckolls et al. “Laser Compression of Matter to Super-High Densities: Thermonuclear (CTR) Applications”. In: *Nature* 239.5368 (1972), pp. 139–142. DOI: 10.1038/239139a0.
- [20] S. Pfalzner. *An Introduction to Inertial Confinement Fusion*. CRC Press, Mar. 2, 2006. 248 pp. ISBN: 9780750307017.
- [21] F. Chen. *Introduction to Plasma Physics and Controlled Fusion*. Springer-Verlag GmbH, Nov. 10, 2015. ISBN: 3319223089.
- [22] T. J. M. Boyd and J. J. Sanderson. *The Physics of Plasmas*. Cambridge University Press, Sept. 17, 2007. 548 pp. ISBN: 0521459125. DOI: 10.1017/CB09780511755750.
- [23] M. Wakatani. *Stellarator and Heliotron Devices*. International Series of Monographs on Physics. Oxford University Press, 1998. ISBN: 0195078314.
- [24] J. Wesson. *The Science of JET*. JET-R(91)14. EUROfusion, 1999. URL: <http://www.euro-fusionscipub.org/archives/jet-archive/the-science-of-jet>.
- [25] A. Kallenbach et al. “Partial detachment of high power discharges in ASDEX Upgrade”. In: *Nuclear Fusion* 55.5 (2015), p. 053026. DOI: 10.1088/0029-5515/55/5/053026.
- [26] R. A. Pitts et al. “Status and physics basis of the ITER divertor”. In: *Physica Scripta* T138 (2009), p. 014001. DOI: 10.1088/0031-8949/2009/t138/014001.
- [27] G. Federici et al. “European DEMO design strategy and consequences for materials”. In: *Nuclear Fusion* 57.9 (2017), p. 092002. DOI: 10.1088/1741-4326/57/9/092002.
- [28] M. Shimada et al. “Chapter 1: Overview and summary”. In: *Nuclear Fusion* 47.6 (2007), S1–S17. DOI: 10.1088/0029-5515/47/6/s01.
- [29] H. Zohm et al. “On the physics guidelines for a tokamak DEMO”. In: *Nuclear Fusion* 53.7 (2013), p. 073019. DOI: 10.1088/0029-5515/53/7/073019.
- [30] G. Giruzzi et al. “Modelling of pulsed and steady-state DEMO scenarios”. In: *Nuclear Fusion* 55.7 (2015), p. 073002. DOI: 10.1088/0029-5515/55/7/073002.
- [31] R. P. Wenninger et al. “DEMO divertor limitations during and in between ELMs”. In: *Nuclear Fusion* 54.11 (2014), p. 114003. DOI: 10.1088/0029-5515/54/11/114003.
- [32] M. Wischmeier, The ASDEX Upgrade Team, and JET EFDA Contributors. “High density operation for reactor-relevant power exhaust”. In: *Journal of Nuclear Materials* 463 (2015), pp. 22–29. DOI: 10.1016/j.jnucmat.2014.12.078.
- [33] T. Pütterich et al. “Calculation and experimental test of the cooling factor of tungsten”. In: *Nuclear Fusion* 50.2 (2010), p. 025012. DOI: 10.1088/0029-5515/50/2/025012.

-
- [34] T. Pütterich et al. “Determination of the tolerable impurity concentrations in a fusion reactor using a consistent set of cooling factors”. In: *Nuclear Fusion* 59.5 (2019), p. 056013. DOI: 10.1088/1741-4326/ab0384.
- [35] R. Wenninger et al. “The physics and technology basis entering European system code studies for DEMO”. In: *Nuclear Fusion* 57.1 (2017), p. 016011. DOI: 10.1088/0029-5515/57/1/016011.
- [36] C. Giroud et al. “Impact of nitrogen seeding on confinement and power load control of a high-triangularity JET ELMy H-mode plasma with a metal wall”. In: *Nuclear Fusion* 53.11 (2013), p. 113025. DOI: 10.1088/0029-5515/53/11/113025.
- [37] A. Huber et al. “Impact of strong impurity seeding on the radiation losses in JET with ITER-like Wall”. In: *Proceedings of the 41st EPS Conference on Controlled Fusion and Plasma Physics, Berlin, 2014*. P1.031. 2014. URL: <http://ocs.ciemat.es/EPS2014PAP/pdf/P1.031.pdf>.
- [38] S. Glögler et al. “Characterisation of highly radiating neon seeded plasmas in JET-ILW”. In: *Nuclear Fusion* 59.12 (2019), p. 126031. DOI: 10.1088/1741-4326/ab3f7a.
- [39] X. Bonnin et al. “Presentation of the New SOLPS-ITER Code Package for Tokamak Plasma Edge Modelling”. In: *Plasma and Fusion Research* 11 (2016), pp. 1403102–1403102. DOI: 10.1585/pfr.11.1403102.
- [40] S. Wiesen et al. “The new SOLPS-ITER code package”. In: *Journal of Nuclear Materials* 463 (2015), pp. 480–484. DOI: 10.1016/j.jnucmat.2014.10.012.
- [41] Max Planck Institute for Plasma Physics and C. Brandt. “IPP Bilddatenbank”. 2011.
- [42] P. C. Stangeby. *The Plasma Boundary of Magnetic Fusion Devices*. Series in Plasma Physics. CRC Press, 2000. ISBN: 0750305592.
- [43] J. P. Freidberg. *Plasma Physics and Fusion Energy*. Cambridge University Press, 2010. ISBN: 0521733170.
- [44] E. J. Doyle et al. “Chapter 2: Plasma confinement and transport”. In: *Nuclear Fusion* 47.6 (2007), S18–S127. DOI: 10.1088/0029-5515/47/6/s02.
- [45] F. Troyon et al. “MHD-Limits to Plasma Confinement”. In: *Plasma Physics and Controlled Fusion* 26.1A (1984), pp. 209–215. DOI: 10.1088/0741-3335/26/1a/319.
- [46] ITER Physics Expert Group on Confinement and Transport, ITER Physics Expert Group on Confinement Modelling and Database, and ITER Physics Basis Editors. “Chapter 2: Plasma confinement and transport”. In: *Nuclear Fusion* 39.12 (1999), pp. 2175–2249. DOI: 10.1088/0029-5515/39/12/302.
- [47] J. Schweinzer et al. “Development of the Q = 10 scenario for ITER on ASDEX Upgrade (AUG)”. In: *Nuclear Fusion* 56.10 (2016), p. 106007. DOI: 10.1088/0029-5515/56/10/106007.
- [48] K. Thomsen et al. “ITER H mode confinement database update”. In: *Nuclear Fusion* 34.1 (1994), pp. 131–167. DOI: 10.1088/0029-5515/34/1/i10.
- [49] M. Greenwald et al. “A new look at density limits in tokamaks”. In: *Nuclear Fusion* 28.12 (1988), pp. 2199–2207. DOI: 10.1088/0029-5515/28/12/009.
- [50] M. Greenwald. “Density limits in toroidal plasmas”. In: *Plasma Physics and Controlled Fusion* 44.8 (2002), R27–R53. DOI: 10.1088/0741-3335/44/8/201.

-
- [51] ITER Physics Expert Group on Disruptions, Plasma Control, and MHD and ITER Physics Basis Editors. “Chapter 3: MHD stability, operational limits and disruptions”. In: *Nuclear Fusion* 39.12 (1999), pp. 2251–2389. DOI: 10.1088/0029-5515/39/12/303.
- [52] P. C. de Vries et al. “Survey of disruption causes at JET”. In: *Nuclear Fusion* 51.5 (2011), p. 053018. DOI: 10.1088/0029-5515/51/5/053018.
- [53] B. Lipschultz et al. “Marfe: an edge plasma phenomenon”. In: *Nuclear Fusion* 24.8 (1984), pp. 977–988. DOI: 10.1088/0029-5515/24/8/002.
- [54] R. Behrisch and W. Eckstein, eds. *Sputtering by Particle Bombardment*. Springer-Verlag GmbH, July 26, 2007. ISBN: 9783540445029. DOI: 10.1007/978-3-540-44502-9.
- [55] C. S. Pitcher and P. C. Stangeby. “Experimental divertor physics”. In: *Plasma Physics and Controlled Fusion* 39.6 (1997), pp. 779–930. DOI: 10.1088/0741-3335/39/6/001.
- [56] *Fusion Wiki: Triangularity*. Fusion Wiki entry; last modified on 17 June 2014, at 14:24. URL: <http://fusionwiki.ciemat.es/wiki/Triangularity>.
- [57] D. D. Ryutov. “Geometrical properties of a “snowflake” divertor”. In: *Physics of Plasmas* 14.6 (2007), p. 064502. DOI: 10.1063/1.2738399.
- [58] P. M. Valanju et al. “Super-X divertors and high power density fusion devices”. In: *Physics of Plasmas* 16.5 (2009), p. 056110. DOI: 10.1063/1.3110984.
- [59] T. Lunt et al. “Proposal of an alternative upper divertor in ASDEX Upgrade supported by EMC3-EIRENE simulations”. In: *Nuclear Materials and Energy* 12 (2017), pp. 1037–1042. DOI: 10.1016/j.nme.2016.12.035.
- [60] H. Reimerdes et al. “TCV divertor upgrade for alternative magnetic configurations”. In: *Nuclear Materials and Energy* 12 (2017), pp. 1106–1111. DOI: 10.1016/j.nme.2017.02.013.
- [61] J. R. Harrison et al. “Overview of new MAST physics in anticipation of first results from MAST Upgrade”. In: *Nuclear Fusion* 59.11 (2019), p. 112011. DOI: 10.1088/1741-4326/ab121c.
- [62] F. Wagner et al. “Regime of Improved Confinement and High Beta in Neutral-Beam-Heated Divertor Discharges of the ASDEX Tokamak”. In: *Physical Review Letters* 49.19 (1982), pp. 1408–1412. DOI: 10.1103/physrevlett.49.1408.
- [63] ASDEX Team et al. “Importance of the divertor configuration for attaining the H-regime in ASDEX”. In: *Journal of Nuclear Materials* 121 (1984), pp. 103–113. DOI: 10.1016/0022-3115(84)90109-0.
- [64] F. Wagner et al. “Experimental evidence for neoclassical ion transport effects in the H-transition of ASDEX”. In: *Nuclear Fusion* 25.10 (1985), pp. 1490–1495. DOI: 10.1088/0029-5515/25/10/013.
- [65] F. Ryter et al. “Experimental Characterization of the Electron Heat Transport in Low-Density ASDEX Upgrade Plasmas”. In: *Physical Review Letters* 86.24 (2001), pp. 5498–5501. DOI: 10.1103/physrevlett.86.5498.
- [66] H. Biglari, P. H. Diamond, and P. W. Terry. “Influence of sheared poloidal rotation on edge turbulence”. In: *Physics of Fluids B: Plasma Physics* 2.1 (1990), pp. 1–4. DOI: 10.1063/1.859529.

-
- [67] F. Ryter et al. “L-H transition physics in hydrogen and deuterium: key role of the edge radial electric field and ion heat flux”. In: *Plasma Physics and Controlled Fusion* 58.1 (2015), p. 014007. DOI: 10.1088/0741-3335/58/1/014007.
- [68] ITER Physics Basis Editors, ITER Physics Expert Group Chairs and Co-Chairs, and ITER Joint Central Team and Physics Unit. “Chapter 1: Overview and summary”. In: *Nuclear Fusion* 39.12 (1999), pp. 2137–2174. DOI: 10.1088/0029-5515/39/12/301.
- [69] G. Federici et al. “Overview of EU DEMO design and R&D activities”. In: *Fusion Engineering and Design* 89.7-8 (2014), pp. 882–889. DOI: 10.1016/j.fusengdes.2014.01.070.
- [70] Y. R. Martin, T. Takizuka, and the ITPA CDBM H-mode Threshold Data Group. “Power requirement for accessing the H-mode in ITER”. In: *Journal of Physics: Conference Series* 123 (2008), p. 012033. DOI: 10.1088/1742-6596/123/1/012033.
- [71] T. Takizuka and ITER Confinement Database and Modelling Expert Group. “Threshold Power and Energy Confinement for ITER”. In: *Proc. 16th IAEA Fusion Energy Conf., Montreal (Canada)*. Vol. 2. IAEA-CN-64/F-5. 1996.
- [72] M. Sato et al. “Threshold power for the H-mode transition in JT-60U plasmas”. In: *Plasma Physics and Controlled Fusion* 38.8 (1996), pp. 1283–1288. DOI: 10.1088/0741-3335/38/8/023.
- [73] E. Delabie et al. “Status of TC-26: L-H/H-L scaling in the presence of Metallic walls, Scaling of the JET-ILW L-H threshold power in vertical target configuration, Report on TC-26 presented at the 21st T&C ITPA meeting (2018)”. 2018.
- [74] M. Keilhacker et al. “Confinement studies in L and H-type ASDEX discharges”. In: *Plasma Physics and Controlled Fusion* 26.1A (1984), pp. 49–63. DOI: 10.1088/0741-3335/26/1a/305.
- [75] H. Zohm. “Edge localized modes (ELMs)”. In: *Plasma Physics and Controlled Fusion* 38.2 (1996), pp. 105–128. DOI: 10.1088/0741-3335/38/2/001.
- [76] G. Calabrò et al. “H-mode threshold studies in helium-4 JET plasmas”. In: *Proceedings of the 37th EPS Conference on Controlled Fusion and Plasma Physics, Dublin, 2010*. O5.127. 2010. URL: <http://ocs.ciemat.es/EPS2010PAP/pdf/O5.127.pdf>.
- [77] E. R. Solano et al. “M-mode: axi-symmetric magnetic oscillation and ELM-less H-mode in JET”. In: *Proceedings of the 40th EPS Conference on Controlled Fusion and Plasma Physics, Helsinki, 2013*. P4.111. 2013. URL: <http://ocs.ciemat.es/EPS2013PAP/pdf/P4.111.pdf>.
- [78] E. R. Solano et al. “Axisymmetric oscillations at L–H transitions in JET: M-mode”. In: *Nuclear Fusion* 57.2 (2017), p. 022021. DOI: 10.1088/0029-5515/57/2/022021.
- [79] D. I. Réfy et al. “Identity of the JET M-mode and the ASDEX Upgrade I-phase phenomena”. In: *Nuclear Fusion* 60.5 (2020), p. 056004. DOI: 10.1088/1741-4326/ab7594.
- [80] G. D. Conway et al. “Mean and Oscillating Plasma Flows and Turbulence Interactions across the L–H Confinement Transition”. In: *Physical Review Letters* 106 (2011), p. 065001. DOI: 10.1103/physrevlett.106.065001.

-
- [81] G. Birkenmeier et al. “Characterisation of Pulsations Close to The L–H Transition in AUG”. In: *Proceedings of the 42nd EPS Conference on Controlled Fusion and Plasma Physics, Lisbon, 2015*. P1.125. 2015. URL: <http://ocs.ciemat.es/EPS2015PAP/pdf/P1.125.pdf>.
- [82] G. S. Xu et al. “Dynamics of L–H transition and I-phase in EAST”. In: *Nuclear Fusion* 54.10 (2014), p. 103002. DOI: 10.1088/0029-5515/54/10/103002.
- [83] J. Cheng et al. “Dynamics of Low-Intermediate–High-Confinement Transitions in Toroidal Plasmas”. In: *Physical Review Letters* 110.26 (2013). DOI: 10.1103/physrevlett.110.265002.
- [84] G. Birkenmeier et al. “Magnetic structure and frequency scaling of limit-cycle oscillations close to L– to H-mode transitions”. In: *Nuclear Fusion* 56.8 (2016), p. 086009. DOI: 10.1088/0029-5515/56/8/086009.
- [85] D. I. Réfy et al. “Comparative analysis of density profile and magnetic signals during the JET M-mode and ASDEX Upgrade I-phase phenomena”. In: *Proceedings of the 43rd EPS Conference on Controlled Fusion and Plasma Physics, Leuven, 2016*. P1.023. 2016. URL: <http://ocs.ciemat.es/EPS2016PAP/pdf/P1.023.pdf>.
- [86] A. Huber et al. “Impact of the ITER-like wall on divertor detachment and on the density limit in the JET tokamak”. In: *Journal of Nuclear Materials* 438 (2013), S139–S147. DOI: 10.1016/j.jnucmat.2013.01.022.
- [87] A. Huber et al. “Density limit of H-mode plasmas on JET-ILW”. In: *Journal of Nuclear Materials* 463 (2015), pp. 445–449. DOI: 10.1016/j.jnucmat.2014.11.055.
- [88] M. Bernert et al. “The H-mode density limit in the full tungsten ASDEX Upgrade tokamak”. In: *Plasma Physics and Controlled Fusion* 57.1 (2015), p. 014038. DOI: 10.1088/0741-3335/57/1/014038.
- [89] D. Bohm. *The characteristics of electrical discharges in magnetic fields*. McGraw-Hill, New York, USA, 1949.
- [90] K.-U. Riemann. “The Bohm criterion and sheath formation”. In: *Journal of Physics D: Applied Physics* 24.4 (1991), pp. 493–518. DOI: 10.1088/0022-3727/24/4/001.
- [91] R. Chodura. “Plasma–wall transition in an oblique magnetic field”. In: *Physics of Fluids* 25.9 (1982), p. 1628. DOI: 10.1063/1.863955.
- [92] D. Naujoks. *Plasma-Material Interaction in Controlled Fusion*. First. Springer Series on Atomic, Optical, and Plasma Physics 39. Springer-Verlag Berlin Heidelberg, 2006. ISBN: 978-3-540-32149-1. DOI: 10.1007/3-540-32149-7.
- [93] J. Roth et al. “Flux dependence of carbon erosion and implication for ITER”. In: *Journal of Nuclear Materials* 337-339 (2005), pp. 970–974. DOI: 10.1016/j.jnucmat.2004.10.115.
- [94] G. Federici et al. “Plasma-material interactions in current tokamaks and their implications for next step fusion reactors”. In: *Nuclear Fusion* 41.12 (2001), pp. 1967–2137. DOI: 10.1088/0029-5515/41/12/218.
- [95] J. H. You et al. “European DEMO divertor target: Operational requirements and material-design interface”. In: *Nuclear Materials and Energy* 9 (2016), pp. 171–176. DOI: 10.1016/j.nme.2016.02.005.

-
- [96] C. Linsmeier et al. “Development of advanced high heat flux and plasma-facing materials”. In: *Nuclear Fusion* 57.9 (2017), p. 092007. DOI: 10.1088/1741-4326/aa6f71.
- [97] R. Wenninger et al. “The DEMO wall load challenge”. In: *Nuclear Fusion* 57.4 (2017), p. 046002. DOI: 10.1088/1741-4326/aa4fb4.
- [98] U. Fantz. “Basics of plasma spectroscopy”. In: *Plasma Sources Science and Technology* 15.4 (2006), S137–S147. DOI: 10.1088/0963-0252/15/4/s01.
- [99] G. Drake, ed. *Springer Handbook of Atomic, Molecular, and Optical Physics*. Springer New York, 2006. ISBN: 9780387263083. DOI: 10.1007/978-0-387-26308-3.
- [100] H.-J. Kunze. *Introduction to Plasma Spectroscopy*. Springer Series on Atomic, Optical, and Plasma Physics 56. Springer Berlin Heidelberg, 2009. ISBN: 9783642022326. DOI: 10.1007/978-3-642-02233-3.
- [101] V. Kotov, D. Reiter, and A. S. Kukushkin. *Numerical study of the ITER divertor plasma with the B2-EIRENE code package*. Bericht des Forschungszentrum Jülich Jül-2599. Forschungszentrum Jülich GmbH Zentralbibliothek, Verlag, 2007. URL: <http://hdl.handle.net/2128/13947>.
- [102] H. R. Griem. *Principles of Plasma Spectroscopy*. Cambridge University Press, 1997. ISBN: 9780511524578.
- [103] I. H. Hutchinson. *Principles of Plasma Diagnostics*. Cambridge University Press, 2005. 460 pp. ISBN: 9780521675741.
- [104] D. J. Ward. “The physics of DEMO”. In: *Plasma Physics and Controlled Fusion* 52.12 (2010), p. 124033. DOI: 10.1088/0741-3335/52/12/124033.
- [105] B. Lomanowski et al. “Interpretation of Lyman opacity measurements in JET with the ITER-like wall using a particle balance approach”. In: *Plasma Physics and Controlled Fusion* 62.6 (2020), p. 065006. DOI: 10.1088/1361-6587/ab7432.
- [106] A. Loarte et al. “Chapter 4: Power and particle control”. In: *Nuclear Fusion* 47.6 (2007), S203–S263. DOI: 10.1088/0029-5515/47/6/s04.
- [107] R. Dux and A. G. Peeters. “Neoclassical impurity transport in the core of an ignited tokamak plasma”. In: *Nuclear Fusion* 40.10 (2000), pp. 1721–1729. DOI: 10.1088/0029-5515/40/10/304.
- [108] T. Pütterich et al. “Impurity Limits in a Reactor Grade Fusion Device”. In: *Proceedings of the 42nd EPS Conference on Controlled Fusion and Plasma Physics, Lisbon, 2015*. P4.111. 2015. URL: <http://ocs.ciemat.es/EPS2015PAP/pdf/P4.111.pdf>.
- [109] A. Kramida et al. *NIST Atomic Spectra Database (ver. 5.7.1)*. 2019. DOI: 10.18434/T4W30F. URL: <https://physics.nist.gov/asd>.
- [110] R. Dux. *Impurity transport in Tokamak plasmas*. eng. IPP Report 10/27. Garching bei München: Max-Planck-Institut für Plasmaphysik, 2004. URL: <http://hdl.handle.net/11858/00-001M-0000-0027-2036-E>.
- [111] R. Neu et al. “New results from the tungsten programme at ASDEX Upgrade”. In: *Journal of Nuclear Materials* 313-316 (2003), pp. 116–126. DOI: 10.1016/s0022-3115(02)01386-7.

-
- [112] C. M. Bruhn. “Characterization of the turbulence driven boron transport in the core of fusion plasmas in the ASDEX Upgrade tokamak”. Dissertation. München: Technische Universität München, 2019. URL: <http://nbn-resolving.de/urn/resolver.pl?urn:nbn:de:bvb:91-diss-20190108-1462516-1-6>.
- [113] R. Dux et al. “The interplay of controlling the power exhaust and the tungsten content in ITER”. In: *Nuclear Materials and Energy* 12 (2017), pp. 28–35. DOI: 10.1016/j.nme.2016.10.013.
- [114] P. C. Stangeby. “Basic physical processes and reduced models for plasma detachment”. In: *Plasma Physics and Controlled Fusion* 60.4 (2018), p. 044022. DOI: 10.1088/1361-6587/aaacf6.
- [115] S. I. Krasheninnikov, A. S. Kukushkin, and A. A. Pshenov. “Divertor plasma detachment”. In: *Physics of Plasmas* 23.5 (2016), p. 055602. DOI: 10.1063/1.4948273.
- [116] S. I. Braginskii. “Transport Processes in a Plasma”. In: *Reviews of Plasma Physics* 1 (1965). Edited by Acad. M. A. Leontovich; Consultants Bureau, New York, pp. 205–311.
- [117] L. Spitzer and R. Härm. “Transport Phenomena in a Completely Ionized Gas”. In: *Physical Review* 89.5 (1953), pp. 977–981. DOI: 10.1103/physrev.89.977.
- [118] A. W. Leonard et al. “Energy Transport and Dissipation in DIII-D Detached Divertor Plasmas”. In: *Proceedings of the 46th EPS Conference on Controlled Fusion and Plasma Physics, Milan, 2019*. O4.105. 2019. URL: <http://ocs.ciemat.es/EPS2019PAP/pdf/O4.105.pdf>.
- [119] Y. Shimomura et al. “Characteristics of the divertor plasma in neutral-beam-heated ASDEX discharges”. In: *Nuclear Fusion* 23.7 (1983), pp. 869–879. DOI: 10.1088/0029-5515/23/7/002.
- [120] ITER Physics Expert Group on Divertor, ITER Physics Expert Group on Divertor Modelling and Database, and ITER Physics Basis Editors. “Chapter 4: Power and particle control”. In: *Nuclear Fusion* 39.12 (1999), pp. 2391–2469. DOI: 10.1088/0029-5515/39/12/304.
- [121] R. Schneider et al. “Plasma Edge Physics with B2-Eirene”. In: *Contributions to Plasma Physics* 46.1-2 (2006), pp. 3–191. DOI: 10.1002/ctpp.200610001.
- [122] S. I. Krasheninnikov and A. S. Kukushkin. “Physics of ultimate detachment of a tokamak divertor plasma”. In: *Journal of Plasma Physics* 83.5 (2017). DOI: 10.1017/s0022377817000654.
- [123] A. A. Pshenov, A. S. Kukushkin, and S. I. Krasheninnikov. “Energy balance in plasma detachment”. In: *Nuclear Materials and Energy* 12 (2017), pp. 948–952. DOI: 10.1016/j.nme.2017.03.019.
- [124] A. Loarte et al. “Plasma detachment in JET Mark I divertor experiments”. In: *Nuclear Fusion* 38.3 (1998), pp. 331–371. DOI: 10.1088/0029-5515/38/3/303.
- [125] L. L. Lengyel. *Analysis of Radiating Plasma Boundary Layers*. IPP-Report 5/98. Max-Planck-Institut für Plasmaphysik, Garching, Germany, 1981. URL: <http://hdl.handle.net/11858/00-001M-0000-0027-4510-D>.

-
- [126] S. Henderson et al. “Experimental studies of the nitrogen concentration required for divertor detachment in ASDEX Upgrade”. In: *3rd IAEA Technical Meeting on Divertor Concepts, Vienna, Austria, November 2019*. 2019. URL: <https://conferences.iaea.org/event/192/contributions/15226/attachments/8311/10973/ID43-Henderson.pdf>.
- [127] R. J. Goldston, M. L. Reinke, and J. A. Schwartz. “A new scaling for divertor detachment”. In: *Plasma Physics and Controlled Fusion* 59.5 (2017), p. 055015. DOI: 10.1088/1361-6587/aa5e6e.
- [128] R. A. Pitts et al. “Physics basis for the first ITER tungsten divertor”. In: *Nuclear Materials and Energy* 20 (2019), p. 100696. DOI: 10.1016/j.nme.2019.100696.
- [129] R. A. Pitts et al. “The first ITER tungsten divertor: operating space and lifetime”. In: *3rd IAEA Technical Meeting on Divertor Concepts, Vienna, Austria, November 2019*. 2019. URL: https://conferences.iaea.org/event/192/contributions/15259/attachments/8369/11068/pitts_iaea_div_tm_07_11_2019_ITER_D_2FGYSX.pdf.
- [130] M. L. Reinke. “Heat flux mitigation by impurity seeding in high-field tokamaks”. In: *Nuclear Fusion* 57.3 (2017), p. 034004. DOI: 10.1088/1741-4326/aa5145.
- [131] A. Kallenbach et al. “Multi-machine comparisons of divertor heat flux mitigation by radiative cooling with nitrogen”. In: *24th IAEA Fusion Energy Conference, San Diego, USA, October 8–13, 2012*. ITR/P1-28. 2012. URL: http://www-naweb.iaea.org/napc/physics/FEC/FEC2012/papers/345_ITRP128.pdf.
- [132] A. Kallenbach et al. “Optimized tokamak power exhaust with double radiative feedback in ASDEX Upgrade”. In: *Nuclear Fusion* 52.12 (2012), p. 122003. DOI: 10.1088/0029-5515/52/12/122003.
- [133] T. Eich et al. “Inter-ELM Decay Length for JET and ASDEX Upgrade: Measurement and Comparison with Heuristic Drift-Based Model”. In: *Physical Review Letters* 107.21 (2011). DOI: 10.1103/physrevlett.107.215001.
- [134] H. Lux et al. “Impurity radiation in DEMO systems modelling”. In: *Fusion Engineering and Design* 101 (2015), pp. 42–51. DOI: 10.1016/j.fusengdes.2015.10.002.
- [135] A. Kallenbach et al. “Plasma surface interactions in impurity seeded plasmas”. In: *Journal of Nuclear Materials* 415.1 (2011), S19–S26. DOI: 10.1016/j.jnucmat.2010.11.105.
- [136] M. Oberkofler et al. “First nitrogen-seeding experiments in JET with the ITER-like Wall”. In: *Journal of Nuclear Materials* 438 (2013), S258–S261. DOI: 10.1016/j.jnucmat.2013.01.041.
- [137] A. Drenik et al. “Evolution of nitrogen concentration and ammonia production in N₂-seeded H-mode discharges at ASDEX Upgrade”. In: *Nuclear Fusion* 59.4 (2019), p. 046010. DOI: 10.1088/1741-4326/aafe23.
- [138] E. Joffrin et al. “Overview of the JET preparation for deuterium–tritium operation with the ITER like-wall”. In: *Nuclear Fusion* 59.11 (2019), p. 112021. DOI: 10.1088/1741-4326/ab2276.
- [139] F. Reimold et al. “Divertor studies in nitrogen induced completely detached H-modes in full tungsten ASDEX Upgrade”. In: *Nuclear Fusion* 55.3 (2015), p. 033004. DOI: 10.1088/0029-5515/55/3/033004.

-
- [140] M. Bernert et al. “Power exhaust by SOL and pedestal radiation at ASDEX Upgrade and JET”. In: *Nuclear Materials and Energy* 12 (2017), pp. 111–118. DOI: 10.1016/j.nme.2016.12.029.
- [141] S. Potzel et al. “Formation of the high density front in the inner far SOL at ASDEX Upgrade and JET”. In: *Journal of Nuclear Materials* 463 (2015), pp. 541–545. DOI: 10.1016/j.jnucmat.2014.12.008.
- [142] E. Wolfrum et al. “Impact of wall materials and seeding gases on the pedestal and on core plasma performance”. In: *Nuclear Materials and Energy* 12 (2017), pp. 18–27. DOI: 10.1016/j.nme.2017.01.002.
- [143] A. Huber et al. “Peculiarity of highly radiating multi-impurity seeded H-mode plasmas on JET with ITER-like wall”. In: *Physica Scripta* T171 (2020), p. 014055. DOI: 10.1088/1402-4896/ab5753.
- [144] G. F. Matthews et al. “Energy balance in JET”. In: *Nuclear Materials and Energy* 12 (2017), pp. 227–233. DOI: 10.1016/j.nme.2016.12.012.
- [145] C. Guillemaut et al. “Main chamber wall plasma loads in JET-ITER-like wall at high radiated fraction”. In: *Nuclear Materials and Energy* 12 (2017), pp. 234–240. DOI: 10.1016/j.nme.2017.02.010.
- [146] R. Dux et al. “Transport of tungsten in the H-mode edge transport barrier of ITER”. In: *Plasma Physics and Controlled Fusion* 56.12 (2014), p. 124003. DOI: 10.1088/0741-3335/56/12/124003.
- [147] H. Urano et al. “Roles of argon seeding in energy confinement and pedestal structure in JT-60U”. In: *Nuclear Fusion* 55.3 (2015), p. 033010. DOI: 10.1088/0029-5515/55/3/033010.
- [148] A. Kallenbach et al. “Developments towards an ELM-free pedestal radiative cooling scenario using noble gas seeding in ASDEX Upgrade”. In: *Nuclear Fusion* (2021). DOI: 10.1088/1741-4326/abbba0.
- [149] A. Loarte et al. “High confinement/high radiated power H-mode experiments in Alcator C-Mod and consequences for International Thermonuclear Experimental Reactor (ITER) QDT=10 operation”. In: *Physics of Plasmas* 18.5 (2011), p. 056105. DOI: 10.1063/1.3567547.
- [150] G. Telesca et al. “High power neon seeded JET discharges: Experiments and simulations”. In: *Nuclear Materials and Energy* 12 (2017), pp. 882–886. DOI: 10.1016/j.nme.2016.10.012.
- [151] G. F. Matthews et al. “Studies in JET divertors of varied geometry. II: Impurity seeded plasmas”. In: *Nuclear Fusion* 39.1 (1999), pp. 19–40. DOI: 10.1088/0029-5515/39/1/302.
- [152] F. Reimold et al. “Experimental studies and modeling of complete H-mode divertor detachment in ASDEX Upgrade”. In: *Journal of Nuclear Materials* 463 (2015), pp. 128–134. DOI: 10.1016/j.jnucmat.2014.12.019.
- [153] F. Reimold et al. “The high field side high density region in SOLPS-modeling of nitrogen-seeded H-modes in ASDEX Upgrade”. In: *Nuclear Materials and Energy* 12 (2017), pp. 193–199. DOI: 10.1016/j.nme.2017.01.010.

-
- [154] L. Y. Xiang et al. “Modeling of argon seeding in ASDEX Upgrade H-mode plasma with SOLPS5.0”. In: *Nuclear Materials and Energy* 12 (2017), pp. 1146–1151. DOI: 10.1016/j.nme.2017.02.017.
- [155] F. Hitzler et al. “Impurity transport and divertor retention in Ar and N seeded SOLPS 5.0 simulations for ASDEX Upgrade”. In: *Plasma Physics and Controlled Fusion* 62.8 (2020), p. 085013. DOI: 10.1088/1361-6587/ab9b00.
- [156] I. Y. Senichenkov et al. “On mechanisms of impurity leakage and retention in the tokamak divertor”. In: *Plasma Physics and Controlled Fusion* 61.4 (2019), p. 045013. DOI: 10.1088/1361-6587/ab04d0.
- [157] J. Chen et al. “Experimental investigation and SOLPS-ITER modeling of Ne-seeded radiative divertor H-modes plasma on EAST”. In: *Physics of Plasmas* 26.5 (2019), p. 052501. DOI: 10.1063/1.5085892.
- [158] E. Sytova et al. “Comparing N versus Ne as divertor radiators in ASDEX-upgrade and ITER”. In: *Nuclear Materials and Energy* 19 (2019), pp. 72–78. DOI: 10.1016/j.nme.2019.02.019.
- [159] E. Kaveeva et al. “SOLPS-ITER modelling of ITER edge plasma with drifts and currents”. In: *Nuclear Fusion* 60.4 (2020), p. 046019. DOI: 10.1088/1741-4326/ab73c1.
- [160] I. Y. Senichenkov et al. “Approaching the radiating X-point in SOLPS-ITER modeling of ASDEX Upgrade H-mode discharges”. In: *Plasma Physics and Controlled Fusion* 63.5 (2021), p. 055011. DOI: 10.1088/1361-6587/abe886.
- [161] C. Guillemaut et al. “Influence of atomic physics on EDGE2D-EIRENE simulations of JET divertor detachment with carbon and beryllium/tungsten plasma-facing components”. In: *Nuclear Fusion* 54.9 (2014), p. 093012. DOI: 10.1088/0029-5515/54/9/093012.
- [162] A. E. Jaervinen et al. “Interpretation of radiative divertor studies with impurity seeding in type-I ELMy H-mode plasmas in JET-ILW using EDGE2D-EIRENE”. In: *Journal of Nuclear Materials* 463 (2015), pp. 135–142. DOI: 10.1016/j.jnucmat.2014.10.047.
- [163] A. E. Jaervinen et al. “Impact of divertor geometry on radiative divertor performance in JET H-mode plasmas”. In: *Plasma Physics and Controlled Fusion* 58.4 (2016), p. 045011. DOI: 10.1088/0741-3335/58/4/045011.
- [164] G. Telesca et al. “Simulation of JET ITER-Like Wall pulses at high neon seeding rate”. In: *Nuclear Fusion* 57.12 (2017), p. 126021. DOI: 10.1088/1741-4326/aa8381.
- [165] A. S. Kukushkin et al. “Finalizing the ITER divertor design: The key role of SOLPS modeling”. In: *Fusion Engineering and Design* 86.12 (2011), pp. 2865–2873. DOI: 10.1016/j.fusengdes.2011.06.009.
- [166] B. J. Braams. “Computational Studies in Tokamak Equilibrium and Transport”. PhD thesis. Rijksuniversiteit Utrecht (Netherlands), 1986. URL: http://inis.iaea.org/search/search.aspx?orig_q=RN:18038616.
- [167] D. Reiter. *The EIRENE code, version: Jan. 1992: users manual*. Bericht des Forschungszentrum Jülich Jül-2599. Forschungszentrum Jülich GmbH Zentralbibliothek, Verlag, 1992. URL: <http://hdl.handle.net/2128/19141>.

-
- [168] D. Reiter. *The EIRENE Code User Manual*. Institut für Energie- und Klimaforschung – Plasmaphysik, Forschungszentrum Jülich GmbH. 2019. URL: <http://www.eirene.de/eirene.pdf>.
- [169] M. Baelmans. “Code improvements and applications of a two-dimensional edge plasma model for toroidal fusion devices”. PhD thesis. Katholieke Universiteit Leuven, Belgium, 1993. URL: https://limo.libis.be/primo-explore/fulldisplay?docid=LIRIAS1744657&context=L&vid=Lirias&search_scope=Lirias&tab=default_tab&lang=en_US.
- [170] N. A. Krall and A. W. Trivelpiece. *Principles of plasma physics*. International Series in Pure and Applied Physics. McGraw-Hill, 1973. ISBN: 0070353468.
- [171] R. Balescu. *Transport Processes in Plasmas: Classical Transport Theory*. Elsevier Science Ltd, 1988. ISBN: 0-444-87091-1.
- [172] R. Balescu. *Transport Processes in Plasmas: Neoclassical Transport Theory*. Elsevier Science Ltd, 1988. ISBN: 0-444-87092-X.
- [173] E. D. Cashwell and C. J. Everett. *Monte Carlo Method for random walk problems*. International Tracts in Computer Science and Technology and Their Application. Pergamon Press, 1959.
- [174] J. Spanier and E. M. Gelbard. *Monte Carlo Principles and Neutron Transport Problems*. Addison-Wesley Series in Computer Science and Information Processing. Addison-Wesley Publishing Company, 1969.
- [175] F. Reimold. *Experimental Studies and Modeling of Divertor Plasma Detachment in H-Mode Discharges in the ASDEX Upgrade Tokamak*. IPP-Report 11/27. Diploma Thesis, TU München. Max-Planck-Institut für Plasmaphysik, Garching, Germany, 2011. URL: <http://hdl.handle.net/11858/00-001M-0000-0026-EB6F-7>.
- [176] D. Reiter. *The data file AMJUEL: Additional Atomic and Molecular Data for EIRENE*. Institut für Energie- und Klimaforschung – Plasmaphysik, Forschungszentrum Jülich GmbH. 2020. URL: <http://www.eirene.de/amjuel.pdf>.
- [177] D. Reiter. *The data file HYDHEL: Atomic and Molecular Data for EIRENE*. Institut für Energie- und Klimaforschung – Plasmaphysik, Forschungszentrum Jülich GmbH. 2020. URL: <http://www.eirene.de/hydhel.pdf>.
- [178] D. Reiter. *The TRIM code surface database*. Institut für Energie- und Klimaforschung – Plasmaphysik, Forschungszentrum Jülich GmbH. 2010. URL: <http://www.eirene.de/manuals/trim.pdf>.
- [179] *ADAS - Atomic Data and Analysis Structure*. URL: <http://www.adas.ac.uk/>.
- [180] D. Reiter, M. Baelmans, and P. Börner. “The EIRENE and B2-EIRENE Codes”. In: *Fusion Science and Technology* 47.2 (2005), pp. 172–186. DOI: 10.13182/fst47-172.
- [181] V. Kotov et al. “Numerical modelling of high density JET divertor plasma with the SOLPS4.2 (B2-EIRENE) code”. In: *Plasma Physics and Controlled Fusion* 50.10 (2008), p. 105012. DOI: 10.1088/0741-3335/50/10/105012.
- [182] K. Ghooos et al. “Accuracy and convergence of coupled finite-volume/Monte Carlo codes for plasma edge simulations of nuclear fusion reactors”. In: *Journal of Computational Physics* 322 (2016), pp. 162–182. DOI: 10.1016/j.jcp.2016.06.049.

-
- [183] K. Ghoo et al. “Accuracy and Convergence of Coupled Finite-Volume / Monte-Carlo Codes for Plasma Edge Simulations”. In: *Contributions to Plasma Physics* 56.6-8 (2016), pp. 616–621. DOI: 10.1002/ctpp.201610010.
- [184] M. Baelmans et al. “Efficient code simulation strategies for B2-EIRENE”. In: *Nuclear Materials and Energy* 12 (2017), pp. 858–863. DOI: 10.1016/j.nme.2016.10.028.
- [185] D. P. Coster et al. *SOLPS-ITER Manual*. Version from 23 April 2020; only accessible with ITER user account; ITER Organisation.
- [186] *DivGeo_Carre_Triang Manual*. Only accessible with ITER user account; ITER Organisation.
- [187] S. Wiesen et al. “On the role of finite grid extent in SOLPS-ITER edge plasma simulations for JET H-mode discharges with metallic wall”. In: *Nuclear Materials and Energy* 17 (2018), pp. 174–181. DOI: 10.1016/j.nme.2018.10.013.
- [188] S. Varoutis et al. *Simulation of Neutral Gas Flow in the JET Sub-Divertor and Comparison with Experimental Results*. EFDA-JET-CP(14)06/37. EUROfusion, 2014. URL: <http://www.euro-fusionscipub.org/archives/jet-archive/simulation-of-neutral-gas-flow-in-the-jet-sub-divertor-and-comparison-with-experimental-results>.
- [189] D. Moulton et al. “Pumping in vertical and horizontal target configurations on JET in L-mode; an interpretive study using EDGE2D-EIRENE”. In: *Proceedings of the 42nd EPS Conference on Controlled Fusion and Plasma Physics, Lisbon, 2015*. O4.119. 2015. URL: <http://ocs.ciemat.es/EPS2015PAP/pdf/O4.119.pdf>.
- [190] T. Eich et al. “Correlation of the tokamak H-mode density limit with ballooning stability at the separatrix”. In: *Nuclear Fusion* 58.3 (2018), p. 034001. DOI: 10.1088/1741-4326/aaa340.
- [191] H. J. Sun et al. “Study of near SOL decay lengths in ASDEX Upgrade under attached and detached divertor conditions”. In: *Plasma Physics and Controlled Fusion* 59.10 (2017), p. 105010. DOI: 10.1088/1361-6587/aa7777.
- [192] P.-H. Rebut. “The Joint European Torus (JET)”. In: *The European Physical Journal H* 43.4-5 (2018), pp. 459–497. DOI: 10.1140/epjh/e2017-70068-y.
- [193] M. Keilhacker et al. “The scientific success of JET”. In: *Nuclear Fusion* 41.12 (2001), pp. 1925–1966. DOI: 10.1088/0029-5515/41/12/217.
- [194] G. F. Matthews et al. “JET ITER-like wall—overview and experimental programme”. In: *Physica Scripta* T145 (2011), p. 014001. DOI: 10.1088/0031-8949/2011/t145/014001.
- [195] F. Romanelli and JET EFDA Contributors. “Overview of the JET results with the ITER-like wall”. In: *Nuclear Fusion* 53.10 (2013), p. 104002. DOI: 10.1088/0029-5515/53/10/104002.
- [196] A. Loarte. “Effects of divertor geometry on tokamak plasmas”. In: *Plasma Physics and Controlled Fusion* 43.6 (2001), R183–R224. DOI: 10.1088/0741-3335/43/6/201.
- [197] R. S. Cohen, L. Spitzer, and P. M. Routly. “The Electrical Conductivity of an Ionized Gas”. In: *Physical Review* 80.2 (1950), pp. 230–238. DOI: 10.1103/physrev.80.230.
- [198] E. Lerche et al. “Optimization of ICRH for core impurity control in JET-ILW”. In: *Nuclear Fusion* 56.3 (2016), p. 036022. DOI: 10.1088/0029-5515/56/3/036022.

-
- [199] D. Čirić et al. “Overview of the JET neutral beam enhancement project”. In: *Fusion Engineering and Design* 82.5-14 (2007), pp. 610–618. DOI: 10.1016/j.fusengdes.2007.07.046.
- [200] R. J. Goldston et al. “New techniques for calculating heat and particle source rates due to neutral beam injection in axisymmetric tokamaks”. In: *Journal of Computational Physics* 43.1 (1981), pp. 61–78. DOI: 10.1016/0021-9991(81)90111-x.
- [201] P. M. Stubberfield and M. L. Watkins. *Multiple Pencil Beam*. Tech. rep. JET-DPA(06)/87. EUROfusion, 1987.
- [202] G. Corrigan, D. G. Muir, and F. Tibone. *Neutral Beam-Plasma Interaction in JET: Comparison of PENCIL and TRANSP Modelling Results*. JET-R(99)13. EUROfusion, 1999. URL: <http://www.euro-fusionscipub.org/archives/jet-archive/neutral-beam-plasma-interaction-in-jet-comparison-of-pencil-and-transp-modelling-results>.
- [203] R. J. H. Pearce et al. “The JET tokamak gas handling and introduction system”. In: *18th IEEE/NPSS Symposium on Fusion Engineering. Symposium Proceedings (Cat. No. 99CH37050)*. IEEE, 1999. DOI: 10.1109/fusion.1999.849902.
- [204] I. Carvalho. *Private communication via e-mail (06.08.2019)*.
- [205] M. N. A. Beurskens et al. “Pedestal and ELM response to impurity seeding in JET advanced scenario plasmas”. In: *Nuclear Fusion* 48.9 (2008), p. 095004. DOI: 10.1088/0029-5515/48/9/095004.
- [206] R. J. H. Pearce et al. “Vacuum pumping developments on the JET tokamak”. In: *Fusion Engineering and Design* 58-59 (2001), pp. 359–364. DOI: 10.1016/s0920-3796(01)00325-8.
- [207] W. Obert et al. “Performance of the JET pumped divertor cryopump system”. In: *Proceedings of 16th International Symposium on Fusion Engineering*. IEEE, 1995. DOI: 10.1109/fusion.1995.534329.
- [208] R. Lässer et al. “Overview of the performance of the JET Active Gas Handling System during and after DTE1”. In: *Fusion Engineering and Design* 47.2-3 (1999), pp. 173–203. DOI: 10.1016/s0920-3796(99)00082-4.
- [209] A. Huber et al. “Upgraded bolometer system on JET for improved radiation measurements”. In: *Fusion Engineering and Design* 82.5-14 (2007), pp. 1327–1334. DOI: 10.1016/j.fusengdes.2007.03.027.
- [210] K. F. Mast et al. “A low noise highly integrated bolometer array for absolute measurement of VUV and soft x radiation”. In: *Review of Scientific Instruments* 62.3 (1991), pp. 744–750. DOI: 10.1063/1.1142078.
- [211] M. Bernert. “Analysis of the H-mode density limit in the ASDEX Upgrade tokamak using bolometry”. PhD thesis. Ludwig-Maximilians-Universität München, 2013. URL: <https://nbn-resolving.org/urn:nbn:de:bvb:19-162625>.
- [212] K. McCormick et al. “New bolometry cameras for the JET Enhanced Performance Phase”. In: *Fusion Engineering and Design* 74.1-4 (2005), pp. 679–683. DOI: 10.1016/j.fusengdes.2005.06.153.

-
- [213] A. Huber et al. “Improved radiation measurements on JET – First results from an upgraded bolometer system”. In: *Journal of Nuclear Materials* 363-365 (2007), pp. 365–370. DOI: 10.1016/j.jnucmat.2007.01.124.
- [214] L. C. Ingesson et al. “Chapter 7: Tomography Diagnostics: Bolometry and Soft-X-Ray Detection”. In: *Fusion Science and Technology* 53.2 (2008), pp. 528–576. DOI: 10.13182/fst53-528.
- [215] J. C. Fuchs et al. “Twodimensional reconstruction of the radiation power density in ASDEX Upgrade”. In: *Proceedings of the 21st EPS Conference on Controlled Fusion and Plasma Physics, Montpellier, 1994*. Vol. Vol 18B. Part III. 1994, pp. 1308–1311.
- [216] L. C. Ingesson et al. “Radiation distribution and neutral-particle loss in the JET MkI and MkIIA divertors”. In: *Proceedings of the 24th EPS Conference on Controlled Fusion and Plasma Physics, Berchtesgaden, 1997*. Vol. Vol 21A. Part I. 1997, pp. 113–116. URL: <http://epsppd.epfl.ch/Madeira/pdfs/P4.083.pdf>.
- [217] L. C. Ingesson et al. “Soft X ray tomography during ELMs and impurity injection in JET”. In: *Nuclear Fusion* 38.11 (1998), pp. 1675–1694. DOI: 10.1088/0029-5515/38/11/307.
- [218] D. R. Ferreira et al. “Full-Pulse Tomographic Reconstruction with Deep Neural Networks”. In: *Fusion Science and Technology* 74.1-2 (2018), pp. 47–56. DOI: 10.1080/15361055.2017.1390386.
- [219] L. C. Ingesson. *Comparison of Methods to Determine the Total Radiated Power in JET*. JET-R(99)06. EUROfusion, 1999. URL: <http://www.euro-fusionscipub.org/archives/jet-archive/comparison-of-methods-to-determine-the-total-radiated-power-in-jet>.
- [220] *KS3 (Openwiki)*. JET Openwiki entry; last modified on 8 August 2019, at 09:37; only accessible with EUROfusion user account; EUROfusion. URL: <https://users.euro-fusion.org/openwiki/index.php/KS3>.
- [221] *KS3 (JET Data Handbook)*. JET Data Handbook Diagnostics entry; last modified on 03 July 2019, at 13:54; only accessible with EUROfusion user account; EUROfusion. URL: <https://users.euro-fusion.org/pages/data-dmsd/jetdatahandbook/php/entry.php?type=0&name=KS3>.
- [222] K. Kadota, M. Otsuka, and J. Fujita. “Space- and time-resolved study of impurities by visible spectroscopy in the high-density regime of JIPP T-II tokamak plasma”. In: *Nuclear Fusion* 20.2 (1980), pp. 209–212. DOI: 10.1088/0029-5515/20/2/010.
- [223] T. M. Biewer et al. *Expanded Capability of the Edge Charge-Exchange Recombination Spectroscopy System on JET*. EFDA-JET-CP(08)03/07. EUROfusion, 2008. URL: <http://www.euro-fusionscipub.org/archives/jet-archive/expanded-capability-of-the-edge-charge-exchange-recombination-spectroscopy-system-on-jet>.
- [224] S. Menmuir. “KS5 for S. Gloegler”. only accessible with EUROfusion user account. 2017. URL: https://users.euro-fusion.org/openwiki/images/0/0a/92118_profiles_ex_smenmuir_10nov17.pdf.
- [225] R. Pasqualotto et al. “High resolution Thomson scattering for Joint European Torus (JET)”. In: *Review of Scientific Instruments* 75.10 (2004), pp. 3891–3893. DOI: 10.1063/1.1787922.

- [226] L. Frassinetti et al. “Spatial resolution of the JET Thomson scattering system”. In: *Review of Scientific Instruments* 83.1 (2012), p. 013506. DOI: 10.1063/1.3673467.
- [227] S. S. Denk. “Study of non-thermal electron energy distribution functions by modeling of electron cyclotron emission from the fusion plasmas of the ASDEX Upgrade tokamak”. Dissertation. München: Technische Universität München, 2019. URL: <http://nbn-resolving.org/urn/resolver.pl?urn:nbn:de:bvb:91-diss-20190130-1467462-1-9>.
- [228] E. de la Luna et al. “Electron cyclotron emission radiometer upgrade on the Joint European Torus (JET) tokamak”. In: *Review of Scientific Instruments* 75.10 (2004), pp. 3831–3833. DOI: 10.1063/1.1781376.
- [229] G. Braithwaite et al. “JET polari-interferometer”. In: *Review of Scientific Instruments* 60.9 (1989), pp. 2825–2834. DOI: 10.1063/1.1140666.
- [230] A. Boboc et al. “Upgrade of the JET far infrared interferometer diagnostic”. In: *Review of Scientific Instruments* 83.10 (2012), 10E341. DOI: 10.1063/1.4737420.
- [231] *KY4D (JET Data Handbook)*. JET Data Handbook (Diagnostics) entry; last modified on 03 December 2019, at 14:50; only accessible with EUROfusion user account; EUROfusion. URL: <https://users.euro-fusion.org/pages/data-dmsd/jetdatahandbook/php/entry.php?type=0&name=KY4D>.
- [232] R. D. Monk et al. “Divertor Langmuir Probe Measurements in JET”. In: *Contributions to Plasma Physics* 36.S1 (1996), pp. 37–44. DOI: 10.1002/ctpp.19960360107.
- [233] D. Tskhakaya et al. “Interpretation of divertor Langmuir probe measurements during the ELMs at JET”. In: *Journal of Nuclear Materials* 415.1 (2011), S860–S864. DOI: 10.1016/j.jnucmat.2010.10.090.
- [234] G. F. Matthews et al. “Divertor energy distribution in JET H-modes”. In: *Journal of Nuclear Materials* 290-293 (2001), pp. 668–672. DOI: 10.1016/s0022-3115(00)00482-7.
- [235] A. Huber et al. “The effect of field reversal on the JET MkiIGB-SRP divertor performance in L-mode density limit discharges”. In: *Journal of Nuclear Materials* 337-339 (2005), pp. 241–245. DOI: 10.1016/j.jnucmat.2004.10.123.
- [236] R. A. Pitts et al. “Edge and divertor physics with reversed toroidal field in JET”. In: *Journal of Nuclear Materials* 337-339 (2005), pp. 146–153. DOI: 10.1016/j.jnucmat.2004.10.111.
- [237] L. Aho-Mantila et al. “Assessment of SOLPS5.0 divertor solutions with drifts and currents against L-mode experiments in ASDEX Upgrade and JET”. In: *Plasma Physics and Controlled Fusion* 59.3 (2017), p. 035003. DOI: 10.1088/1361-6587/59/3/035003.
- [238] G. F. Matthews, JET EFDA Contributors, and the ASDEX-Upgrade Team. “Plasma operation with an all metal first-wall: Comparison of an ITER-like wall with a carbon wall in JET”. In: *Journal of Nuclear Materials* 438 (2013), S2–S10. DOI: 10.1016/j.jnucmat.2013.01.282.
- [239] S. Brezinsek and JET-EFDA contributors. “Plasma-surface interaction in the Be/W environment: Conclusions drawn from the JET-ILW for ITER”. In: *Journal of Nuclear Materials* 463 (2015), pp. 11–21. DOI: 10.1016/j.jnucmat.2014.12.007.
- [240] I. Nunes and JET contributors. “Plasma confinement at JET”. In: *Plasma Physics and Controlled Fusion* 58.1 (2016), p. 014034. DOI: 10.1088/0741-3335/58/1/014034.

-
- [241] N. Fedorczak et al. “Tungsten transport and sources control in JET ITER-like wall H-mode plasmas”. In: *Journal of Nuclear Materials* 463 (2015), pp. 85–90. DOI: 10.1016/j.jnucmat.2014.12.044.
- [242] N. Den Harder et al. “ELM-resolved divertor erosion in the JET ITER-Like Wall”. In: *Nuclear Fusion* 56.2 (2016), p. 026014. DOI: 10.1088/0029-5515/56/2/026014.
- [243] L. Frassinetti et al. “Effect of nitrogen seeding on the energy losses and on the time scales of the electron temperature and density collapse of type-I ELMs in JET with the ITER-like wall”. In: *Nuclear Fusion* 55.2 (2015), p. 023007. DOI: 10.1088/0029-5515/55/2/023007.
- [244] A. Järvinen et al. “Simulations of tungsten transport in the edge of JET ELMy H-mode plasmas”. In: *Journal of Nuclear Materials* 438 (2013), S1005–S1009. DOI: 10.1016/j.jnucmat.2013.01.219.
- [245] M. Goniche et al. “Ion cyclotron resonance heating for tungsten control in various JET H-mode scenarios”. In: *Plasma Physics and Controlled Fusion* 59.5 (2017), p. 055001. DOI: 10.1088/1361-6587/aa60d2.
- [246] C. F. Maggi et al. “L–H power threshold studies in JET with Be/W and C wall”. In: *Nuclear Fusion* 54.2 (2014), p. 023007. DOI: 10.1088/0029-5515/54/2/023007.
- [247] M. N. A. Beurskens et al. “The effect of a metal wall on confinement in JET and ASDEX Upgrade”. In: *Plasma Physics and Controlled Fusion* 55.12 (2013), p. 124043. DOI: 10.1088/0741-3335/55/12/124043.
- [248] M. N. A. Beurskens et al. “Global and pedestal confinement in JET with a Be/W metallic wall”. In: *Nuclear Fusion* 54.4 (2014), p. 043001. DOI: 10.1088/0029-5515/54/4/043001.
- [249] C. F. Maggi et al. “Pedestal confinement and stability in JET-ILW ELMy H-modes”. In: *Nuclear Fusion* 55.11 (2015), p. 113031. DOI: 10.1088/0029-5515/55/11/113031.
- [250] C. Giroud et al. “Progress at JET in integrating ITER-relevant core and edge plasmas within the constraints of an ITER-like wall”. In: *Plasma Physics and Controlled Fusion* 57.3 (2015), p. 035004. DOI: 10.1088/0741-3335/57/3/035004.
- [251] A. E. Jaervinen et al. “Comparison of H-mode plasmas in JET-ILW and JET-C with and without nitrogen seeding”. In: *Nuclear Fusion* 56.4 (2016), p. 046012. DOI: 10.1088/0029-5515/56/4/046012.
- [252] D. Moulton et al. “Neutral pathways and heat flux widths in vertical- and horizontal-target EDGE2D-EIRENE simulations of JET”. In: *Nuclear Fusion* 58.9 (2018), p. 096029. DOI: 10.1088/1741-4326/aacf0f.
- [253] E. Joffrin et al. “Impact of divertor geometry on H-mode confinement in the JET metallic wall”. In: *Nuclear Fusion* 57.8 (2017), p. 086025. DOI: 10.1088/1741-4326/aa6e1c.
- [254] M. J. Leyland et al. “The H-mode pedestal structure and its role on confinement in JET with a carbon and metal wall”. In: *Nuclear Fusion* 55.1 (2015), p. 013019. DOI: 10.1088/0029-5515/55/1/013019.
- [255] H. Meyer et al. “The role of divertor and SOL physics for access to H-mode on JET”. In: *Proceedings of the 41st EPS Conference on Controlled Fusion and Plasma Physics, Berlin, 2014*. P1.013. 2014. URL: <http://ocs.ciemat.es/EPS2014PAP/pdf/P1.013.pdf>.

- [256] E. Delabie et al. “The relation between divertor conditions and the L–H threshold on JET”. In: *Proceedings of the 42nd EPS Conference on Controlled Fusion and Plasma Physics, Lisbon, 2015*. O3.113. 2015. URL: <http://ocs.ciemat.es/EPS2015PAP/pdf/O3.113.pdf>.
- [257] E. Delabie et al. *Overview and Interpretation of L–H Threshold Experiments on JET with the ITER-like Wall*. EFDA–JET–CP(14)06/18. EUROfusion, 2014. URL: <http://www.euro-fusionscipub.org/archives/jet-archive/overview-and-interpretation-of-l-h-threshold-experiments-on-jet-with-the-iter-like-wall>.
- [258] C. Giroud et al. “Integration of a radiative divertor for heat load control into JET high triangularity ELMy H-mode plasmas”. In: *Nuclear Fusion* 52.6 (2012), p. 063022. DOI: 10.1088/0029-5515/52/6/063022.
- [259] S. Glöggler et al. “Corrigendum: characterisation of highly radiating neon seeded plasmas in JET-ILW (2019 Nucl. Fusion 59 126031)”. In: *Nuclear Fusion* 60.7 (2020), p. 079501. DOI: 10.1088/1741-4326/ab9025.
- [260] E. Joffrin et al. “First scenario development with the JET new ITER-like wall”. In: *Nuclear Fusion* 54.1 (2014), p. 013011. DOI: 10.1088/0029-5515/54/1/013011.
- [261] F. Wagner et al. “Development of an Edge Transport Barrier at the H-Mode Transition of ASDEX”. In: *Physical Review Letters* 53.15 (1984), pp. 1453–1456. DOI: 10.1103/physrevlett.53.1453.
- [262] H. Zohm. “Dynamic behavior of the L-H transition”. In: *Physical Review Letters* 72.2 (1994), pp. 222–225. DOI: 10.1103/physrevlett.72.222.
- [263] F. Ryter et al. “Experimental evidence for the key role of the ion heat channel in the physics of the L–H transition”. In: *Nuclear Fusion* 54.8 (2014), p. 083003. DOI: 10.1088/0029-5515/54/8/083003.
- [264] A. Kallenbach et al. “Impurity seeding for tokamak power exhaust: from present devices via ITER to DEMO”. In: *Plasma Physics and Controlled Fusion* 55.12 (2013), p. 124041. DOI: 10.1088/0741-3335/55/12/124041.
- [265] G. Pereverzev and P. N. Yushmanov. *ASTRA Automated System for TRansport Analysis in a Tokamak*. IPP-Report 5/98. Max-Planck-Institut für Plasmaphysik, Garching, Germany, 2002. URL: <http://hdl.handle.net/11858/00-001M-0000-0027-4510-D>.
- [266] G. M. Staebler, J. E. Kinsey, and R. E. Waltz. “A theory-based transport model with comprehensive physics”. In: *Physics of Plasmas* 14.5 (2007), p. 055909. DOI: 10.1063/1.2436852.
- [267] E. Fable et al. “Novel free-boundary equilibrium and transport solver with theory-based models and its validation against ASDEX Upgrade current ramp scenarios”. In: *Plasma Physics and Controlled Fusion* 55.12 (2013), p. 124028. DOI: 10.1088/0741-3335/55/12/124028.
- [268] G. M. Staebler et al. “A model of the saturation of coupled electron and ion scale gyrokinetic turbulence”. In: *Nuclear Fusion* 57.6 (2017), p. 066046. DOI: 10.1088/1741-4326/aa6bee.
- [269] N. Bonanomi et al. “Effects of nitrogen seeding on core ion thermal transport in JET ILW L-mode plasmas”. In: *Nuclear Fusion* 58.2 (2018), p. 026028. DOI: 10.1088/1741-4326/aa9e7c.

-
- [270] R. R. Dominguez and M. N. Rosenbluth. “Local kinetic stability analysis of the ion temperature gradient mode”. In: *Nuclear Fusion* 29.5 (1989), pp. 844–848. DOI: 10.1088/0029-5515/29/5/015.
- [271] C. D. Challis et al. “Impact of neon seeding on fusion performance in JET ILW hybrid plasmas”. In: *Proceedings of the 44th EPS Conference on Controlled Fusion and Plasma Physics, Belfast, 2017*. P2.153. 2017. URL: <http://ocs.ciemat.es/EPS2017PAP/pdf/P2.153.pdf>.
- [272] D. Frigione et al. “Impact of Neon Injection on Electron Density Peaking in JET Hybrid Plasmas”. In: *27th IAEA Fusion Energy Conference, Ahmedabad, India*. P/233, submitted to *Nuclear Fusion*. 2018. URL: <https://nucleus.iaea.org/sites/fusionportal/Shared%20Documents/FEC%202018/fec2018-preprints/preprint0233.pdf>.
- [273] M. Romanelli et al. “Electron Density Peaking Induced by Neon seeding in JET Hybrid Plasmas”. In: *23rd Joint EU-US Transport Task Force Meeting, Seville, Spain*. 2018. URL: http://www.psft.eu/ttf2018/wp-content/uploads/2018/06/romanelli_abstract_ttf2018.pdf.
- [274] M. Sertoli. *Private communication via e-mail (21.05.2019)*.
- [275] M. Sertoli et al. “Determination of 2D poloidal maps of the intrinsic W density for transport studies in JET-ILW”. In: *Review of Scientific Instruments* 89.11 (2018), p. 113501. DOI: 10.1063/1.5046562.
- [276] M. Sertoli et al. “Measuring the plasma composition in tokamaks with metallic plasma-facing components”. In: *Journal of Plasma Physics* 85.5 (2019). DOI: 10.1017/s0022377819000618.
- [277] I. Paradela Pérez et al. “SOL parallel momentum loss in ASDEX Upgrade and comparison with SOLPS”. In: *Nuclear Materials and Energy* 12 (2017), pp. 181–186. DOI: 10.1016/j.nme.2017.01.026.
- [278] R. Dux et al. “Influence of CX-reactions on the radiation in the pedestal region at ASDEX Upgrade”. In: *Nuclear Fusion* 60.12 (2020), p. 126039. DOI: 10.1088/1741-4326/abb748.
- [279] B. Viola et al. “Study of the effect of the outer-strike point location on the divertor neutral pressure in JET-ILW using EDGE2D/EIRENE”. In: *Proceedings of the 40th EPS Conference on Controlled Fusion and Plasma Physics, Helsinki, 2013*. P1.114. 2013. URL: <http://ocs.ciemat.es/EPS2013PAP/pdf/P1.114.pdf>.
- [280] A. E. Jaervinen et al. “Interpretation of partially detached divertor operation with and without impurity seeding in JET with EDGE2D-EIRENE”. In: *Proceedings of the 42nd EPS Conference on Controlled Fusion and Plasma Physics, Lisbon, 2015*. P2.105. 2015. URL: <http://ocs.ciemat.es/EPS2015PAP/pdf/P2.105.pdf>.
- [281] M. Groth et al. “Divertor plasma conditions and neutral dynamics in horizontal and vertical divertor configurations in JET-ILW low confinement mode plasmas”. In: *Journal of Nuclear Materials* 463 (2015), pp. 471–476. DOI: 10.1016/j.jnucmat.2014.12.030.
- [282] K. D. Lawson et al. “A study of the atomic and molecular power loss terms in EDGE2D-EIRENE simulations of JET ITER-like wall L-mode discharges”. In: *Nuclear Materials and Energy* 12 (2017), pp. 924–930. DOI: 10.1016/j.nme.2017.04.015.

- [283] F. Reimold. “Experimental Studies and Modeling of Divertor Plasma Detachment in H-Mode Discharges in the ASDEX Upgrade Tokamak”. Dissertation. Technische Universität München, 2015. URL: <http://nbn-resolving.de/urn/resolver.pl?urn:nbn:de:bvb:91-diss-20150108-1232875-0-7>.
- [284] O. Pan et al. “SOLPS-ITER modeling with activated drifts for a snowflake divertor in ASDEX Upgrade”. In: *Plasma Physics and Controlled Fusion* 62.4 (2020), p. 045005. DOI: 10.1088/1361-6587/ab7108.

A JET Pulse Numbers with Neon Seeding

For this thesis the neon-seeded JET discharges from the experimental programmes M13-17 and M15-20 listed below were evaluated. The rough baseline values are given, i.e. without considering e.g. the effect of ELMs, NBI heating drops, or the slowly decreasing puffs. Due to the compactness of this representation rounding errors are possible. Only relevant time windows are listed, e.g. without ramp-up or ramp-down phases. Discharges performed within the same JET sessions are grouped together. In the list the following quantities are shown:

JPN	JET Pulse Number
t (s)	Start and end of time window
P_{heat} (MW)	Total heating power
P_{NBI} (MW)	NBI heating power
P_{ICRH} (MW)	ICRH heating power
Γ_{D} (10^{22} e/s)	Deuterium puff
Γ_{Ne} (10^{21} e/s)	Neon puff
DB	Included in database?

JPN	t (s)	P_{heat} (MW)	P_{NBI}	P_{ICRH}	Γ_{D} (10^{22} e/s)	Γ_{Ne} (10^{21} e/s)	DB
84884	9.5 - 14.0	19	18	0	4.5	0.0	x
	14.0 - 17.0	19	18	0	4.5	0.0	x
85440	9.5 - 10.5	19	18	0	4.0	0.0	
	10.5 - 14.5	19	18	0	4.0	9.0	x
	14.5 - 17.0	19	18	0	4.0	0.0	x
85441	9.5 - 10.5	19	18	0	4.0	0.0	
	10.5 - 16.0	19	18	0	4.0	12.0	x
	16.0 - 17.0	19	18	0	4.0	0.0	
85442	9.5 - 10.5	19	18	0	4.0	0.0	
	10.5 - 12.0	19	18	0	4.0	16.0	
85443	9.5 - 10.5	19	18	0	4.0	0.0	
	10.5 - 14.0	19	18	0	4.0	13.0	x
87190	9.5 - 10.5	22	18	3	4.0	0.0	
	10.5 - 12.5	22	18	3	4.0	5.0	x
	12.5 - 15.0	22	18	3	2.0	5.0	x

JPN	t (s)	P_{heat} (MW)	P_{NBI}	P_{ICRH}	Γ_{D} (10^{22}e/s)	Γ_{Ne} (10^{21}e/s)	DB
87191	9.5 - 10.5	27	22	4	2.0	0.0	
	10.5 - 12.5	27	22	4	2.0	5.0	x
	12.5 - 15.0	27	22	4	4.0	5.0	x
87192	9.5 - 13.5	27	22	4	2.0	13.0	x
	13.5 - 15.0	27	22	4	4.0	12.0	x
87194	9.5 - 13.5	28	22	5	2.0	13.0	x
	13.5 - 15.0	28	22	5	4.0	12.0	x
87195	9.5 - 12.5	15	14	0	2.0	3.0	x
	12.5 - 15.0	15	14	0	4.0	3.0	x
87196	9.5 - 11.5	15	14	0	2.0	3.5	x
	11.5 - 12.7	15	14	0	4.0	4.5	x
	12.7 - 13.9	15	14	0	4.0	5.5	x
	13.9 - 15.0	15	14	0	4.0	6.5	x
87197	9.5 - 11.5	16	15	0	2.0	3.5	x
	11.5 - 12.7	16	15	0	4.0	10.0	x
	12.7 - 13.4	16	15	0	4.0	12.0	
92118	9.5 - 10.5	23	19	3	5.0	0.0	
	10.5 - 14.0	23	19	3	5.0	12.0	x
	14.0 - 15.0	23	19	3	5.0	0.0	
	15.0 - 17.0	23	19	3	7.0	0.0	
92120	10.0 - 13.0	25	19	5	5.0	11.0	x
	13.0 - 14.0	25	19	5	5.0	16.0	x
	14.0 - 15.0	25	19	5	5.0	0.0	
	15.0 - 17.0	25	19	5	7.0	0.0	
92124	10.0 - 12.5	27	21	5	5.0	20.0	x
	12.5 - 13.0	27	21	5	5.0	31.0	
92357	10.0 - 14.0	29	24	4	5.0	21.0	x
	14.0 - 15.0	29	24	4	5.0	0.0	
	15.0 - 16.5	29	24	4	7.0	0.0	
92358	10.0 - 14.0	29	24	4	5.0	25.0–0.0	
	15.0 - 16.5	29	24	4	7.0	0.0	
92359	10.0 - 11.5	29	24	4	5.0	9.0	x
	11.5 - 13.5	29	24	4	5.0	16.0	x
	13.5 - 15.0	29	24	4	5.0	0.0	
	15.0 - 16.5	29	24	4	7.0	0.0	
92360	10.0 - 12.0	30	24	5	4.5	21.0	x
	12.0 - 14.0	30	24	5	3.0	20.0	x
	14.0 - 15.0	30	24	5	5.5	0.0	
	15.0 - 16.5	30	24	5	7.5	0.0	

B Acknowledgments

This thesis profited a lot from the help and knowledge of others towards whom I want to express my gratitude. I would like to thank my academic supervisor Prof. Ulrich Stroth for giving me the opportunity to work on this topic and for his valuable feedback. I want to thank especially my supervisor Dr. Marco Wischmeier for his guidance and wide expertise that greatly helped in advancing this thesis.

During the work at this thesis I got to know a lot of researchers and people in the plasma fusion community who were always happy to provide help in their respective field of expertise, be it at IPP, JET, or anywhere else in the world. I appreciated this open atmosphere and would like to express my gratitude to the entire community. Especially, I would like to thank all researchers who took the time to explain their research to me and provide analyses, to all diagnostic and experiment responsible officers, the SOLPS community, the IT departments, workshop employees, and secretaries. I also gained a lot from the exchange with many PhD and undergraduate students whom I had the pleasure to meet during my thesis and would like to thank them for all the nice conversations and the delicious cakes. I want to thank all my friends and my family, especially my parents, my sister, and my wife, for always supporting me, not only during this thesis.